EFFECTS OF ADSORPTION ON MOLECULAR TRANSPORT IN NANOTUBE

A Thesis

by

SANSARNG RIEWCHOTISAKUL

Submitted to the Office of Graduate and Professional Studies of
Texas A&M University
in partial fulfillment of the requirements for the degree of

MASTER OF SCIENCE

Chair of Committee,	I. Yucel Akkutlu
Committee Members,	John Killough
	Yalchin Efendiev
Head of Department,	A. Daniel Hill

May 2015

Major Subject: Petroleum Engineering

ABSTRACT

Adsorbed hydrocarbons, stored along the walls of kerogen pores and capillaries of organic-rich shale, are generally considered unrecoverable until desorption at low pressure is induced. Consequently, production from these organic pores is considered solely due to transport of the bulk phase (free) fluid in the center of the pores, if given any consideration at all. In this research, using non-equilibrium steady-state flow Molecular Dynamics simulations, a piston-frame attached to a carbon nanotube is modeled to understand the effects of adsorbed phase on nanometer-scale transport under reservoir conditions.

Profound new results were observed. Not only that the adsorbed phase is observed to be mobile and potentially producible, its existence significantly enhances the overall transport in the nanotube when compare with the conventional Darcy-regime transport. These effects are found to be prominent at large pressure and pressure gradient, and in smaller pores and capillaries.

The simulation results are utilized to develop a dimensionless mass transport enhancement equation, designed to capture the effects of the mobile adsorbed phase with respect to the conventional Darcy-flow. Finally the approach is extended to a bundle of capillaries of varying sizes and used to predict kerogen permeability of a Marcellus shale sample. The enhancement on Darcy flow is estimated to be more than 50%. The study sheds new light on transport mechanism of organic-rich shale and provides further insight into quantifying production from unconventional resources.

ACKNOWLEDGEMENTS

I would like to thank my committee chair, Dr. I. Yucel Akkutlu, and my committee members Dr. John Killough and Dr. Yalchin Efendiev, for their guidance and support throughout the course of this research. I would also like to thank Dr. Khoa Bui for his advices and support in creating the simulation models with the piston.

Thanks go to my friends and colleagues in the Petroleum Engineering Department and to the faculty and staff for making my time at Texas A&M University a wonderful experience. Thanks also go to my sponsor PTT Exploration and Production Inc. of Thailand for the financial support during my graduate education.

Finally, thanks to my family for their encouragement that motivates me to pursue my graduate education.

NOMENCLATURE

P	Pressure
T	Temperature
Nm, nm	Nanometer
Ps, ps	Picosecond
Psi	Pound per square-inch absolute
J_i	Flux of phase i
A, A_i	Cross sectional area for flows and fluxes
k	Permeability
k_a	Apparent permeability
C_μ	Adsorbed phase concentration
R_a	Rate of adsorption
R_d	Rate of desorption
M	Molecular mass
μ	Dynamic viscosity
R	Gas constant
θ	Fraction of occupied adsorption sites
v_{HP}	Hagen-Poiseuille velocity, classical Darcy-flow
Q_{HP}	Hagen-Poiseuille volumetric flow rate
Q_{total}	Adsorbed and bulk volume flow rate with respect to bulk density
v_{ads}	Adsorbed phase velocity

C_{sv}	Adsorbed phase velocity coefficient
M_{HP}	Mass flow rate for single-phase Hagen-Poiseuille flow
M_{total}	Mass flow rate for bulk and adsorbed phase
$R_{me\text{-}bulk}$	Enhancement factor in bulk phase flow
$R_{me\text{-}s}$	Enhancement factor by adsorbed phase
R_{me}	Dimensionless mass transport enhancement ratio

TABLE OF CONTENTS

LIST OF FIGURES

Page

LIST OF FIGURES

LIST OF FIGURES

1 INTRODUCTION

Among the unconventional petroleum resources exploited in the United States in early 21st century, shales are arguably the biggest contributors to oil and gas production. As of 2009 Barnett shale has ranked as the largest gas producer in the country, replacing conventional gas reservoirs by a large margin. Some productive formations in Bakken, Eagle Ford, and Permian Basin, have been producing at rates well over 1 million barrels per day (EIA, 2014). This phenomenon was dubbed the 'shale revolution' and has pushed the U.S. towards being a top oil and gas producer globally.

Aside from within natural fractures, which exist only in certain shale formations, hydrocarbons are generally stored in two types of pore space: the large inorganic inter-granular matrix which acts more like the tight sands and the small organic pores associated with the organic matter, also known as kerogen (Figure 1.a). Previous studies have demonstrated that large amounts of hydrocarbons can be found within these organic pores, existing as a dense adsorbed phase along the pore walls (Ambrose et al., 2011).

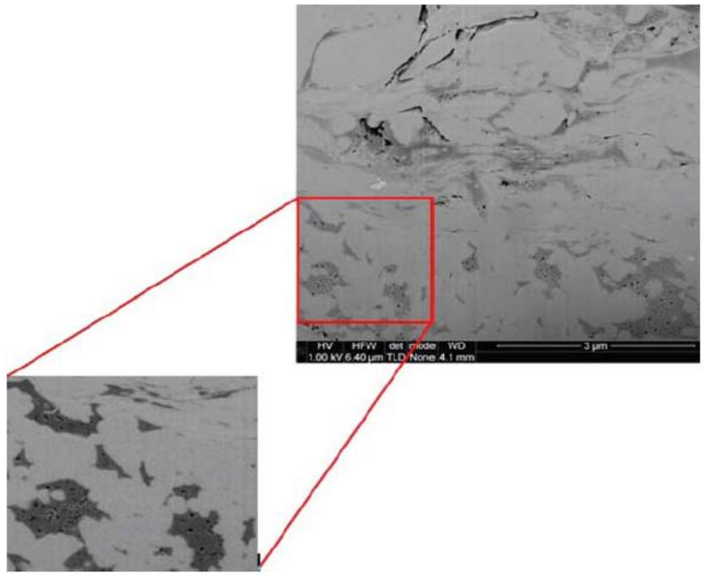

Figure 1.a: Image of Barnett shale sample in micron scale from a scanning electron microscope (Ambrose et al., 2012). The gray background is the inorganic matrix, whereas the imbedded dark patches are kerogen with nano-scale (< 50 nm) pores, where adsorbed gas resides. The large crack represents micro-fractures.

Adsorbed hydrocarbons are conventionally deemed stationary and unrecoverable unless a reduction in pore pressure induces their desorption into the bulk phase. Once they are desorbed, the molecules can be transported as part of the bulk phase. However, studies of molecular transport in other fields, particularly those in regards to surface diffusion (Figure 1.b), have previously showed that these molecules may have potency to move while adsorbed onto the surface (Choi, Do and Do, 2001; Fathi and Akkutlu, 2012). This hinted that, in addition to its role as a storage mechanism, adsorption along the organic pore wall may also contribute to the hydrocarbon transport. Analyzing the potential transport mechanism of the adsorbed hydrocarbons could provide a more accurate basis to predict gas production from shale resources and better identify its potential reserve. The latter has been the main drive in our research and has eventually led to development of this thesis.

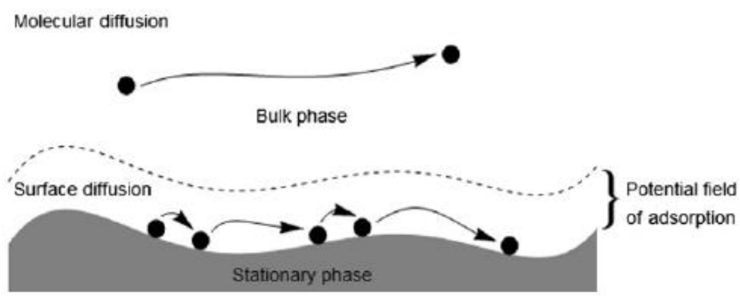

Figure 1.b: Surface diffusion mechanism (Medved and Cerny, 2011). The process could potentially applies to adsorbed gas in kerogen pores of shale reservoirs

2 LITERATURE REVIEW

2.1 Surface Diffusion

Surface diffusion, as its name states, is a phenomena involving transport of molecule along a surface. The process is generally represented by hopping-like mechanism occurring at relatively low pressure environment. In this model, adsorbed molecules are bounded to the surface sites with relatively weak van der Waals forces. When an adsorbed molecule gains sufficient energy, the binding force is overcome and it detaches itself from a surface site; when a molecule loses energy, it drops back down onto another site (see Figure 2.a). The constant cycles of gaining and losing energy allow molecule to travel from site to site, essentially moving along the surface (Duong, 1998). More complicated models could involve molecules readily adsorbing and desorbing on top of another molecule, in which binding force is lower. For hydrocarbons, however, only single-layered adsorptions are generally observed.

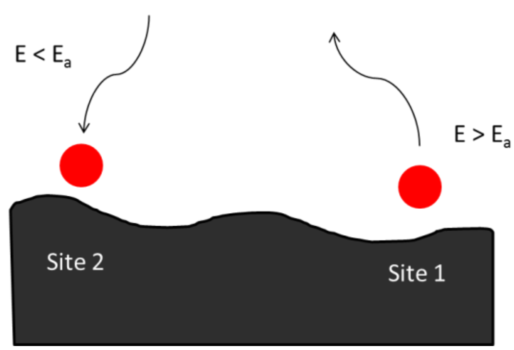

Figure 2.a: Hopping model scheme (Original Figure, Riewchotisakul, 2015). Molecules gain sufficient energy to overcome the heat of adsorption E_a will jump from surface site

Surface diffusion is usually quantified with Fickian diffusion equations. This means that flux in the transport direction is linearly dependent on the gradient of phase concentration. The surface concentration, i.e. adsorbed phase concentration, is often characterized as dependent on pressure and temperature; this means that for an isothermal system the diffusion gradient can be influenced or controlled by the pressure gradient. As such, if a multi-phase hydrocarbon storage system such as kerogen pore is under a pressure gradient, potential flow could occur for both bulk and adsorbed phases.

The Fickian diffusion approach to quantification of surface diffusion phenomena is mechanistic; the theory characterizes surface diffusion as an additional flux that is independent of the transport of the viscous bulk phase flow.

$$J_{total} = J_{bulk} + J_s \qquad (1)$$

Here J_{total} is the total transport flux, and J_{bulk} and J_s are transport terms for the bulk phase and the adsorbed phase, respectively. Total flux can be measured through laboratory experiments or simulations; the adsorbed phase flux is then quantified by subtracting the total flux with theoretical, calculated values of bulk phase flow (Medved and Cerny 2011).

The J_{bulk} above is often characterized with Darcy flow equations or in case of small pores, molecular diffusion. The adsorbed phase flux, J_s, is quantified using Fickian model's concentration gradient:

$$J_s = -D_s \nabla C_\mu \qquad (2)$$

J_s is the adsorbed phase mass flux (in moles or mass) per bulk area per time and C_μ is the concentration (or density) in adsorbed phase in moles per surface area or bulk volume. Here the diffusivity coefficient, D_s, represents a constant of proportionality quantifying the rate of transport independent of gradient, much like permeability. It may be formulated as a function of pressure, temperature, and molecule-wall interactions.

Several equations have been formulated in different forms for C_μ and D_s, depending on the wall-molecule pair and thermodynamic regime of adsorption. The most simplistic and most applicable model to hydrocarbon is that of Langmuir's: a monolayer adsorption scheme defined in terms of pressure and under isothermal condition.

2.2 Langmuir's Isothermal Equilibrium for Monolayer Adsorption

In 1918, Langmuir proposed his equilibrium model for single-layer adsorption on flat surfaces using rates obtained from kinetic theory of gases; the model is still applicable today, often used to evaluate the adsorbed methane in microporous coal bed reservoirs. Langmuir assumes a homogeneous surface where energy of adsorption, i.e. binding energy between molecules and walls, is constant and uniform throughout the medium. Monolayer adsorption is also assumed; only a single molecule can be adsorbed onto a surface site, and intermolecular forces are weak such that molecules cannot adsorb onto each other (Duong, 1998). These assumptions are certainly limited, but adequate for organic pores and capillaries and hydrocarbon system where monolayer adsorption is generally observed.

Using the kinetic theory of gases, the rate of molecules colliding on a wall is quantified as:

$$R_s = \frac{P}{\sqrt{2\pi MRT}} \tag{3}$$

R_s is the collision rate, in moles per area per time. P and T are the pressure and temperature. M is the molecular mass of the gas molecules and R is the universal gas constant.

Langmuir proposed that the greater number of collision onto a surface should result in greater number of molecule adsorbed and hence the adsorption rate should be proportional to R_s above. Since monolayer adsorption is assumed, the adsorption rate should also be proportional to the number of free sites available on the wall; this is quantified as fractional factor (1-θ), where θ is the portion of occupied sites. The probability of a molecule being adsorbed once it strikes an empty site is assumed to be constant for a medium and defined as a sticking coefficient 'α' (Duong, 1998). The rate of adsorption, R_a, is then proportional to the three factors above as follows:

$$R_a = \frac{\alpha P}{\sqrt{2\pi MRT}}(1-\theta) \tag{4}$$

Langmuir's treatment of desorption is similar to that of a chemical reaction, and in particular, the process of breaking chemical bonds. Adsorbed molecules that obtained enough activation energy to overcome the van der Waals attraction with the surface site can return to the free or bulk phase. Desorption rate in this case can be quantified using the Arrhenius equation. Naturally, desorption rate will depend on the amount of adsorbed molecules on the sites; this fraction is defined as θ, similar to the previous equation.

The equation for desorption rate, R_d, is:

$$R_d = (\theta)ke^{-\frac{E}{RT}} \tag{5}$$

R_d is desorption rate; k is a rate constant when temperature approach infinity. E is the energy binding the molecule to the surface, while R and T are gas constant and temperature, respectively.

At equilibrium, the adsorption rate should be equal to the desorption rate. Letting $R_a = R_d$, the equilibrium adsorbed fraction θ can be defined as:

$$\theta = \frac{bP}{1 + bP} \tag{6}$$

The coefficient b is dependent on aforementioned thermodynamic variables while E denotes the interaction between the gas molecule and the surface (Duong, 1998). Specifically:

$$b = b(T) = \frac{\alpha\, e^{\frac{E}{RT}}}{k\sqrt{2\pi MRT}} \tag{7}$$

2.3 Adsorbed Phase Concentration Gradient

Langmuir's definition of adsorption under thermodynamic equilibrium allows the concentration of the adsorbed phase to be defined in terms of pressure, and consecutively, the concentration gradient in terms of pressure gradient.

For a given surface such as kerogen pore wall, the adsorbed concentration should be proportional to the maximum concentration (when all sites are occupied) and the fraction adsorbed, in other words:

$$C_\mu = C_{\mu\, sat}\theta = C_{\mu\, sat}\frac{bP}{1+bP} \tag{8}$$

$C_{\mu\, sat}$ is adsorbed concentration at complete monolayer coverage, where $\theta = 1$. This equation is called the Langmuir Isotherm and is typically used in estimation of adsorbed hydrocarbon in uniform medium, such as coalbed methane.

According to the relationship above, the adsorbed phase concentration is dependent on pressure and temperature. Higher pressure and lower temperature means greater amount adsorbed and vice versa. This has been experimentally observed with multiple gases, shown in Figure 2.b.

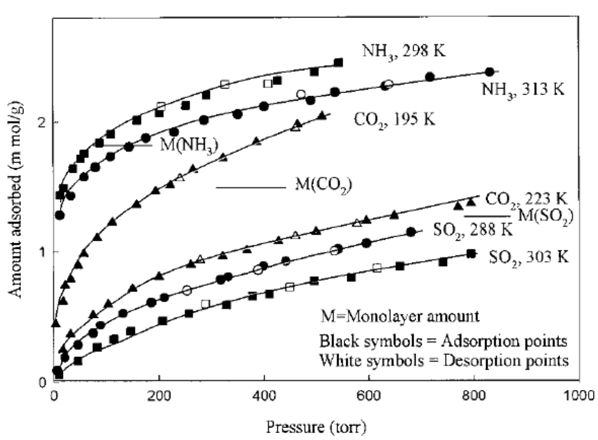

Figure 2.b: Plot of adsorbed amount (C_μ) against pressure for various gas species and temperature (Choi, Do, and Do 2001). The trend follows Langmuir model.

For one directional transport, in the L direction parallel to the pore wall, the concentration gradient simplifies to a single derivative:

$$\nabla C_{\mu} = \frac{dC_{\mu}}{dL} \tag{9}$$

From the existing relationship between C_{μ} and pressure, the concentration gradient can be converted to pressure gradient assuming isothermal condition:

$$\nabla C_{\mu} = \frac{dC_{\mu}}{dP}\nabla P = C_{\mu\, sat}\frac{b}{(1+bP)^2}\nabla P \tag{10}$$

For transport in one direction:

$$\nabla C_{\mu} = \frac{dC_{\mu}}{dL} = \frac{dC_{\mu}}{dP}\frac{dP}{dL} = C_{\mu\, sat}\frac{b}{(1+bP)^2}\frac{dP}{dL} \tag{11}$$

In contrast to the concentration (storage), the gradient (transport) above is expected to have an inverse relationship with pressure; less pressure, more mobility.

2.4 Quantifying Diffusion Coefficient – HIO and Yang's model

Many models exist to quantify D_s, the surface diffusivity coefficient. Some of them rely on the Einstein's two-dimensional (lateral surface) transport diffusivity equation:

$$D_s = \frac{\sigma^2}{4\tau} \tag{12}$$

In this case, σ is the distance between surface sites. τ is the holding time: a period where molecule remains stationary on the site (Duong, 1998).

The hopping model, on the other hand, defines adsorption and desorption as activated processes; as such, τ and consequently D_s can be quantified using Arrhenius equations:

$$\tau = \tau_0 \, e^{\frac{E}{RT}} \tag{13}$$

$$D_s(\theta) = D_{s\infty}(\theta) \, e^{-\frac{E}{RT}} \tag{14}$$

The constant $D_{s\infty}$ is maximum diffusivity at infinite temperature while E is the binding energy between the surface site and adsorbed molecule that is needed to overcome.

As shown above, D_s and subsequently $D_{s\infty}$ are also functions of θ. The availability of the free sites affects the mobility of surface transport such that with greater number of filled sites, molecules hop more to land on an empty site; thus, higher θ should theoretically result in greater diffusivity. In high pressure system such as hydrocarbon reservoir, however, it is generally safe to assume saturated condition where $\theta \approx 1$.

In 1966, Higashi, Oya, and Oishi proposed a model for the surface diffusivity coefficient. The so-called HIO model assumes the holding time is relatively small compares to the mobile period of the hopping molecule. The probability of a molecule achieving the k^{th} hopping step after leaving adsorption site is then $\theta^{k-1}(1-\theta)$. Averaging the probability over all the molecules, the number of steps approaches infinity yields the relationship:

$$\frac{D_s(\theta)}{D_s(0)} = \frac{1}{1-\theta} \tag{15}$$

$D_s(0)$ is constant diffusivity coefficient at zero saturation (Higashi, Oya, and Oishi 1966)

It can be easily deduced from the equation above that as θ approaches 1, i.e., at high pressure, the diffusivity coefficient will approach unrealistically high value. The model is further modified later on by Yang, Fenn, and Haller (1973) in order to account for D_s when adsorption approaches saturation. In such case, there is a need to consider the van der Waals attraction between two molecules experiencing hopping on each other. The effects of the pseudo-second layer will become more prominent as the first layer approach saturation.

$$\frac{D_s(\theta)}{D_s(0)} = \frac{1}{(1-\theta) + \theta \frac{v_1}{v_2} e^{-\frac{\Delta E_1 - \Delta E_2}{RT}}} \tag{16}$$

In the above equation, ΔE_1 is the energy binding molecules to a site (denoted simply as E in previous equations); ΔE_2 is energy between two molecules as one lands onto an occupied site. v_1 and v_2 are vibrational frequencies of the moving molecule in the first and second adsorbed layer, respectively. In this case the diffusivity will approach a finite number as the first adsorbed layer reaches saturation (see Figure 2.c)

Combining Yang et al's modified HIO model for diffusivity coefficient and the Arrhenius relationship yields a mono layer adsorption diffusivity coefficient:

$$D_s = D_{s\infty}\, e^{-\frac{E_s}{RT}} \frac{1}{(1-\theta) + \theta \frac{v_1}{v_2} e^{-\frac{\Delta E_1 - \Delta E_2}{RT}}} \tag{17}$$

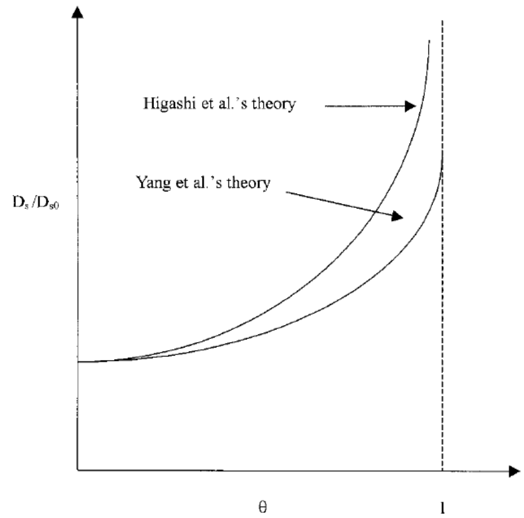

Figure 2.c: Comparison for D_s from HIO and Yang's modified HIO theory against saturation (Choi, Do, and Do 2001). D_s increases with saturation, but for original HIO model it deviates approaches infinity as θ approaches 1.

2.5 Mechanistic Model for Monolayer Surface Diffusion

The mechanistic model of monolayer adsorption flux, J_s, combines the modified HIO equation for diffusivity coefficient and Langmuir's relationship between concentration and pressure. Assuming isothermal condition, one-direction transport such as those through organic capillaries, the flux defined by pressure gradient is:

$$J_s = -\left[D_{S\infty}\, e^{-\frac{E_S}{RT}} \frac{1}{(1-\theta) + \theta \frac{v_1}{v_2} e^{-\frac{\Delta E_1 - \Delta E_2}{RT}}}\right]\left[C_{\mu\, sat} \frac{b}{(1+bP)^2} \frac{dP}{dL}\right] \tag{18}$$

The flux J_s is in units of mole per area per time and $\frac{dP}{dz}$ is the pressure gradient driving the transport.

Assuming a homogeneous molecular composition (e.g. pure Methane), under isothermal condition, and uniform molecule-wall interaction, all energy, vibrational frequencies, and temperature related terms will become constant. In such environment, the mechanistic flux above could be reduced to:

$$J_s = -\left[\frac{A'}{(1-\theta) + B'\theta}\right]\left[C_{\mu\, sat}\frac{b}{(1+bP)^2}\frac{dP}{dL}\right] \tag{19}$$

A' and B' are constants. Additionally, in high pressure environment often found in hydrocarbon reservoirs, the saturation of adsorption layer will most likely approach unity. Letting θ = 1 in the equation above further simplifies the flux to its pressure and gradient dependent form:

$$J_s = \left[\frac{C'}{(1+bP)^2}\right]\frac{dP}{dL} \tag{20}$$

C' is another constant. The above is the simplest variation of adsorbed phase flux equation. The assumptions required for this simplification (isothermal condition, uniform wall-molecule interaction, homogeneous fluid) are reasonable for the subsurface conditions. Further, they are appropriate restrictions for an investigation involving molecular simulations. This simplified relationship between flux, pressure, and gradient above will, therefore, be tested using non-equilibrium simulations.

2.6 Investigation of Density Behavior using Molecular Simulations

Recent researches have highlighted the significant contributions of organic pores and adsorbed phase to mass storage (Ambrose et al, 2011). Since the scale of these capillaries is extremely small, direct measurement of their properties are often not possible; many studies have employed computerized molecular simulation instead in order to investigate phenomena at nanometer scale. An example is shown below (Figure 2.d) where hydrocarbon phase behavior between nano-scale carbon slit pore is simulated (Rahmani and Akkutlu, 2013). Their predicted density profile across the pore width shows there are three distinct density regions at such scale (Figure 2.e).

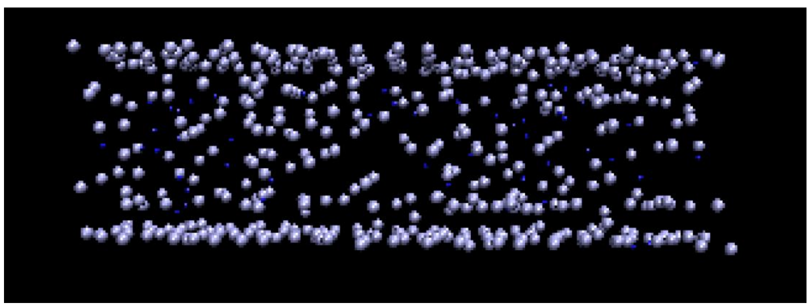

Figure 2.d: Visualization of molecular simulations of hydrocarbon in slit pore (Rahmani and Akkutlu, 2013). Simulation includes methane and ethane in nanometer-scale slit. Notice the dense adsorbed phase at upper and lower boundaries.

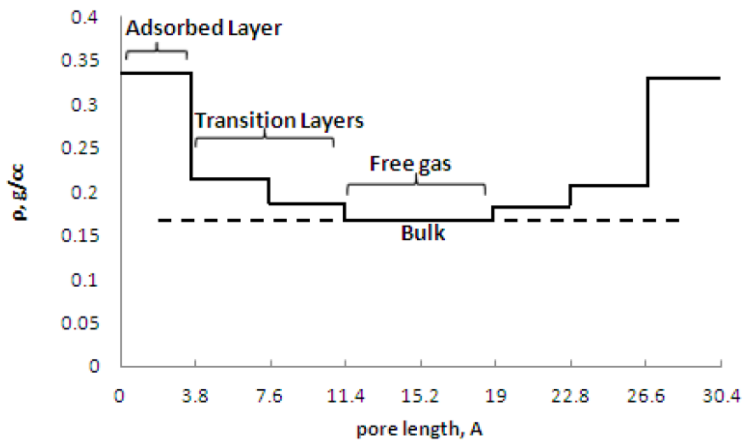

Figure 2.e: Density profile of adsorbed layer, bulk, and transition region (Rahmani and Akkutlu, 2013). The phases are identified through molecular simulations of Methane and Ethane in nanometer-scale slit pore

At the center is the bulk (free) region where molecules behave like conventional fluid, following densities predicted by the real gas laws. Adjacent to the wall is the dense adsorbed layer occupying the pore walls. Between them is the transition region where molecules readily adsorbed and desorbed. Structural density identified with transition layers in such studies has shown deviation from classical Langmuir model with monolayer adsorption.

3 RESEARCH METHODOLOGY

In order to analyze the effects of adsorbed phase on transport behavior on such a small scale, computer simulations of flow in a capillary will be employed. Specifically, Molecular Dynamics simulations of transport through a carbon tube with 5 nanometer diameter. The objectives was to create an isothermal, steady state flow across an organic capillary that is representative of those in kerogen and extract the phase densities and flow velocities across the diameter of the capillary during the steady flow period.

Simulation methodologies of transport problem in the field generally employ either DCV-GCMD (Dual Control Volume Grand Canonical Molecular Dynamics) or EF-MD (External Force field Molecular Dynamics).

In DCV-GCMD, simulations are generally set up with two tanks sandwiching a transport media, e.g. source and sink tanks connected by a tube. The general idea is to create a concentration or pressure gradient by adding more molecules to the source tank and deleting molecules from the sink location. This addition and deletion process is achieved with Monte Carlo Grand Canonical simulation. Since Monte Carlo cannot simulate ‘time’, the transport through the media has to be performed by Molecular Dynamics simulation; this result in repeating start-stop cycles between the two simulations: charging and flowing. The discontinuity in simulation due to repeated switch between Monte Carlo regime, which progress in random statistical steps while charging the molecules, and Molecular Dynamic, which progress in time while letting the molecule move, can induce error into the simulation in pulse-like manner. For example, large amount of molecule may be "suddenly" introduced to or deleted from the simulation in order to maintain pressure gradient: a phenomena which is highly unnatural. Furthermore, Monte Carlo simulations, due to its nature, cannot be performed under parallel processing; this significantly increases computer resource required and slow down the simulation process.

In EF-MD, molecular movement is driven by external force field, e.g. by specifying acceleration factor. While this allows the simulation to be ran continuously without relying on Monte Carlo charging, applying acceleration to all molecule directly in the flow direction could have adverse effects of clouding the actual transport phenomena. All molecules, regardless of phase or location, are being pushed at the same acceleration drive. While other forces, e.g. tube walls, are also acting upon these molecules to differentiate their transport behavior, there is a sensitive need to suppress the external force field such that it does not wholly overwrite the transport behavior.

This research attempts to avoid pitfalls of both DCV-GCMD and EF-MD; in other words, there is a need to run a continuous simulation in time (MD) without relying on direct acceleration of the molecules or Monte Carlo steps. This has been achieved by creating piston-like frame structure where single-wall carbon nanotube is sandwiched between a source and a sink tank, similar to DC-GCMD set up but with a 'mobile wall' at the edge of the source tank. This wall moves across the source tank, inducing pressure gradient across the tube, and induce a continuous flow through it (Figure 3.a). The ability to create gradient without relying on Monte Carlo process has reduce the simulation resource considerably.

The piston simulations have been completed with Molecular Dynamic simulation program 'Gromacs'. Multiple simulations have been run to investigate sensitivity on pressure, pressure gradient, and wall interactions. Isothermal condition was maintained with the simulation's thermal coupling capabilities, while period of constant average pressure and pressure gradient were extracted manually for analysis after the simulation has finished. The temperature chosen was 353 °Kelvin (175 °F) and the pressure range is between 1700-3500 psi, to mimic generic shale reservoirs condition.

Analysis of average density and velocity profiles were performed using in-house written program, reading and processing location and velocity vectors of selected molecules within the tube at each time step of the simulation.

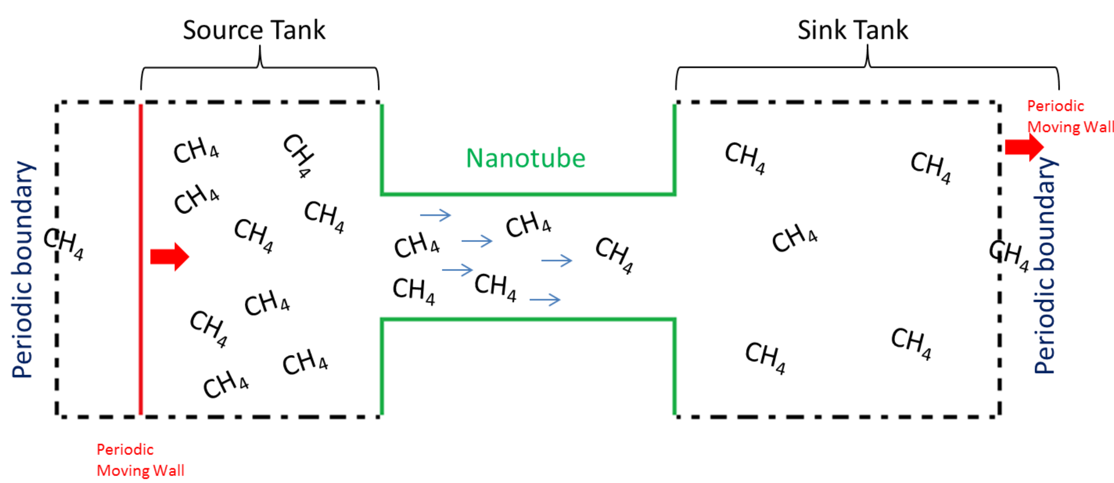

Figure 3.a: Two-dimensional schematic of the piston system (Original Figure, Riewchotisakul, 2015). Moving wall induces methane flow across the carbon nanotube.

The simulation procedures are summarized as follows:

1. Creating a nanometer-scale carbon tube to simulate a kerogen organic pore, possibly connected to a source and sink tank of the flow. A fixed piston-shape frame will be constructed (Fig 3.b), having a carbon nanotube in the center of two tanks, divided by a mobile wall with periodic boundary conditions. The carbon nanotube will represent kerogen pore in its simplest form. The mobile wall, dividing the source and sink tank periodically, will move towards the tube to induce the flow.
2. The whole system was charged and equalized with methane molecules; the number of molecules, along with experimental temperature in the simulator, will determine the system pressure. The charging process was performed using Grand Canonical Monte Carlo simulation generating molecular location inside the tube and, subsequently, another equilibrium simulation is run at the desired temperature using Gromacs. (Figure 3.c) demonstrates the charged condition of the system.
3. After the source and sink tanks are charged with methane molecules and allowed to reach equilibrium, the mobile wall located at the outermost end of the tanks was pulled at a designated center of mass, COM, velocity towards the tube. This will create a piston-like effect, resulting in volume reduction in the source tank and expansion of the sink tank due to periodic boundary conditions. This volume change translates to increase of pressure in the source tank and decrease of pressure in the sink tank, essentially subjecting a

constant pressure gradient and inducing a steady flow across the tube. As molecules move across the tube, pressure will decrease in the source tank and increase in the sink tank; this will counter the volume change described above. Essentially, the piston should be move at controlled velocities to achieve a steady-state condition, in which pressure in the source and sink regions are maintained and relatively constant pressure gradient is induced. Temperature (kinetic energy of the molecules) will be held relatively constant during the simulation by temperature coupling function.

Note that the average pressure can be varied during the charging step by changing the number of methane molecules in the system. Additionally, the pressure gradient was varied by changing the COM velocity at which the moving wall is pulled.

4. In order to induce and maintain steady-state flow through the tube, the induced wall COM velocity needs to be carefully chosen. A wall velocity that is too fast will continuously increase the source tank pressure and eventually sandwich the molecules between the moving and stationary walls; a wall velocity that is too slow will result in molecules equalizing across the tube before pressure gradient can be maintained, resulting in net zero flow. Multiple COM velocity was tried for each run and the few yielding steady pressure gradients are chosen for the flow analysis. To ensure the stability of steady-state condition, an in-house program is used to keep track of the average pressures in the source and sink tanks at each time step by reading

the output trajectory file in which molecule location and velocities are recorded for the all of the molecules at all times. This allows proper selection of moving the wall speed and identification of the steady-state flow period for the analysis. These calculations of pressure gradient across tube are outlined in section 4. Pressure gradient used for analyses are plotted in Figure 5.a.1-5.a.3.

5. Once the steady state flow period is identified, the simulation results of those periods were extracted as a separate trajectory file containing locations and velocities of the molecules to be used in the investigation.

6. The steady-state trajectories were then used to calculate the average methane density and velocities for each section of the tube during the flow. This is performed through another in-house program (refer to section 4) where the tube sections are divided as cylindrical shell with the outermost shell representing the adsorbed phase (Figure 4.b). The result is an average density and velocity profile across the tube radius (Fig 5.b.1-5.b.3 and 5.c.1 – 5.c.3).

7. The simulations are repeated for different values of average pressure and pressure gradient. Additionally, the 3500 psi average pressure simulations were ran with sensitivity analysis by varying the wall carbon molecules; in this case, the epsilon factor in the Lennard-Jones potential function was varied.

8. From the averaged profile data, transport mechanism of adsorbed phase and its effect on the bulk phase are identified and analyzed (refer to Section 5).

The analysis of simulation results aims to make sense of flow results from different pressure and pressure gradients such that the effects of adsorbed phase transport on bulk phase and total flow, if exists, can be quantified in equation form, similar to other wall effects such as Klinkenberg slippage factor and its correction (Fathi Tinni and Akkutlu, 2012).

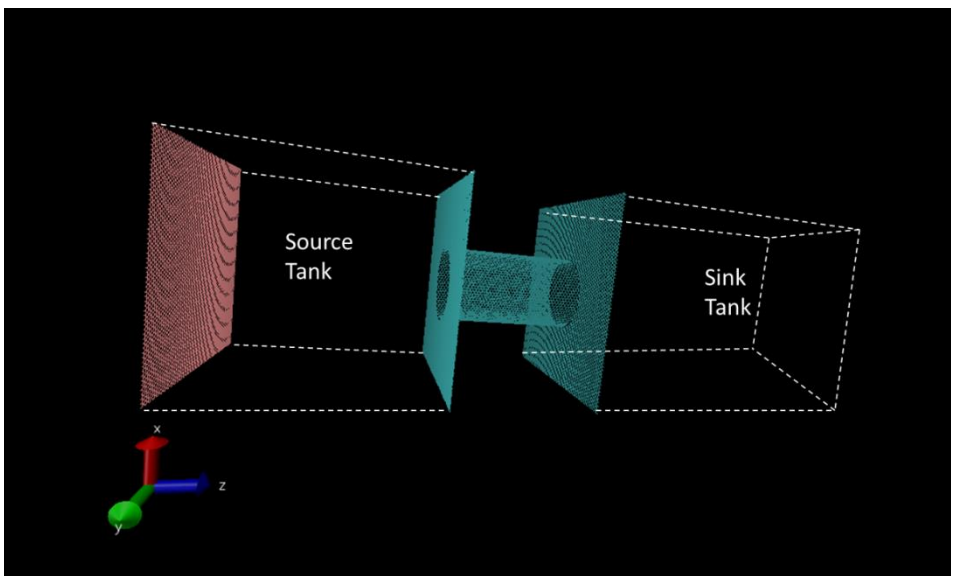

Figure 3.b: Piston frame in simulation set up (Original Figure, Riewchotisakul, 2015). The green wall and tube represents carbon and the red wall is the moving piston. Periodic boundaries are shown in white dash lines.

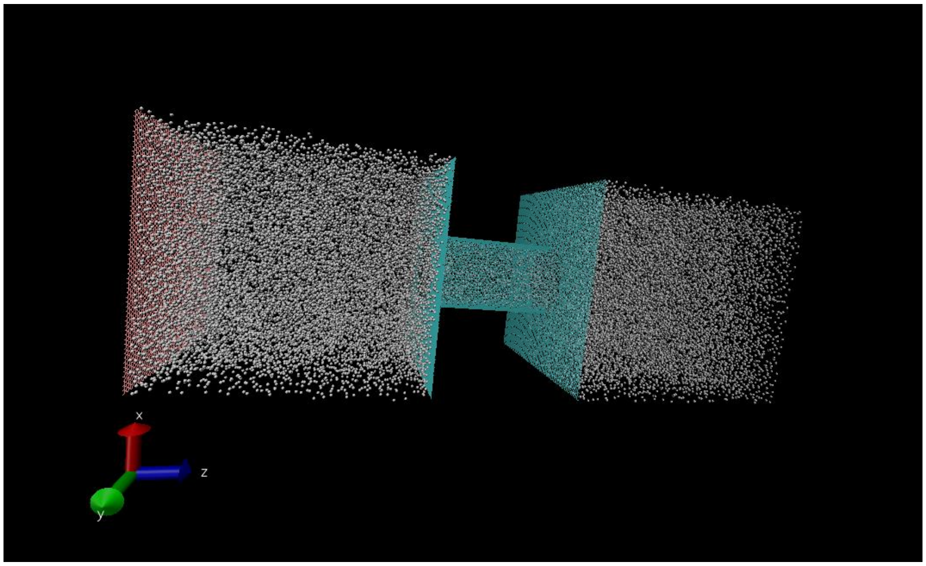

Figure 3.c: Piston frame charged with methane molecule (Original Figure, Riewchotisakul, 2015). In this example, the charging pressure is 3500 psia and temperature is 353 °Kelvin (175 °F).

4 IN-HOUSE NUMERICAL ANALYSIS PROGRAMS

Two sets of in-house program and calculation spreadsheets are written with the specific purpose of:

(1) Analyzing the pressure in the source and sink tank at each recorded time of the simulation runs. An example of analysis results in shown in Figure 5.a.1-5.a.3.

(2) Averaging the density and velocity of Methane molecules during the steady state flow period. This was performed by dividing the volume inside the tube multiple cylindrical shell volumes, before taking time-average of each shell (Figure 4.a). The results are shown in Figure 5.b's and Figure 5.c's.

Both programs utilized the simulation trajectory file, a record of molecule location and velocity at each time step of the simulation.

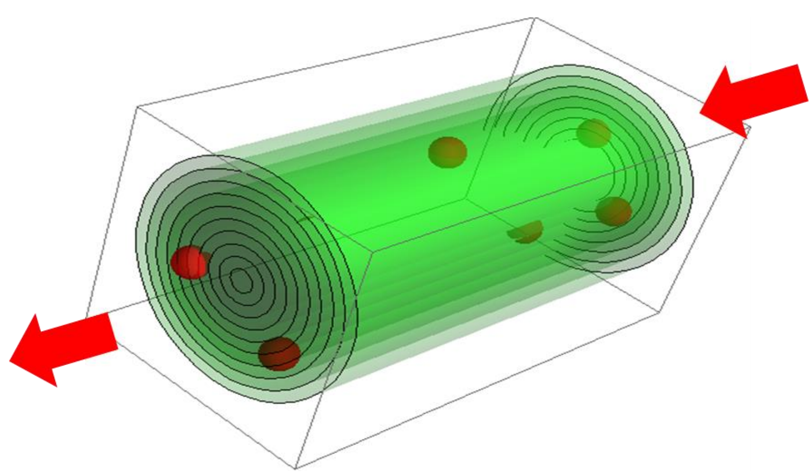

Figure 4.a: Numerical analysis scheme (Original Figure, Riewchotisakul, 2015). Number of molecules and their velocities in each green cylindrical shell region will be averaged during steady-state flow.

5 RESULTS

The data for analysis are selected from steady-state flow period of the simulation, where pressure and pressure gradient are kept constant. Examples of selected steady state regions for three average pressures are shown in Figure 5.a.1-5.a.3 below.

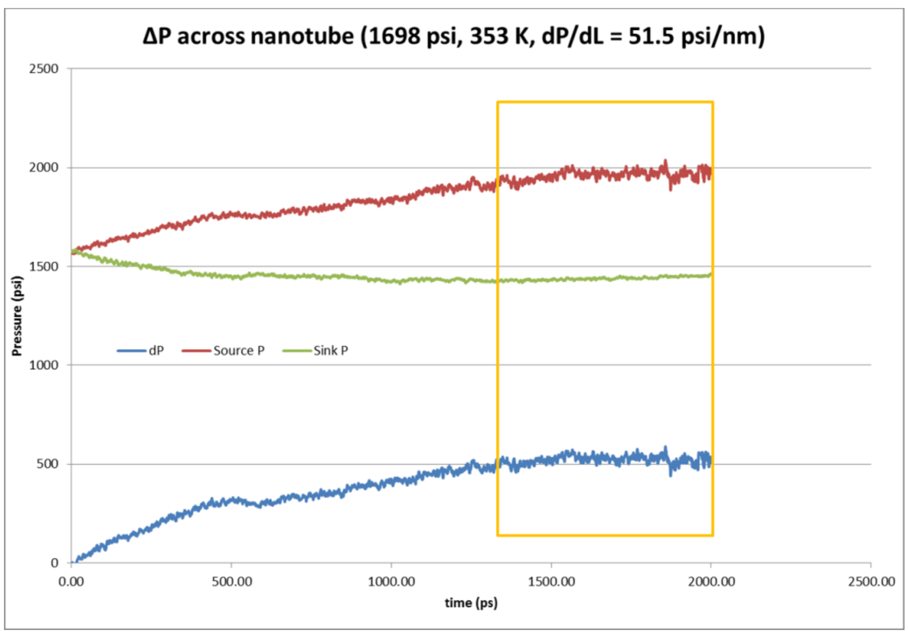

Figure 5.a.1: Tank pressure difference at average pressure of 1698 psi (Original Figure, Riewchotisakul, 2015). Above is a sample pressure record of source tank, sink tank, and their difference during simulation period. The steady state period, highlighted in yellow box, is selected for analysis.

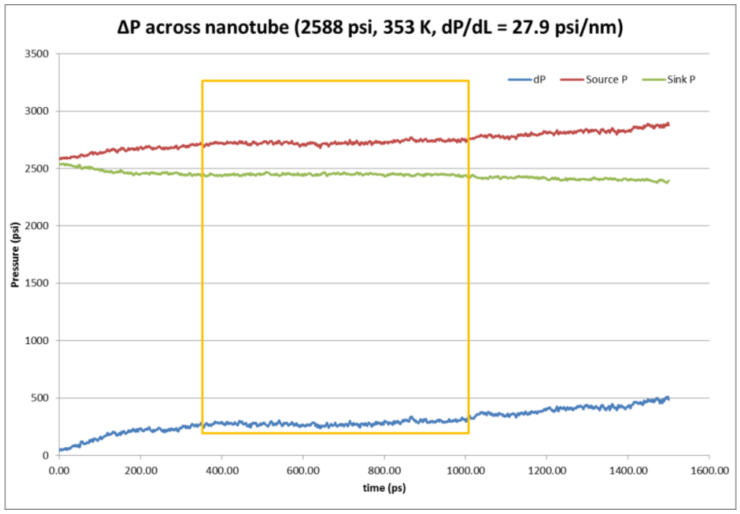

Figure 5.a.2: Tank pressure difference at average pressure of 2588 psi (Original Figure, Riewchotisakul, 2015).

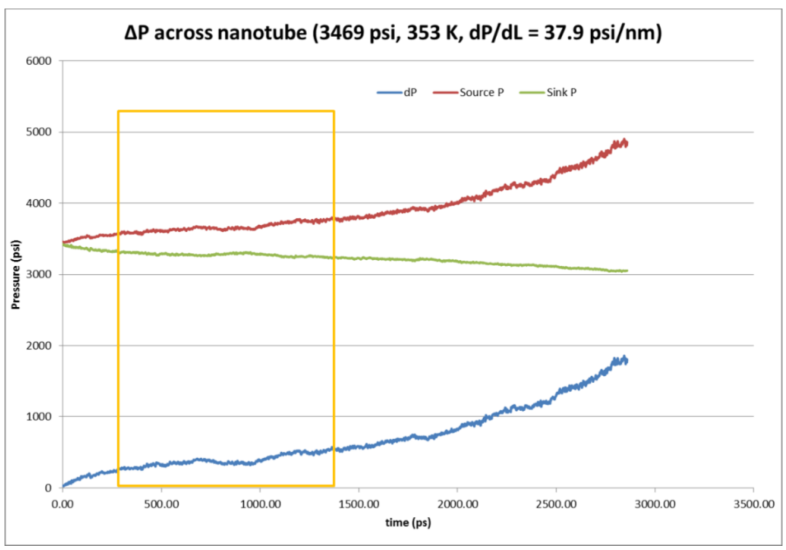

Figure 5.a.3: Tank pressure difference at average pressure of 3469 psi (Original Figure, Riewchotisakul, 2015).

5.1 Identification of Bulk and Adsorbed Phase Regions

Using the simulation results processed through in-house program, two distinct fluid phases are observed from the spike in the plots: the bulk phase in the center of the tube and the single-layer, dense, adsorbed phase along the wall (Figure 5.b.1-5.b.3). The densities of bulk phase are compared to correlation values calculated based on Methane with real gas laws, assuming equivalent average pressure (averaged between the source and the sink tank) and using z-factor correlation from NIST SUPERTRAP; these bulk phase density values demonstrated very close match at all pressures.

As predicted by literature (Rahmani and Akkutlu, 2013), the transition region is observed between adsorbed phase and bulk phase. Their density in this case, however, is very close to the bulk phase such that it should not introduce major deviation to Langmuir's binary-mode assumption.

From the comparison between different pressure and gradients (Figure 5.b.4-5.b.5), it was observed that the density profile varies negligibly with pressure gradient, i.e. the difference between the source and sink concentration, but is strongly dependent on the average pressure.

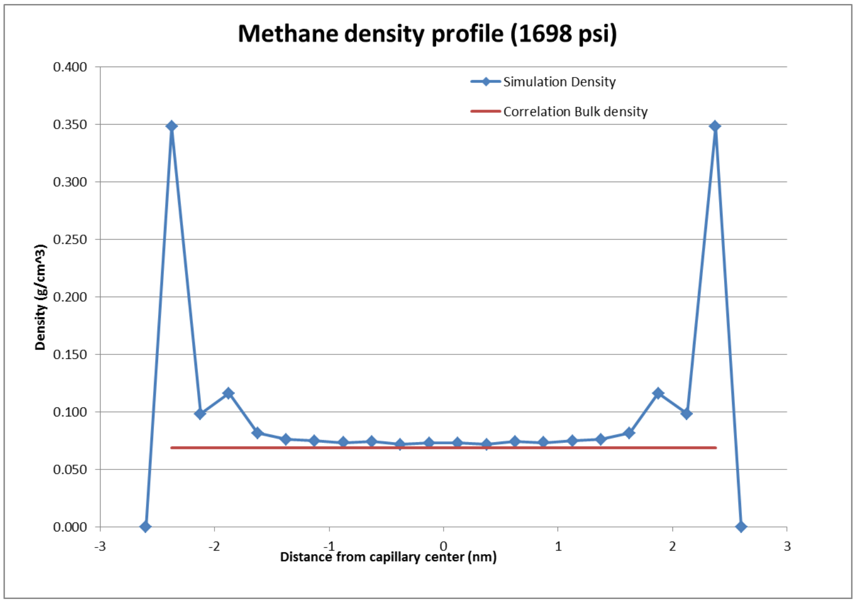

Figure 5.b.1: Density profile for a simulation at 1698 psi (Original Figure, Riewchotisakul, 2015). The Adsorbed phase high density is shown at the tube wall (edge) while the lower bulk phase density is in the middle of the tube. The red line represent Methane density calculated using real gas law at similar pressure and temperature. The bulk phase simulation density and correlated values shows very close match.

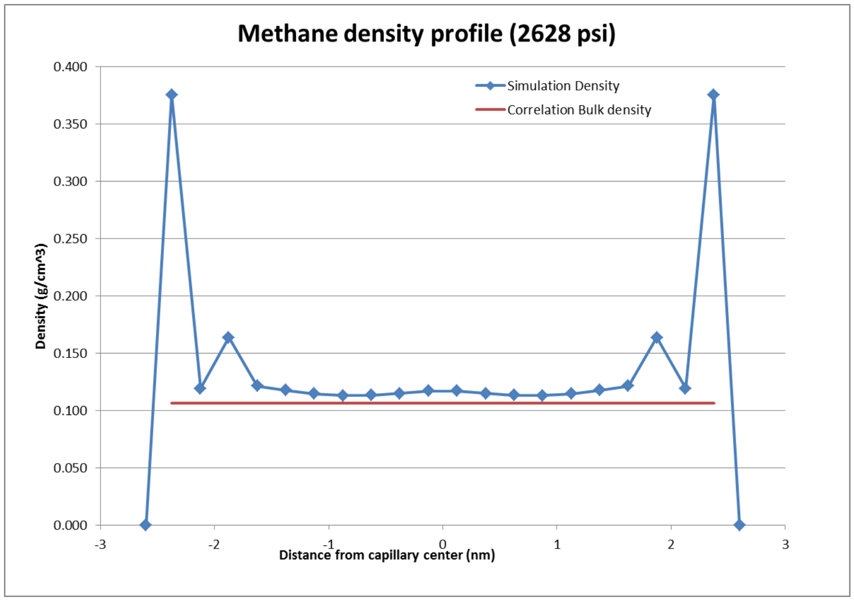

Figure 5.b.2: Density profile for a simulation at 2628 psi (Original Figure, Riewchotisakul, 2015). Plot legend is similar to 5.b.1. The bulk phase simulation density and correlated values shows very close match.

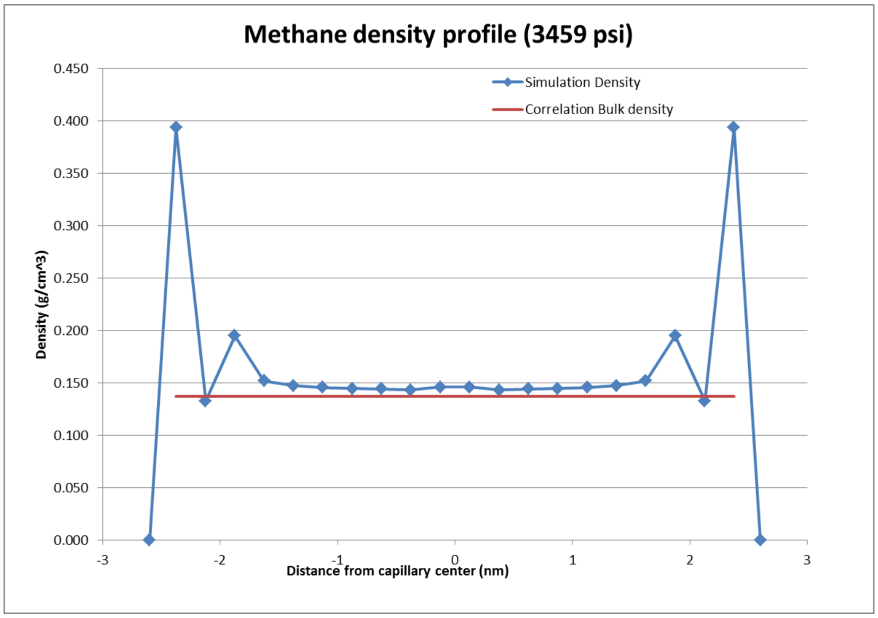

Figure 5.b.3: Density profile for a simulation at 3459 psi (Original Figure, Riewchotisakul, 2015). Plot legend is similar to 5.b.1. The bulk phase simulation density and correlated values shows very close match.

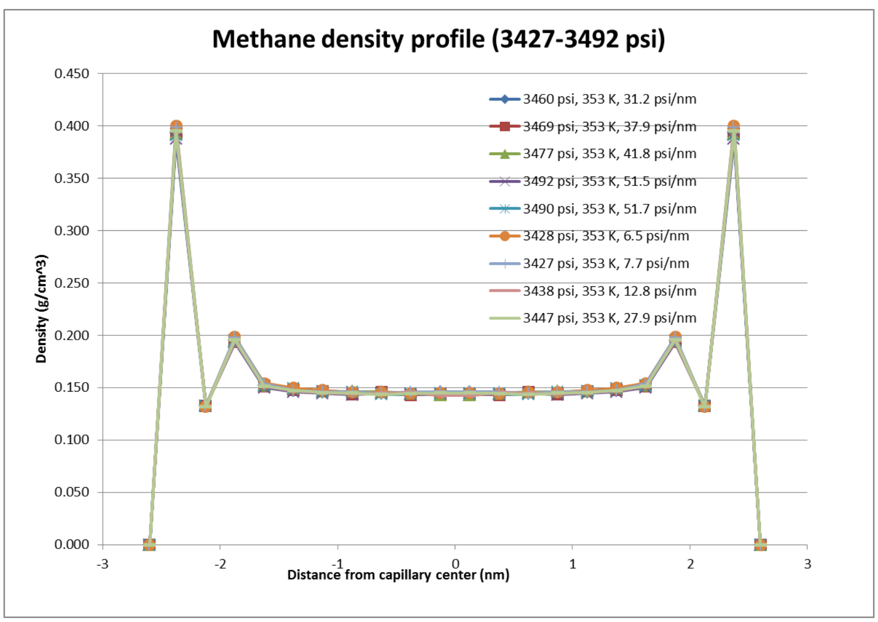

Figure 5.b.4: Density profile for a simulation at 3427-3492 psi (Original Figure, Riewchotisakul, 2015). Phase density shows negligible sensitivity to pressure gradient, and little variation as long as average pressure is maintained.

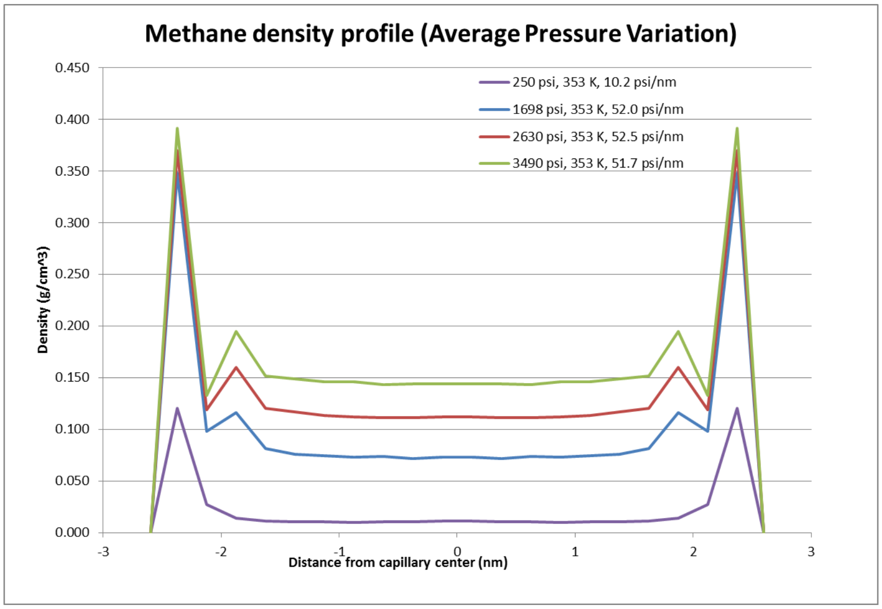

Figure 5.b.5: Density profile for a simulation at different average pressure (Original Figure, Riewchotisakul, 2015). Additional result from 250 psi simulation is included. Distinct bulk phase density differences are observed for each average pressure, matching their expected values from real gas law correlation. In contrast to low pressure simulation at 250 psi, the adsorbed phase density between 1698-3490 psi has little differences; this shows that for the selected simulation condition, the adsorbed phase has already reached saturation.

5.2 Velocity Profile Trends

The average velocity profiles through the tube were calculated using in-house program ‘Average Tube Profile’. Each profile was plotted against density and classical laminar-flow Hagen-Poiseuille velocities at equivalent average pressure and pressure gradient. Examples of these comparisons are shown below in (Figure 5.c.1 – 5.c.3); complete velocity profiles from each simulation are provided in Appendix A.

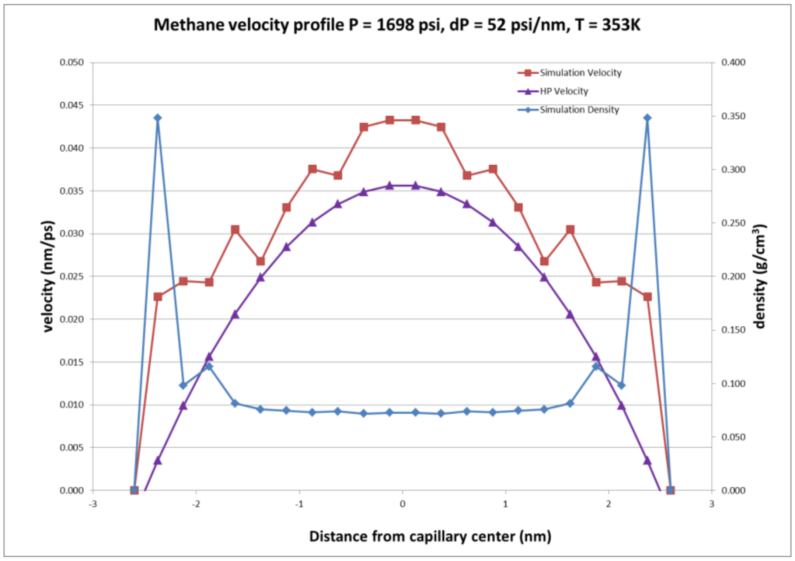

Figure 5.c.1: Velocity profile at average pressure of 1698 psi (Original Figure, Riewchotisakul, 2015). Temperature is at 353 °K and pressure gradient is 52 psi/nm. Note the simulated velocity (red) is positive for adsorbed phase and higher than classical Hagen-Poiseuille velocity (purple).

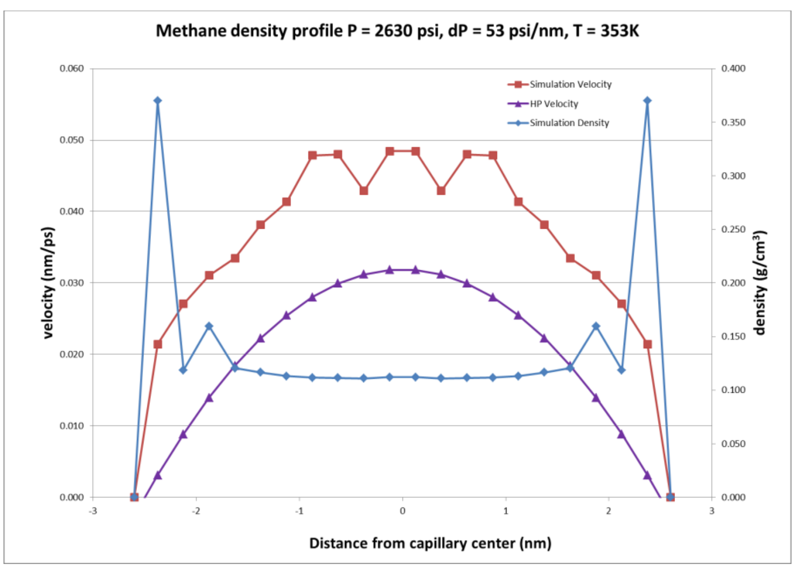

Figure 5.c.2: Velocity profile (red) at average pressure of 2630 psi (Original Figure, Riewchotisakul, 2015). Temperature is 353 °K and pressure gradient is 53 psi/nm. Density profile (blue) identifies the phases. Comparison is shown with classical Hagen-Poiseuille velocity (purple).

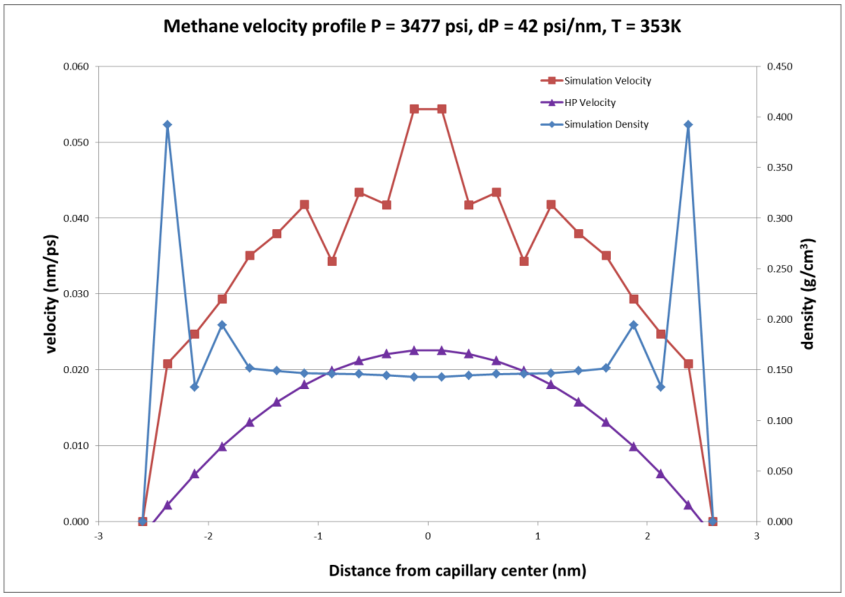

Figure 5.c.3: Velocity profile (red) at average pressure of 3477 psi (Original Figure, Riewchotisakul, 2015). Temperature is 353 °K and pressure gradient is 42 psi/nm. Density profile (blue) identifies the phases. Comparison is shown with classical Hagen-Poiseuille velocity (purple).

Many significant phenomena can be observed from these velocity profiles. First and foremost, all profiles demonstrated positive velocities, towards the sink, at the outermost layer. This shows that the adsorbed-phases by the capillary walls are not stationary, but move alongside the bulk phase near the walls with comparable velocities due to the pressure gradient.

Secondly, all of the parabolic velocity profiles obtained are significantly higher than the classical profiles expected from Hagen-Poiseuille equation with the same average pressure and gradient values. This clearly demonstrates flow enhancement in the bulk phase in the presence of adsorbed layer, regardless of pressure or gradient. The effect is compounded by the fact that adsorbed phase is much denser than the bulk phase, giving additional mass transfer across the tube.

The velocity profile heavily depends on the gradient, as demonstrated from Figure 5.d.1-5.d.3, where higher gradient increase the parabolic velocities uniformly for each average tube pressure. The profile seems to also be affected by the average pressure across the capillary; results with equivalent gradients shows higher velocity trend with higher average pressure (Figure 5.d.4).

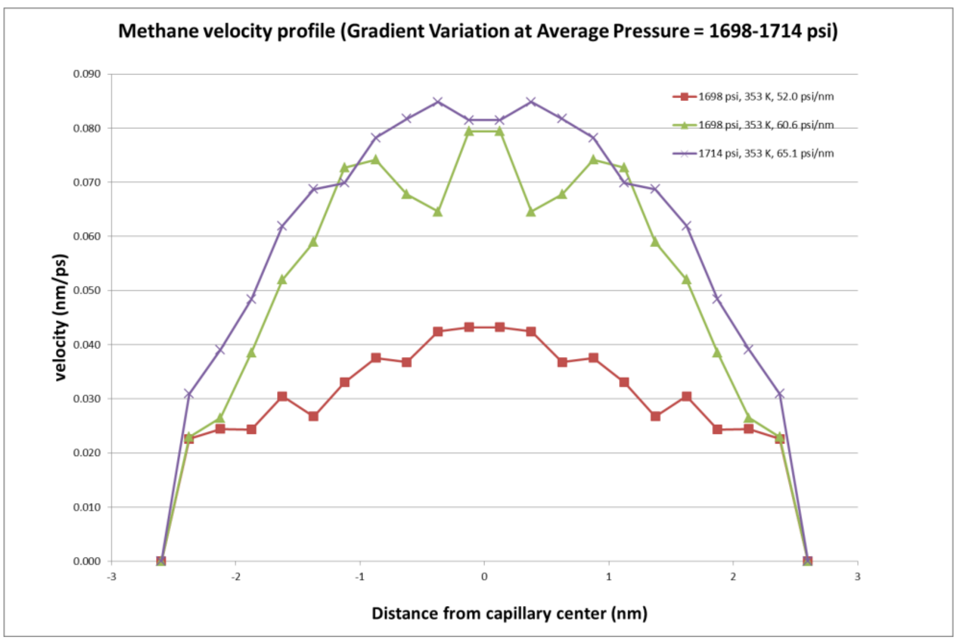

Figure 5.d.1: Velocity profile comparison for different pressure gradient at average pressure of 1698-1714 psi (Original Figure, Riewchotisakul, 2015).

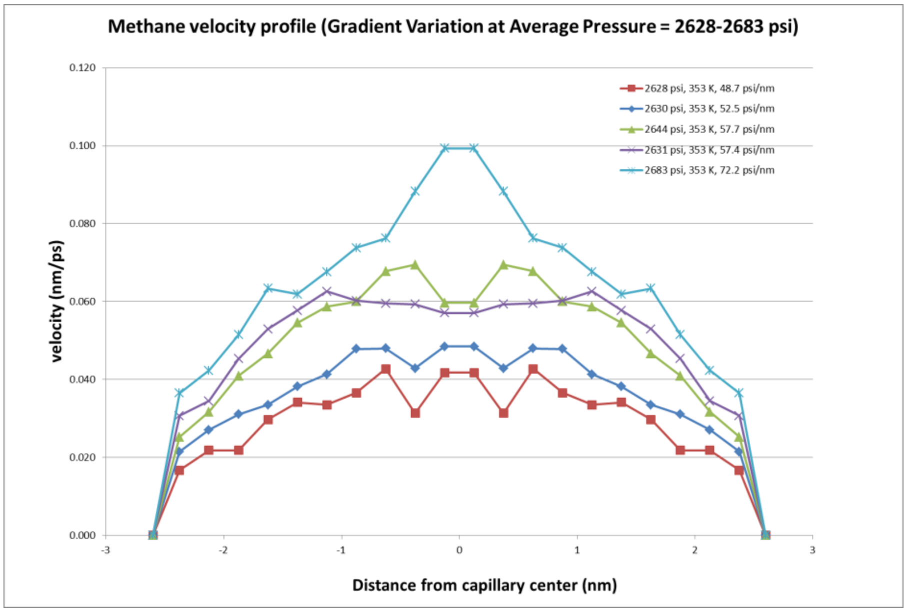

Figure 5.d.2: Velocity profile comparison for different pressure gradient at average pressure of 2628-2683 psi (Original Figure, Riewchotisakul, 2015). The velocity increases along with the gradient.

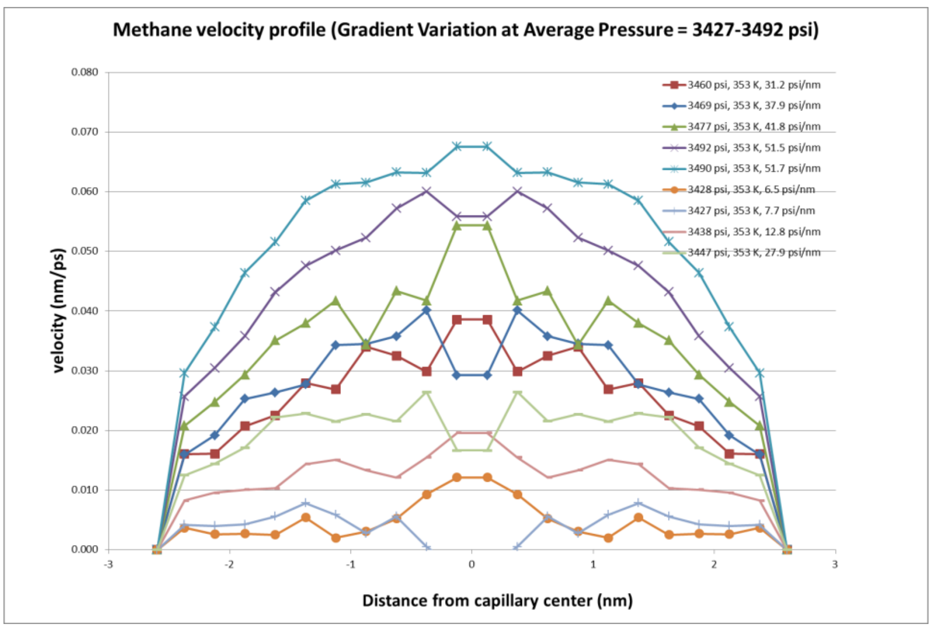

Figure 5.d.3: Velocity profile comparison for different pressure gradient at average pressure of 3427-3492 psi (Original Figure, Riewchotisakul, 2015). The velocity increases along with the gradient.

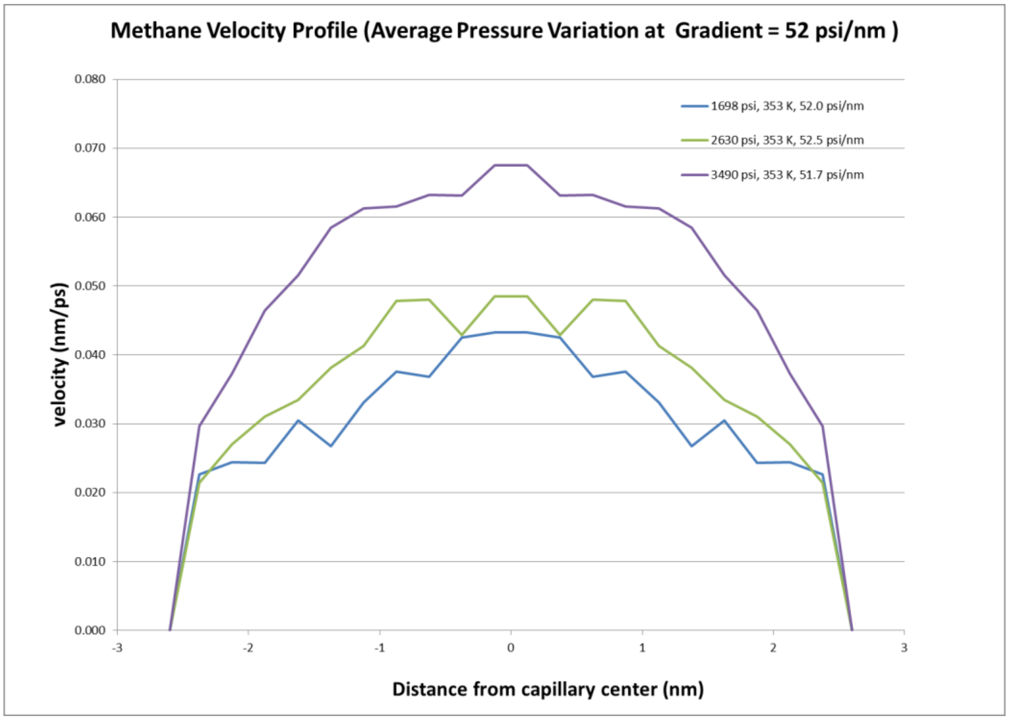

Figure 5.d.4: Velocity profile comparison for different average pressure at equivalent gradient of 52 psi/nm (Original Figure, Riewchotisakul, 2015). The velocity increases along with average pressure.

5.3 Quantifying Mass Transport Enhancement

In order to quantify the increase in mass transfer across the tube of each simulation result with respect to classical laminar flow model, a dimensionless factor dubbed "Mass Transport Enhancement Ratio" is established. The formula for R_{me} is:

$$R_{me} = \frac{M_{total}}{M_{HP}} = \frac{\sum_i^n \rho_i A_i \, v_i}{\rho_{bulk} Q_{HP}} \tag{21}$$

Here, M_{total} is the total mass transfer rate in the tube, represented by dot product of density (ρ_i), cross sectional flow area (A_i), and velocity (v_i) of each cylindrical shell layer inside the tube. The denominator, a classical Hagen Poiseuille-model mass transfer, is simply a product of bulk phase density (ρ_{bulk}) and the Hagen-Poiseuille volumetric flow rate calculated at the same pressure gradient, average pressure, and temperature.

R_{me} essentially measures the increase in mass transfer, as a multiplication factor, between simulated two-phase (bulk and adsorbed) flow and a conventional single-phase laminar flow under the same drive and thermodynamic conditions.

Plot of R_{me} for each simulation results are shown in Figure 5.e.1. The values are fairly constant around 3.5 for 5-nm tube. Average pressure seems to have negligible effects, with slight dependent on pressure gradient. The mean value obtained is 3.44, with standard deviation of 0.48 and coefficient of variation of 13.98%.

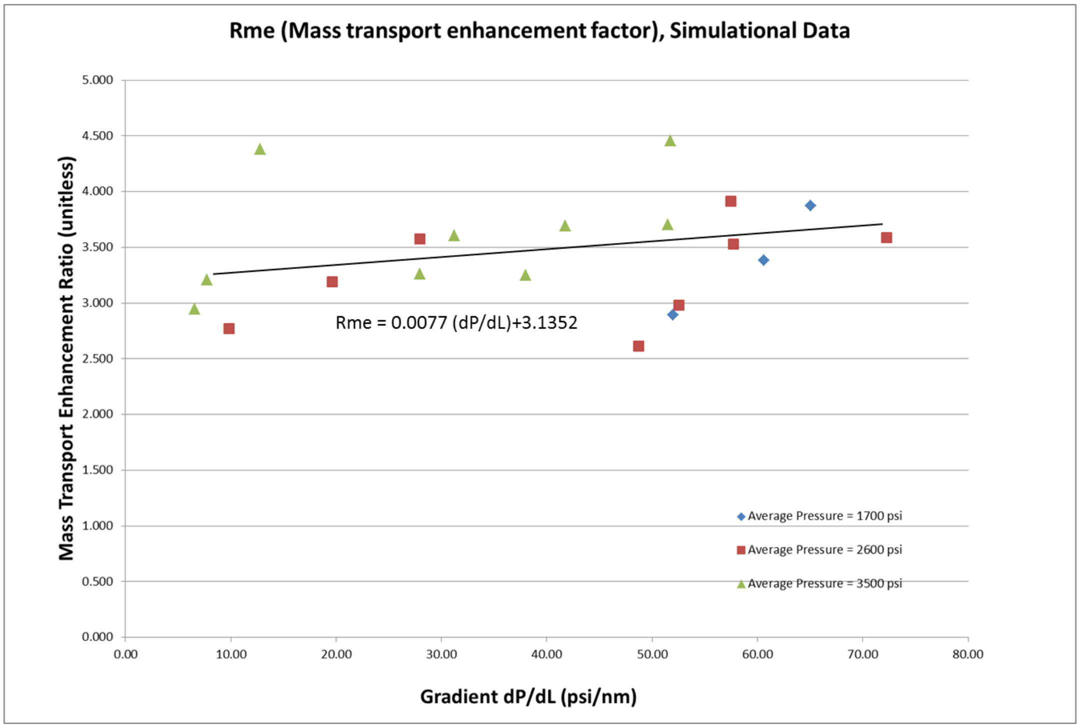

Figure 5.e.1: Mass transport enhancement ratio plotted against pressure gradient (Original Figure, Riewchotisakul, 2015). Three average pressure sets are shown in different color icons.

5.4 Linear Dependence of Adsorbed Phase Velocity

The average velocities of the outer most layer, i.e. adsorbed phase, is plotted against pressure gradient in Figure 5.f.1-5.f.2 for all average pressures. It is observed that the adsorbed phase velocity is strongly linearly-dependent on the pressure gradient but does not vary significantly with the average pressure. We compare this with the simplified mechanistic velocity equation (20) from previous section. In contrast to the mechanistic model, the Langmuir b constant in the denominator seems to be so low such that the effects of the pressure have been reduced to negligible magnitude. In this case, the adsorbed phase flux relationship becomes:

$$J_s = \left[\frac{C_{sv}}{A_s}\right]\frac{dP}{dL} \tag{22}$$

C_{sv} is a constant dependent on temperature and specific molecule-wall interactions and A_s the cross sectional area of the flux. For the 5-nm tube at 353 °Kelvin, $C_{sv} = 0.0004593\ \frac{nm^2}{picosecond\ psi}$ and $\frac{C_{sv}}{A_s} = 0.0001231\ \frac{1}{picosecond\ psi}$, which corresponds to the volumetric flows.

This linear relationship can be determined from the simulation, and is an essential part for quantification of the flow enhancement in terms of dimensionless multiplication factor, as demonstrated in the next section.

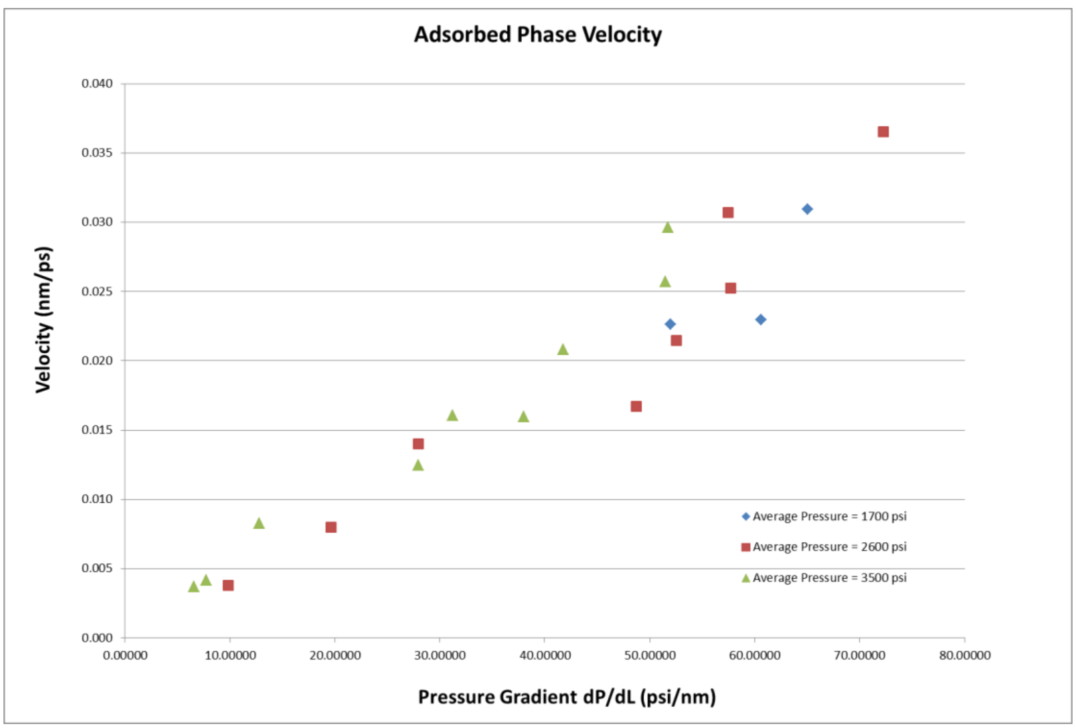

Figure 5.f.1: Adsorbed phase velocity plotted against pressure gradient (Original Figure, Riewchotisakul, 2015). Pressure does not seem to correlate much.

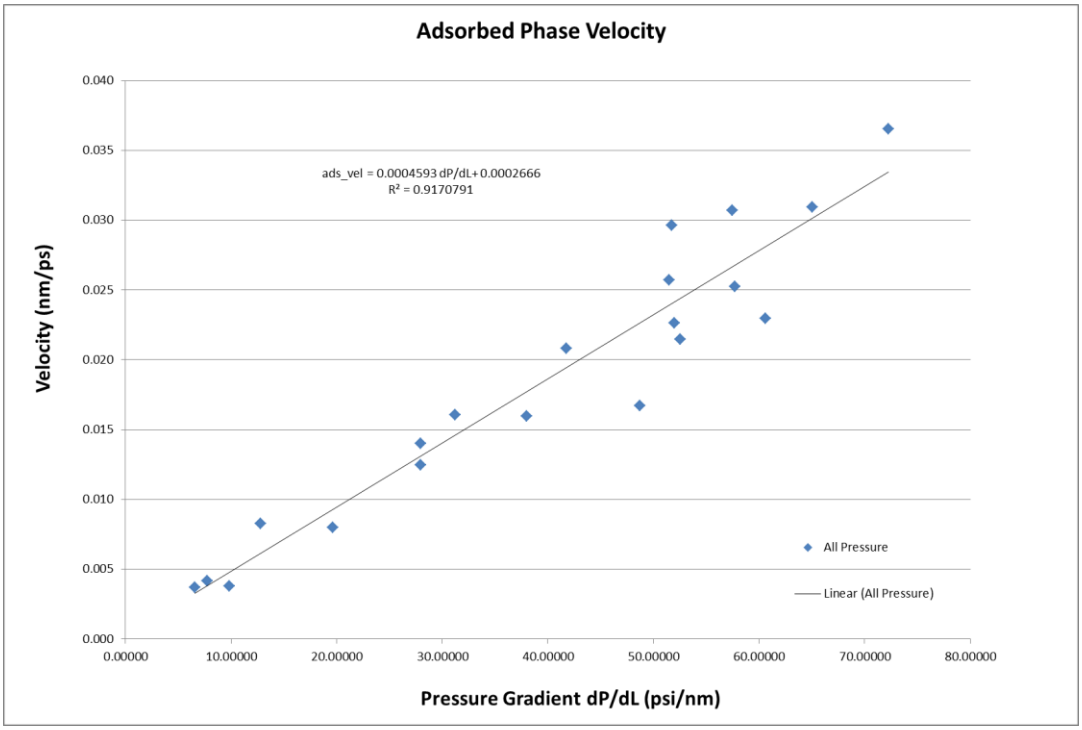

Figure 5.f.2: Regression fit of adsorbed phase velocity (Original Figure, Riewchotisakul, 2015). The relationship between velocity and gradient is highly linear, regardless of average pressure.

5.5 Velocity Enhancement in the Bulk Phase

An interesting relationship is observed when analyzing the transport enhancement in the bulk region. When the adsorbed layer velocity is added to classical Hagen-Poiseuille velocity, the resulting profile closely follows the enhanced bulk phase velocity profile. In other words, the total velocity enhancement in the simulations is a direct superposition of adsorbed phase velocity on the classical laminar flow. The match was reasonable in all the simulation cases investigated except at extremely low gradient where viscous flow devolve to diffusion and a ‘profile’ no longer exists. Example is shown below in Figure 5.g.1: a comparison between the superpositioned Hagen-

Poiseuille velocity profile and the velocity from simulation. Complete superpositioned profiles are provided in Appendix B.

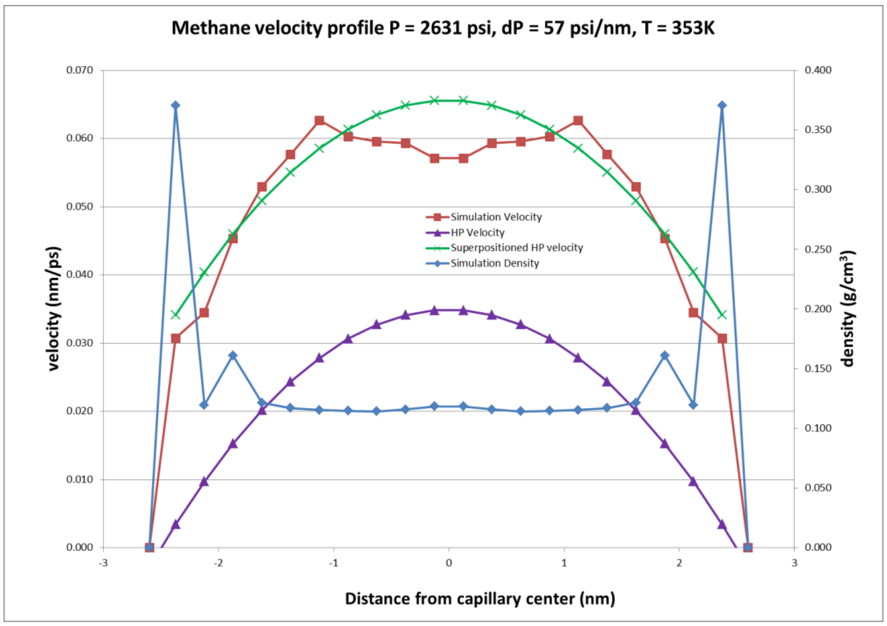

Figure 5.g.1: Superpositioned velocity (Original Figure, Riewchotisakul, 2015). Comparison between Hagen-Poiseuille velocity superpositioned with adsorbed phase velocity (green) and velocity profile obtained from simulation (red). They result in a very close match.

This observation could be rationalized by comparing the mobile adsorbed phase to a moving capillary wall. When the bulk molecule collide (or 'hop') on top of the dense adsorption layers, it gains additional momentum from the movement of the layer in the flow direction much like a ping pong ball bouncing off a moving walkway. During the steady-state flow the momentum shared between the two phases reach a quasiequilibrium such that sum of the adsorbed phase velocity and the velocity to the bulk phase becomes constant.

Many velocity profiles show slight decrease in slope in the area where adsorbed phase transitioned into bulk phase. This may suggest presences of slippage-like effects between the bulk phase and the adsorbed layer, with the latter acting much like a moving walkway. However, all the velocities showed high consistency with superpositioned profile, demonstrating that this slippage effect is minimal.

This observation serves as a backbone in formulating the equation of transport in nano-scale capillaries as detailed in the next section.

5.6 Effects of Wall Properties on Velocity

Sensitivity analysis was performed at an average pressure of 3500-psi across the tube by varying the level of molecular interactions. In our simulations these interactions are introduced using energy sink parameter ε of the Lennard-Jones potential function. It was observed that the parameter has an inverse relationship with the transport enhancement; higherε, i.e. higher interaction between Methane and the wall, yields lower adsorbed phase velocity and lower velocity profile. The storage, however, is positively affected by increase in the potential; higher ε yields higher adsorbed phase density, meaning more molecules stored along the surface of the capillary walls. Comparison of these density and velocity profiles are shown in Figure 5.h.1 and 5.h.2.

The C_{sv}/A_s values, calculated from adsorbed phase velocity are compared with the change in ε in Figure 5.h.3; the two factor exhibits an inverse power-law relationship, suggesting that ε may be directly proportional to the molecule-surface interaction energy E from the mechanistic model of diffusivity coefficient.

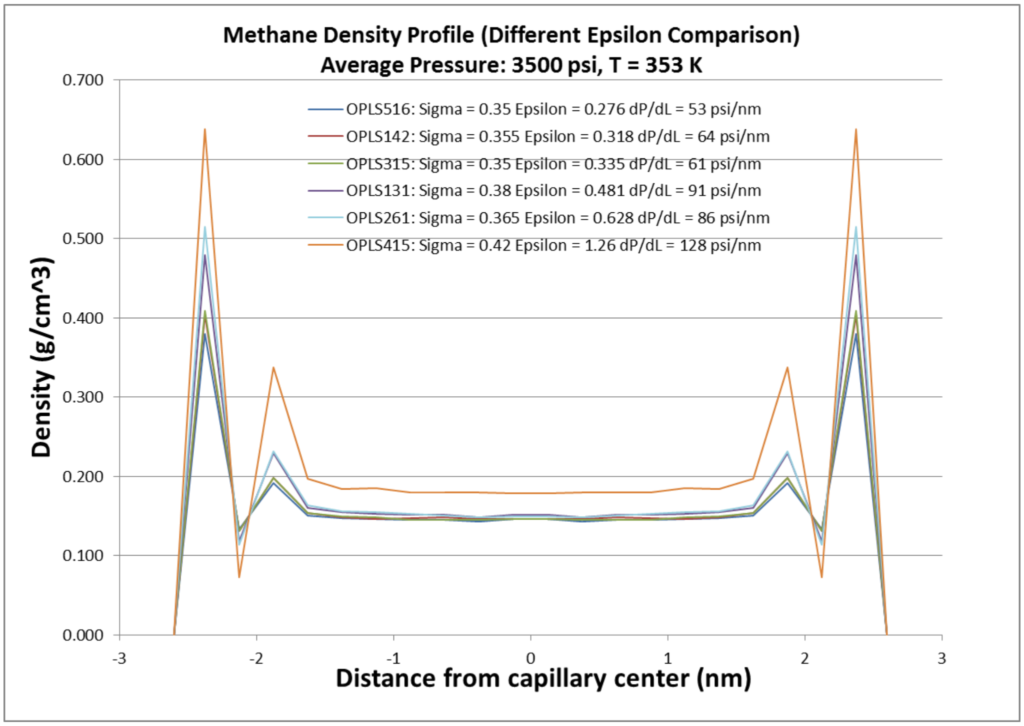

Figure 5.h.1: Variation of density profile with epsilon (Original Figure, Riewchotisakul, 2015). Higher epsilon, the molecular interaction coefficient, yields higher density in the adsorbed phase.

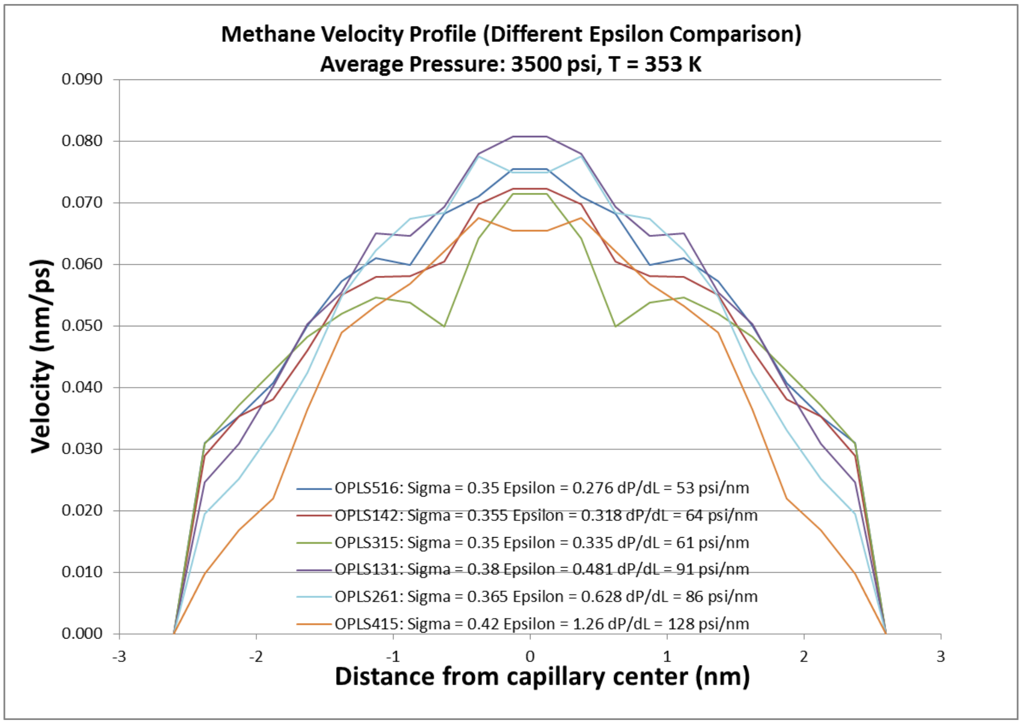

Figure 5.h.2: Variation of velocity profile with epsilon (Original Figure, Riewchotisakul, 2015). Higher epsilon results in higher attraction to the wall and less mobility, lowering the velocity of the adsorbed phase. Notice the lowest velocity profile at Epsilon = 1.26 despite having over two times the gradient as the highest velocity.

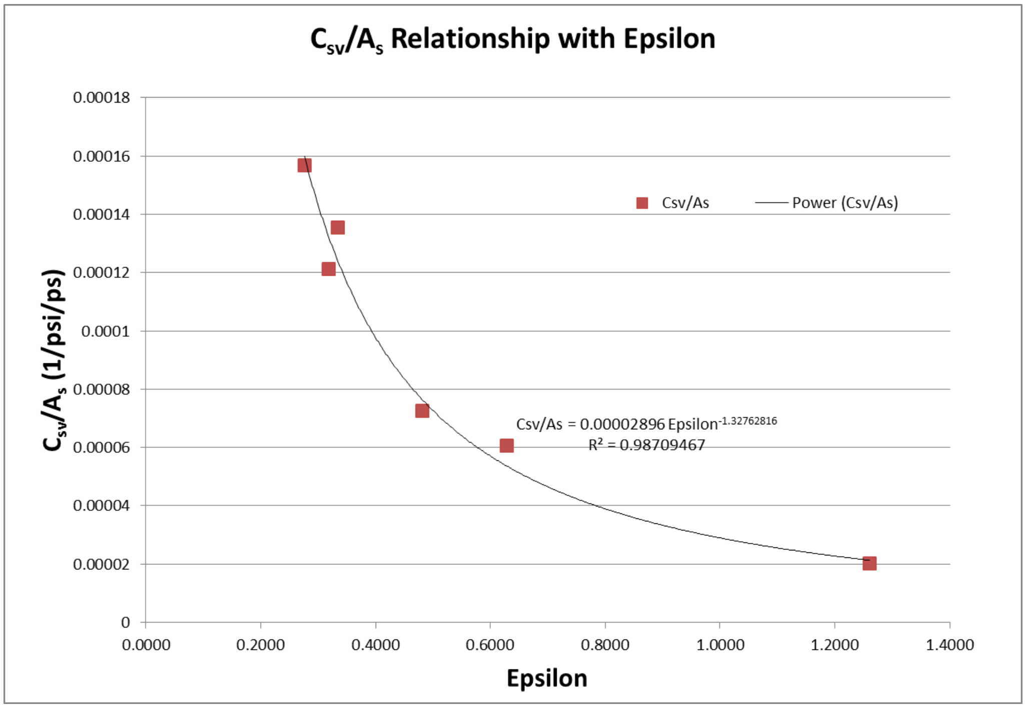

Figure 5.h.3: Plotted adsorbed phase velocity constant (C_{sv}/A_s) against epsilon (Original Figure, Riewchotisakul, 2015). The result yields inverse relationship in power-law fashion.

6 MASS TRANSPORT ENHANCEMENT RATIO

6.1 Correlation

Based on the observation that the two-phase velocities being a superposition of the Hagen-Poiseuille velocity over the adsorbed phase velocity, as observed readily from the computed velocity profiles, a correlation for mass transfer increase due to the adsorbed-phase could be proposed.

The two-phase mass transfer through the tube is the sum of bulk phase mass transfer rate and adsorbed phase mass transfer rate:

$$M_{total} = M_{bulk} + M_{ads} \tag{23}$$

This can be converted to volumetric rate if the difference between the bulk and the adsorbed phase density values is known. The simple relationship between a mass transfer rate (M) and a volume transfer rate (Q) of a phase is dependent on the density (ρ) of that phase as follows:

$$M = \rho\, Q \tag{24}$$

Let us define Q_{total}, the total volume transfer with respect to the bulk phase density as:

$$M_{total} = \rho_{bulk} Q_{total} \tag{25}$$

Substitution of volume transfer rate yields:

$$Q_{total} = \frac{1}{\rho_{bulk}} M_{total} \tag{26}$$

$$Q_{total} = \frac{1}{\rho_{bulk}}(M_{bulk} + M_{ads}) \tag{27}$$

$$Q_{total} = \frac{1}{\rho_{bulk}}(\rho_{bulk}Q_{bulk} + \rho_{ads}Q_{ads}) \tag{28}$$

$$Q_{total} = Q_{bulk} + \frac{\rho_{ads}}{\rho_{bulk}}Q_{ads} \tag{29}$$

The Q's are the volumetric flow (bulk at the center of the tube and adsorbed at the wall), ρ_{ads} is the adsorbed phase density and ρ_{bulk} is the bulk phase density of methane.

Since volumetric flow rate is an integral of velocity over the cross-section area normal to flow:

$$Q = \iint_A velocity\ dA \tag{30}$$

The volumetric flow above can be converted to integral of velocity profile over radius, with area A assume being circular cross sectional area of a tube with radius r.

$$A = \pi r^2 \tag{31}$$

$$dA = 2\pi r dr \tag{32}$$

$$Q_{total} = \int_0^{r_{ads}} (v_{HP} + v_{ads})\ 2\pi r dr + \frac{\rho_{ads}}{\rho_{bulk}}\int_{r_{ads}}^{r_{tube}} v_{ads}\ 2\pi r dr \tag{33}$$

$$Q_{total} = \int_0^{r_{ads}} (v_{HP})\ 2\pi r dr + \int_0^{r_{ads}} (v_{ads}) 2\pi r dr + \frac{\rho_{ads}}{\rho_{bulk}}\int_{r_{ads}}^{r_{tube}} v_{ads}\ 2\pi r dr \tag{34}$$

Here r_{ads} is the radius of the adsorbed layer (single layer away from the tube wall), r_{tube} is the nanotube radius, and v_{HP} and v_{ads} are Hagen-Poiseuille velocity and adsorbed phase velocity, respectively.

From the adsorbed phase velocity correlation in previous section (see Figure 5.f.2), we assumed v_{ads} is a linear function of pressure gradient, that is:

$$v_{ads} = C_{sv}\left(\frac{dP}{dL}\right) \tag{35}$$

Here C_{sv} is a constant velocity factor. The integral for the last two terms can then be simplified:

$$Q_{total} = \int_0^{r_{ads}} (v_{HP})\, 2\pi r dr + v_{ads}\int_0^{r_{ads}} 2\pi r dr + \frac{\rho_{ads}}{\rho_{bulk}} v_{ads}\int_{r_{ads}}^{r_{tube}} 2\pi r dr \tag{36}$$

$$Q_{total} = \int_0^{r_{ads}} (v_{HP})\, 2\pi r dr + v_{ads}\pi(r_{ads}^2) + \frac{\rho_{ads}}{\rho_{bulk}} v_{ads}\pi(r_{tube}^2 - r_{ads}^2) \tag{37}$$

$$Q_{total} = \int_0^{r_{ads}} (v_{HP})\, 2\pi r dr + C_{sv}\frac{dP}{dL}\pi(r_{ads}^2) + \frac{\rho_{ads}}{\rho_{bulk}} C_{sv}\frac{dP}{dL}\pi(r_{tube}^2 - r_{ads}^2) \tag{38}$$

The first term, the integral of the Hagen-Poiseuille velocity over bulk phase, up to the adsorbed layer, represents classic laminar flow through the tube. This can be integrated in the same manner as when Klinkenberg (1941) integrated velocity shell for the description of his slip flow.

Starting from equation (4) from Klinkenberg's derivation of slip flow (1941), the infinitesimal volumetric flow of velocity integrated through the tube with radius r_{tube} during time t is:

$$dv = \frac{-\pi}{2\mu}\left(\frac{dP}{dL}\right) t \int_0^{r_{tube}} (r_{tube}^2 r dr - r^3 dr + 2c\,\lambda r_{tube} r dr) \tag{39}$$

Since slip phenomena does not develop in our case, the equation is reduced to:

$$dv = \frac{-\pi}{2\mu}\left(\frac{dP}{dL}\right) t \int_0^{r_{tube}} (r_{tube}^2 r dr - r^3 dr) \tag{40}$$

Our first integral term in Q_{total} considers tube (Hagen-Poiseuille) velocity over r_{ads}, up until the adsorbed phase region, so the modified integral is:

$$r_{ads} < r_{tube} \tag{41}$$

$$dv = \frac{-\pi}{2\mu}\left(\frac{dP}{dL}\right) t \int_0^{r_{ads}} (r_{tube}^2 r dr - r^3 dr) \tag{42}$$

$$v = \frac{-\pi}{2\mu}\left(\frac{dP}{dL}\right) t (\frac{1}{2} r_{tube}^2 {r_{ads}}^2 - \frac{1}{4} r_{ads}^4) \tag{43}$$

$$v = \frac{-\pi}{8\mu}(2r_{tube}^2 r_{ads}^2 - r_{ads}^4)\left(\frac{dP}{dL}\right) t \tag{44}$$

It is observed that instead of a factor of ${r_{tube}}^4$ in classic laminar flow, we arrived at a factor of $(2\ {r_{tube}}^2\ {r_{ads}}^2 - {r_{ads}}^4)$, relative to the adsorbed phase radius.

From the definition of infinitesimal volumetric flow at time t (v) above and that of Hagen-Poiseuille equation, we can infer that the volumetric flow rate, i.e. an area integral of velocity, up to r_{ads} would be:

$$\int_0^{r_{ads}} (v_{HP})\ 2\pi r dr = \frac{\pi(2r_{tube}^2 r_{ads}^2 - r_{ads}^4)}{8\mu}\frac{dP}{dL} \tag{45}$$

The above is similar to classical Hagen-Poiseuille equation, but with slightly modified tube radius. Combining the term into Q_{total}, we have:

$$Q_{total} = \frac{\pi(2r_{tube}^2 r_{ads}^2 - r_{ads}^4)}{8\mu}\frac{dP}{dL} + C_{sv}\frac{dP}{dL}\pi(r_{ads}^2) + \frac{\rho_{ads}}{\rho_{bulk}} C_{sv}\frac{dP}{dL}\pi(r_{tube}^2 - r_{ads}^2) \tag{46}$$

Q_{total} is the total volumetric flow of two-phase fluid, with respect to bulk density.

To obtain the dimensionless transport enhancement ratio with respect to the classical laminar volumetric flow through a tube, the Q_{total} above can be divided by the Hagen-Poiseuille equation for volumetric flow:

$$Q_{HP} = \frac{\pi(r_{tube}^4)}{8\mu}\frac{dP}{dL} \tag{47}$$

This relationship, while being represented by volumetric flow, is actually a mass transfer increase; the reason this is allowed is because both Q's are determined with respect to the classical bulk density, while the density of adsorbed phase has been preserved in the form of density ratio. From the simulation results, it could be concluded that the adsorbed phase density, once the adsorption layer is fully-developed, will become independent of pressure.

In equation 21, we have defined dimensionless mass transport enhancement ratio, R_{me}, as the ratio between actual mass transfer and classical Darcy-regime transfer for simulation data. Its equation form, ratio between the enhanced mass transport and classical Hagen-Poiseuille flow, can be developed as:

$$R_{me} = \frac{M_{total}}{M_{HP}} = \frac{\rho_{bulk}Q_{total}}{\rho_{bulk}Q_{HP}} = \frac{Q_{total}}{Q_{HP}} \tag{48}$$

$$R_{me} = \frac{\frac{\pi(2r_{tube}^2 r_{ads}^2 - r_{ads}^4)}{8\mu}\frac{dP}{dL} + C_{sv}\frac{dP}{dL}\pi(r_{ads}^2) + \frac{\rho_{ads}}{\rho_{bulk}}C_{sv}\frac{dP}{dL}\pi(r_{tube}^2 - r_{ads}^2)}{\frac{\pi(r_{tube}^4)}{8\mu}\frac{dP}{dL}} \tag{49}$$

$$R_{me} = \frac{Q_{total}}{Q_{HP}} = \frac{(2r_{tube}^2 r_{ads}^2 - r_{ads}^4)}{r_{tube}^4} + 8\mu C_{sv}(\frac{r_{ads}^2}{r_{tube}^4}) + 8\mu\frac{\rho_{ads}}{\rho_{bulk}}C_{sv}(\frac{r_{tube}^2 - r_{ads}^2}{r_{tube}^4}) \tag{50}$$

$$R_{me} = \frac{Q_{total}}{Q_{HP}} = \frac{(2r_{tube}^2 r_{ads}^2 - r_{ads}^4)}{r_{tube}^4} + 8\mu C_{sv}\left[\frac{r_{ads}^2}{r_{tube}^4} + \frac{\rho_{ads}}{\rho_{bulk}}\frac{r_{tube}^2 - r_{ads}^2}{r_{tube}^4}\right] \tag{51}$$

We can then segregate the enhancement factor into two terms, where:

$$R_{me} = R_{me-bulk} + R_{me-s} \tag{52}$$

The first term is $R_{me-bulk}$.

$$R_{me-bulk} = \frac{(2r_{tube}^2 r_{ads}^2 - r_{ads}^4)}{r_{tube}^4} \tag{53}$$

This represents the conventional Hagen-Poiseuille transport in the bulk phase with adjusted transport surface area due to layer(s) being taken up by adsorbed molecule. It is a function of pore radius and thickness of the adsorbed layer.

The second term is R_{me-s}.

$$R_{me-s} = 8\mu C_{sv}\left[\frac{r_{ads}^2}{r_{tube}^4} + \frac{\rho_{ads}}{\rho_{bulk}}\frac{r_{tube}^2 - r_{ads}^2}{r_{tube}^4}\right] \tag{54}$$

This term represent transport of the adsorbed phase and the velocity enhancement of the bulk phase that becomes prominent at small pore size. It is a function of pore radius, thickness of adsorbed layer, and pressure and temperature (which determines the viscosity and densities).

The contribution of each term can be demonstrated by segregating the portions of the velocity profile as shown in Figure 6.a.1 and 6.a.2 below, with transport in the adsorbed layer (areas to the left and right of $R_{me-bulk}$) also enhanced by greater adsorbed phase density.

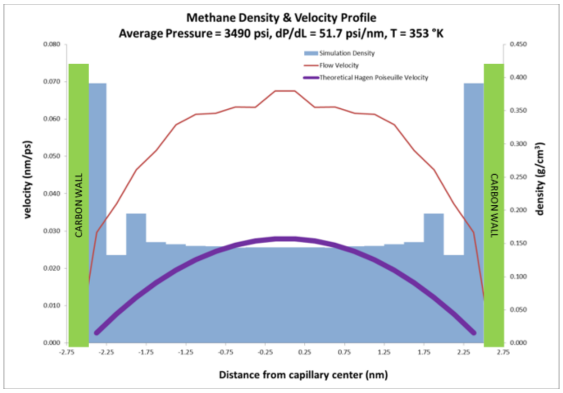

Figure 6.a .1: Velocity profile compared with classical Hagen-Poiseuille Velocity at equivalent conditions (Original Figure, Riewchotisakul, 2015).

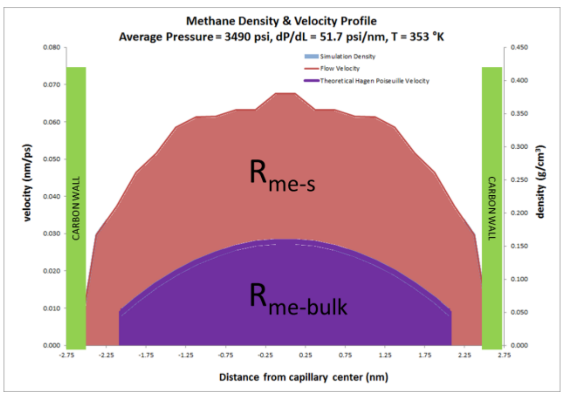

Figure 6.a.2: Velocity profile segregated into regions contributed by the two enhancement terms (Original Figure, Riewchotisakul, 2015).

We can also infer from the equations that as the tube radius gets larger, r_{ads} approaches r_{tube} and the mass transfer increase simply approaches to R_{me} =1; in other words, the effects will be dampened in large capillaries where adsorbed phase contribution becomes minimal when compared with the bulk phase's.

As shown in the equation above, the enhancement ratio R_{me} depends heavily on the pore radius. It was observed in Figure 6.b, R_{me} plotted against pore diameter, that the majority of enhancement occurs below 15 nm-diameter pores and the effects rapidly diminish at larger pore size. Comparison between R_{me} derived from equation 51 and R_{me} obtained from simulation data of 5 nm tube using equation 21 are also shown in the plot. With a slight degree of variation, possibly due to regression fit of C_{sv} values, there is a good match of data surrounding the 5-nm point.

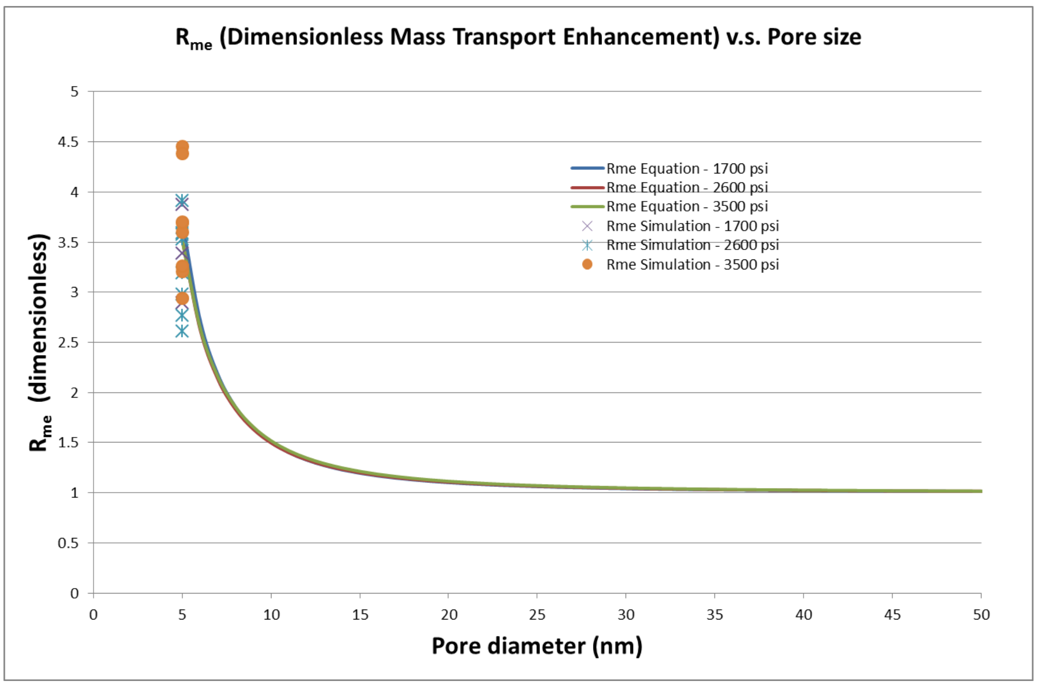

Figure 6.b: Prediction of R_{me} relationship with pore size (Original Figure, Riewchotisakul, 2015). Comparison is against simulation calculated values. Enhancement effects are significant below pore diameter of 10 nm. Variation of viscosity with respect to average pressure has negligible impact.

While the enhancement effect theoretically increases with smaller pore size, it is speculated that there is a minimum-pore diameter limit on such phenomena. When the capillary become too narrow and the walls are too close to each other, storage and flow of multiphase hydrocarbon will be very restricted. From the simulation results, it can be infer that such size limit is below 5 nm capillaries.

6.2 Application to Permeability and Field Example

Since derivation of Darcy's permeability from Hagen-Poiseuille flow is simply an addition of flow through *n* independent number of tubes, this dimensionless factor can apply to the permeability as well. However, actual kerogen contains multiple pore size, which means the enhancement, a function or r_{tube}, should be weighed against the pore size distribution.

Assuming a collection of independent organic tubes of the different sizes, we define the pore size distribution as:

$$\sum f(r_{tube}) = 1 \tag{55}$$

The above fraction f is the distribution function for tube with radius r_{tube}, weighed by pore volume fraction. It can be obtained from pore size distribution experiments of various organic-rich shales.

The enhanced permeability or organic pores can then be estimated:

$$k_a = k \sum [f(r_{tube})\ R_{me}] \tag{56}$$

$$k_a = k \sum [f(r_{tube})\ (R_{me-bulk} + R_{me-s})] \tag{57}$$

$$k_a = k \sum [f(r_{tube}) * \left(\frac{\left(2r_{tube}^2 r_{ads}^2 - r_{ads}^4\right)}{r_{tube}^4} + 8\mu C_{sv}\left[\frac{r_{ads}^2}{r_{tube}^4} + \frac{\rho_{ads}}{\rho_{bulk}}\frac{r_{tube}^2 - r_{ads}^2}{r_{tube}^4}\right]\right)] \tag{58}$$

The above is an adjustment for mass transfer due to adsorbed phase transport. The difference between the enhancement above and slippage is that while slippage is a low-pressure laboratory phenomena, decreasing with pressure, the adsorbed phase transport develops with the presence of an adsorption layer, and tends to increase with pressure. Our simulations show that consideration of the latter transport mechanism as part of the recovery from source rocks rich in organic pores and capillaries is more reasonable.

Pore size distribution measurements from a Marcellus shale sample are shown below (Figure 6.c); it is observed that significant volume fraction, over one-third, lies in the region below 15 nm diameter. The weighed dimensionless mass transport enhancement function from equation 58 is applied to this data with cut-off at 2 nm, i.e. assuming no flow from pores smaller than 2 nm. This results in additional permeability enhancement of **57.3%**, a significant increase. This factor can then be used to correct permeability from organic pores for application in flow simulations and production forecast.

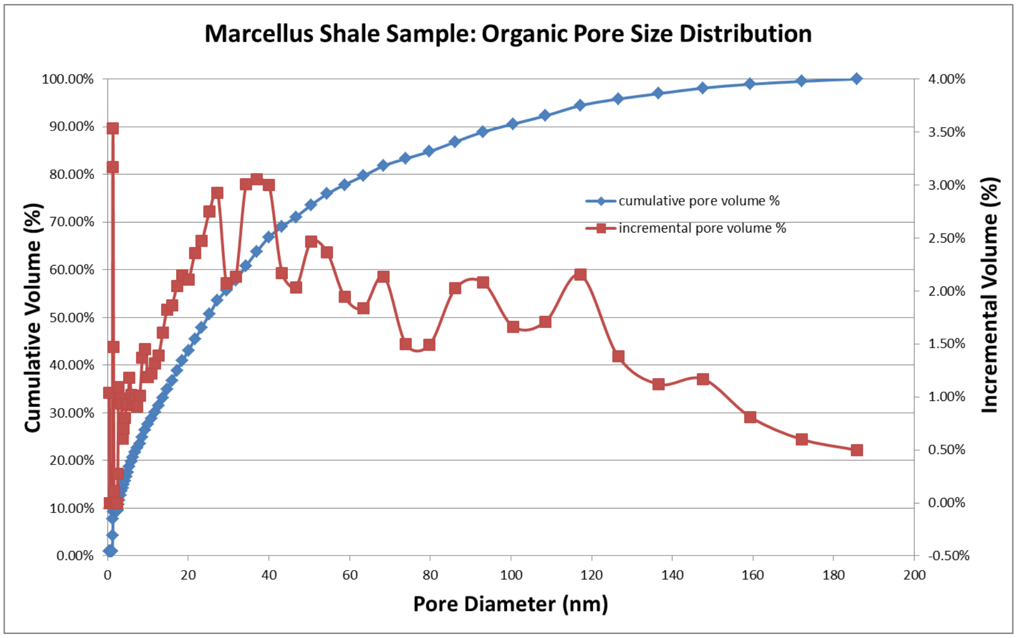

Figure 6.c: Pore size distribution of a Marcellus shale sample (Original Figure, Riewchotisakul, 2015). Over one-third of the pore volumes belong to those smaller than 15 nm.

7 CONCLUSION

A piston-model is developed using non-equilibrium molecular dynamics simulations and have been performed to analyze the effect of adsorbed phase on transport in nanometer-scale organic pores and to compare with the mechanistic flow equation derived from the literature.

Many profound discoveries were obtained from the simulation results. First, the adsorbed hydrocarbon layers are found to be mobile, with comparable velocity to the bulk phase, when subjected to pressure gradient across the nanotube. The velocity of the adsorbed layer are also discovered to be strongly, linearly dependent on pressure gradient. Second, the bulk phase transport is enhanced by the mobility of the adsorbed phase, leading to overall mass transport enhancement. These effects are found to be more prominent at higher pressure and larger pressure gradient.

The results from simulations have led to the development of dimensionless mass transport enhancement equation as a function of pore size, designed to accommodate the effects of mobile adsorption layer. The effects are predicted to be significant at 10 nanometer sized pore and below, converging to classical Darcy flow in larger size pores. Application to a shale sample pore distribution data from the field yields significant result, leading to a correction factor for permeability of organic pores.

Further development of the concepts and equations can be done readily with proposed piston-frame model. Mass transport enhancement and C_{sv} sensitivity to pore size can be investigated by varying the pore diameter. The effects of compositional hydrocarbon in the pore can be introduced by adding heavier molecules such as propane or butane into the simulation. Heavier molecules are predicted to significantly increase the adsorbed phase density due to their greater attraction to the wall; however, the attraction will most likely result in less mobility and lower C_{sv} value. Effects of tortuosity factor can also be introduced into the simulation by varying tube structure. Greater tortuosity is expected to hinder the transport enhancement and adsorbed phase mobility, but not the for bulk phase.

The proposed dimensionless equation and simulation result should serve as a basis for better understanding and flow predictions of transport in nanometer-scale kerogen pores found in many organic-rich shales and coals.

REFERENCES

Ambrose, R. J., Hartman, R. C., Akkutlu, I. Y. 2011. Shale Gas-in-Place Calculations Part II: Multi-Component Gas Adsorption Effects. Paper SPE 144097 presented at SPE Unconventional Gas Conference, Woodlands, Texas, 14-16 June

Ambrose, R. J., Hartman, R. C., Diaz-Campos, M. et al. 2010. Shale Gas-in-Place Calculations Part I: New Pore-Scale Considerations. Paper SPE 131772 presented at SPE Unconventional Gas Conference, Pittsburgh, Pennsylvania, 23-25 February.

Choi, J. G., D. D. Do, H. D. Do. 2001. Surface Diffusion of Adsorbed Molecules in Porous Media: Monolayer, Multilayer, and Capillary Condensation Regimes. Industrial & Engineering Chemistry Research 40 (19): 4005-4031.

Duong, D. Do. 1998. Adsorption Analysis : Equilibria and Kinetics. London: Series in Chemical Engineering, Imperial College Press (Reprint).

Energy Information Administration. Top 100 U.S. Oil & Gas Fields By 2009 Proved Reserves. United States Energy Information Administration Report, EIA, 2009.

Fathi E., and Akkutlu, I.Y. 2012. Mass Transport of Adsorbed-phase in Stochastic Porous Medium with Fluctuating Porosity Field and Nonlinear Gas Adsorption Kinetics. Journal of Transport in Porous Media, Volume 91 (1) 5-33.

Fathi E., A. Tinni, I. Y. Akkutlu. 2012. Correction to Klinkenberg Slip Theory for Gas Flow in Nano-capillaries. International Journal of Coal Geology, 103: 51-59.

Higashi, Kunio, Akio Oya, Jun Oishi. 1966. Surface Diffusion Phenomena in Gaseous Diffusion, (III) (in Journal of Nuclear Science and Technology 3 (2): 51-56.

Klinkenberg, L. J. 1941. The Permeability of Porous Media to Liquids And Gases. Proc.

Medved, I., R. Cerny. 2011. Surface Diffusion in Porous Media: A Critical Review. Microporous and Mesoporous Materials 142 (2-3): 405-422.

Rahmani Didar, Behnaz, Akkutlu, I. Y. 2013. Pore-size Dependence of Fluid Phase Behavior and Properties in Organic-Rich Shale Reservoirs. Paper 164099 presented at SPE International Symposium on Oilfield Chemistry, Woodlands, Texas, 8-10 April

Yang, R. T., J. B. Fenn, G. L. Haller. 1973. Modification to Higashi Model for Surface Diffusion (in English). AIChE Journal 19 (5): 1052-1053.

APPENDIX A

Velocity Profiles

Velocity profiles obtained from simulations are shown below in red. For comparison, classical laminar flow Hagen-Poiseuille velocity profiles (HP velocity) are shown in purple, with phase density in blue. Average Pressure, Pressure Gradient, and temperature of each simulation are labeled on the plots. Enhancement of transport is observed in the simulations. All figures below are original, Riewchotisakul, 2015.

A.1 Average Pressure of 1700 psi

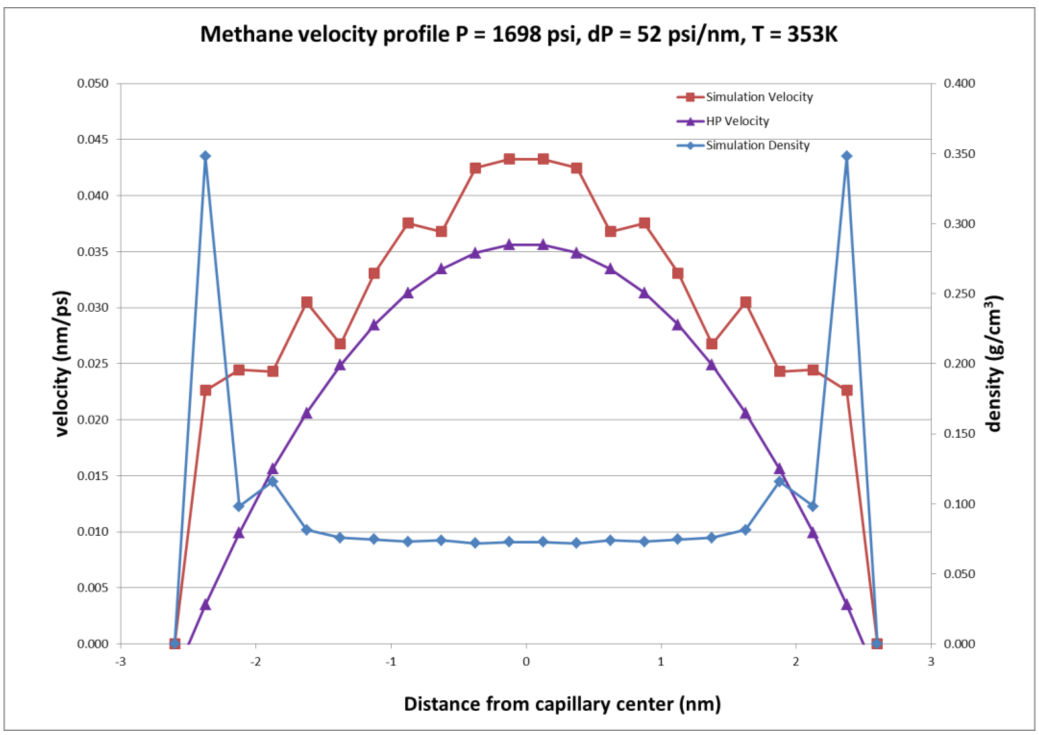

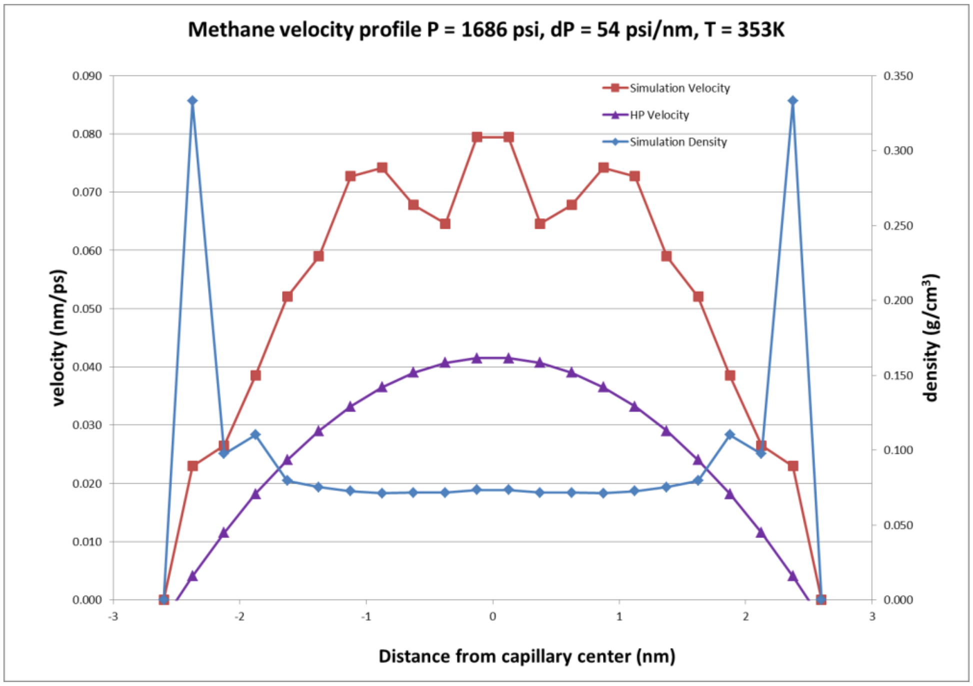
Methane velocity profile P = 1686 psi, dP = 54 psi/nm, T = 353K
Simulation Velocity
HP Velocity
Simulation Density
velocity (nm/ps)
density (g/cm3)
Distance from capillary center (nm)

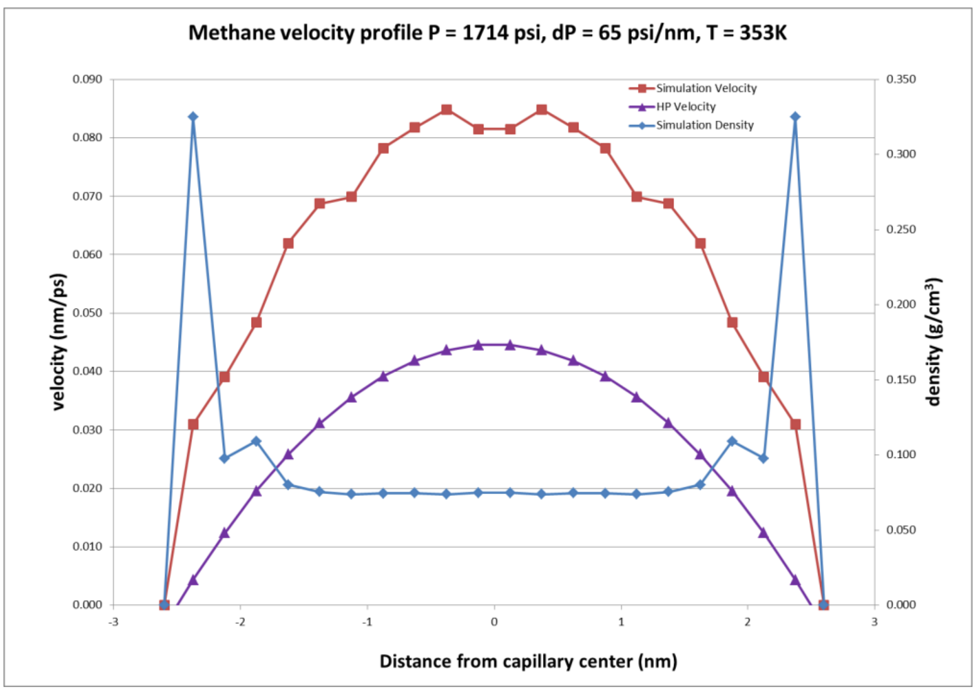
Methane velocity profile P = 1714 psi, dP = 65 psi/nm, T = 353K
Simulation Velocity
HP Velocity
Simulation Density
velocity (nm/ps)
density (g/cm3)
Distance from capillary center (nm)

A.2 Average Pressure of 2600 psi

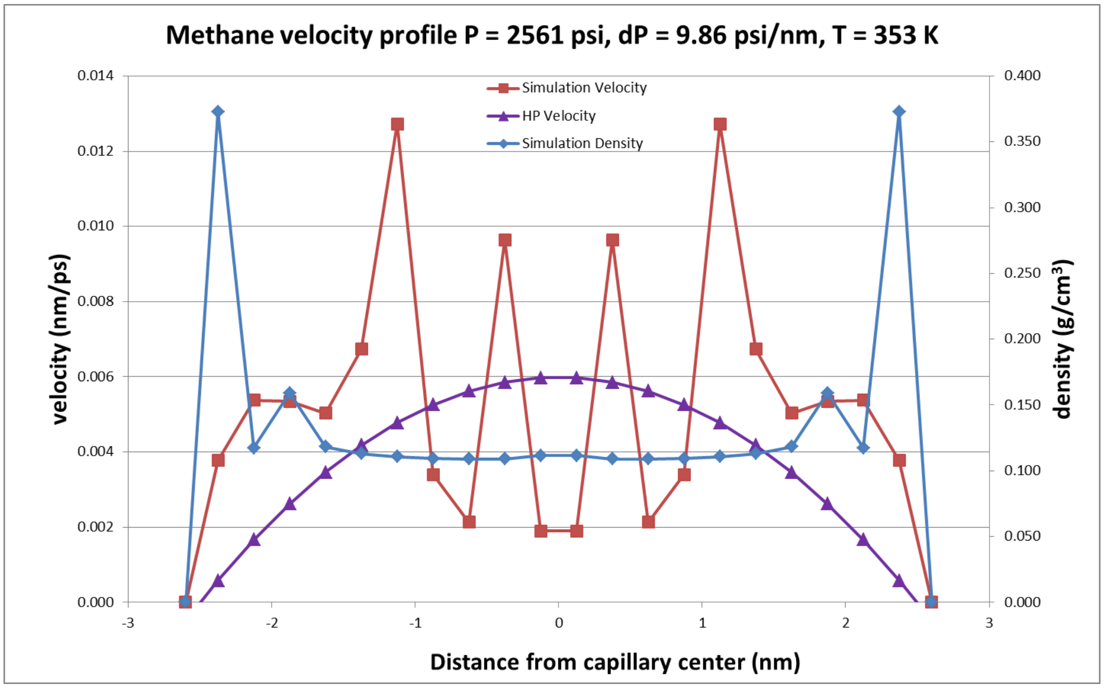

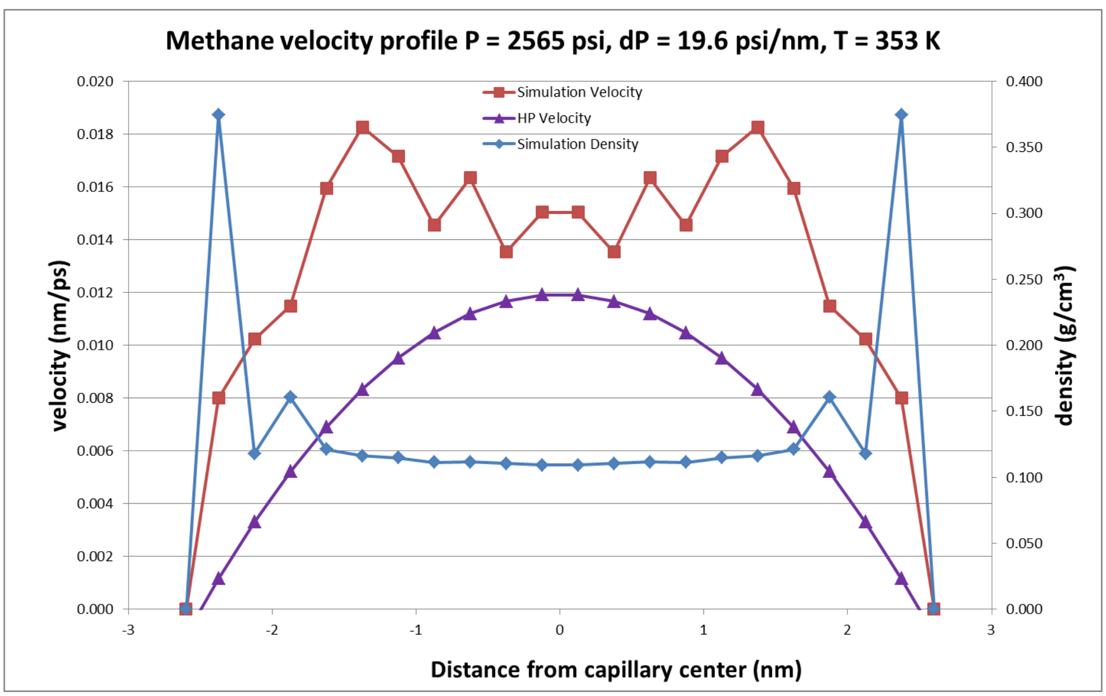

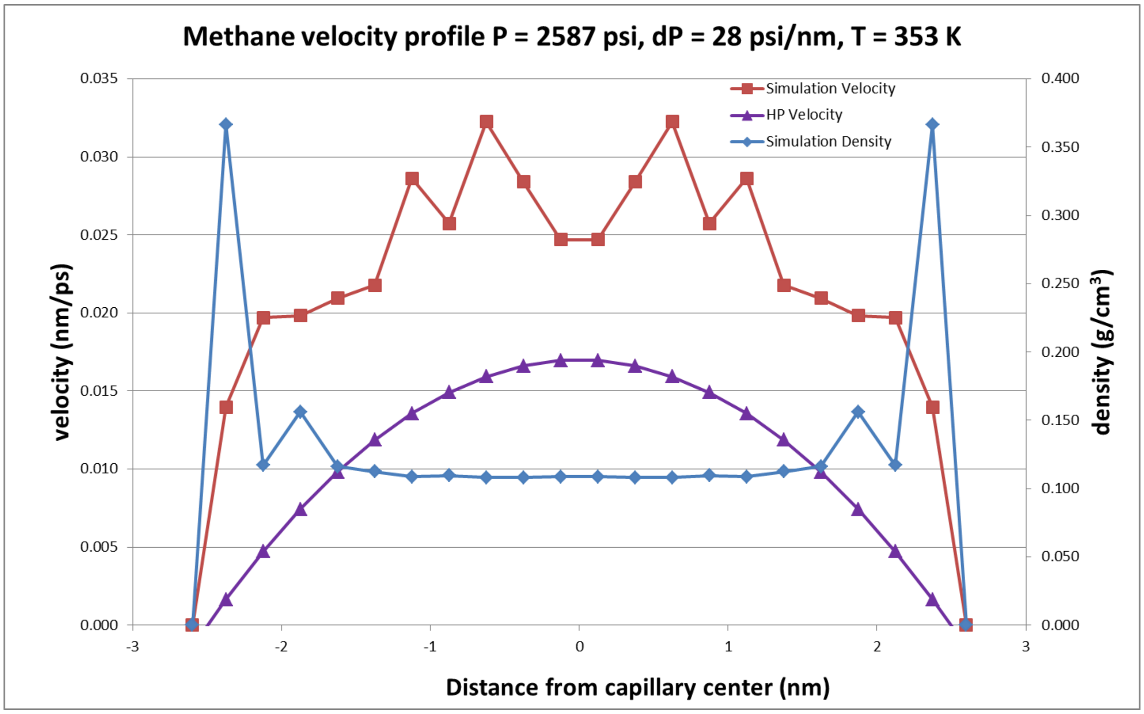
Methane velocity profile P = 2587 psi, dP = 28 psi/nm, T = 353 K
Simulation Velocity
HP Velocity
Simulation Density
velocity (nm/ps)
density (g/cm³)
0.035
0.030
0.025
0.020
0.015
0.010
0.005
0.000
0.400
0.350
0.300
0.250
0.200
0.150
0.100
0.050
0.000
-3
-2
-1
0
1
2
3
Distance from capillary center (nm)

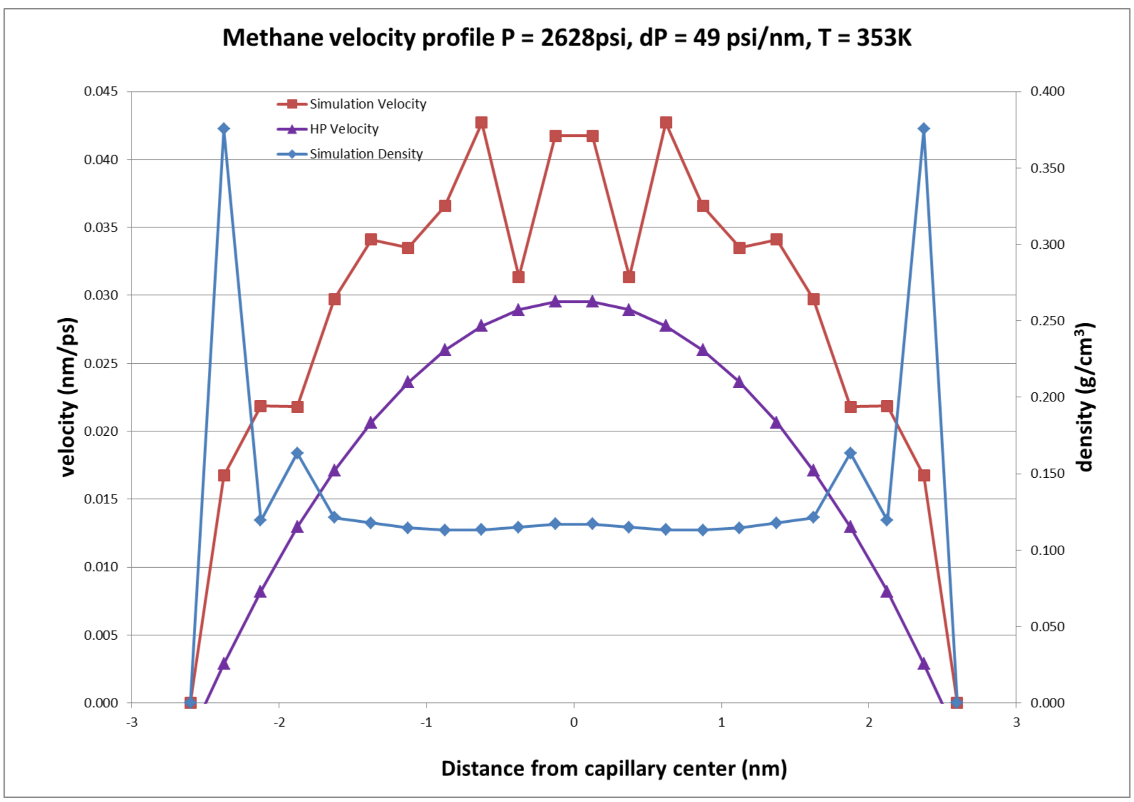
Methane velocity profile P = 2628psi, dP = 49 psi/nm, T = 353K
Simulation Velocity
HP Velocity
Simulation Density
velocity (nm/ps)
density (g/cm³)
0.045
0.040
0.035
0.030
0.025
0.020
0.015
0.010
0.005
0.000
0.400
0.350
0.300
0.250
0.200
0.150
0.100
0.050
0.000
-3
-2
-1
0
1
2
3
Distance from capillary center (nm)

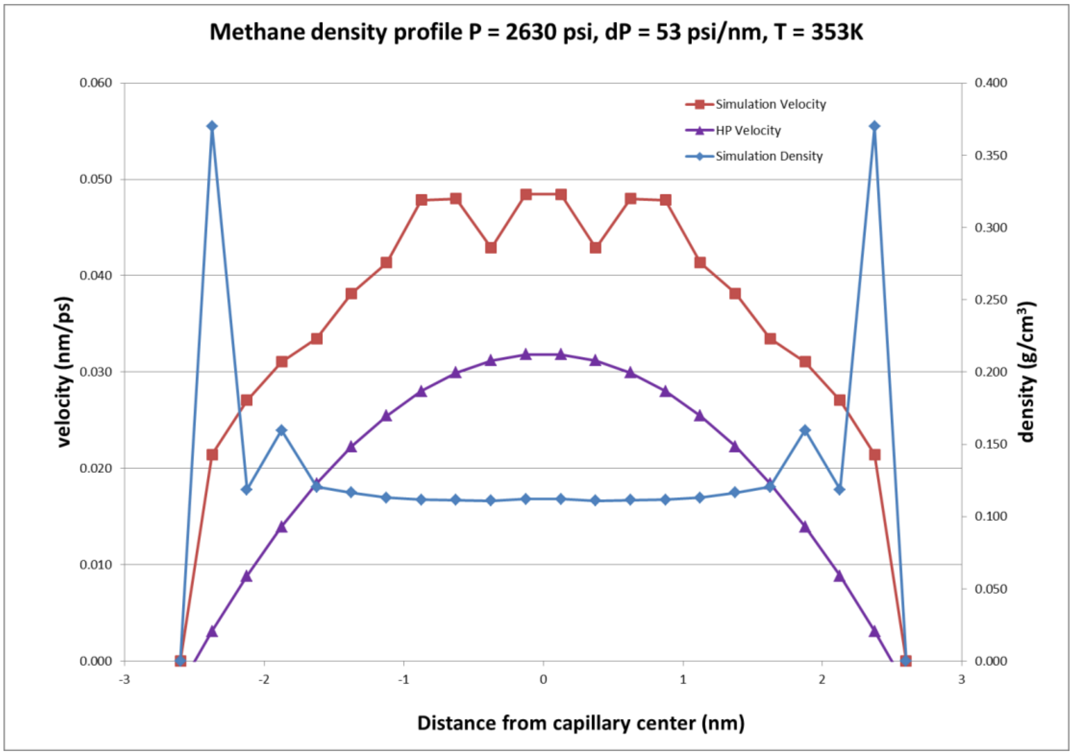

Methane density profile P = 2630 psi, dP = 53 psi/nm, T = 353K
Simulation Velocity
HP Velocity
Simulation Density
velocity (nm/ps)
density (g/cm³)
Distance from capillary center (nm)

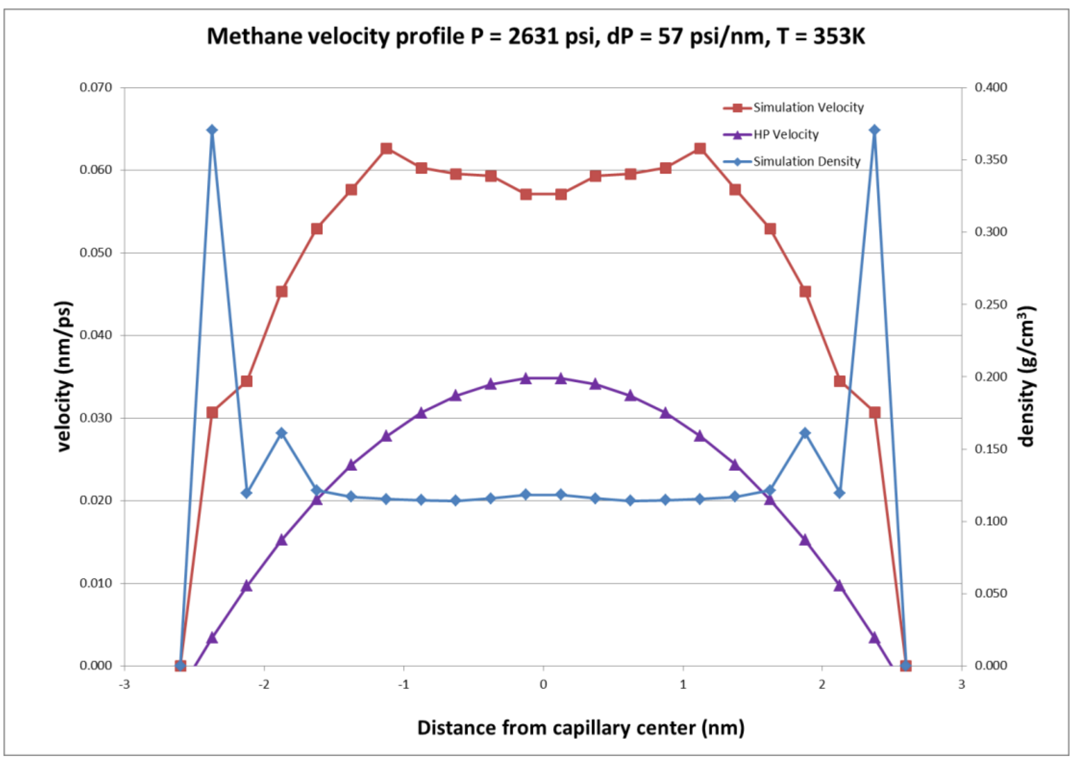

Methane velocity profile P = 2631 psi, dP = 57 psi/nm, T = 353K
Simulation Velocity
HP Velocity
Simulation Density
velocity (nm/ps)
density (g/cm³)
Distance from capillary center (nm)

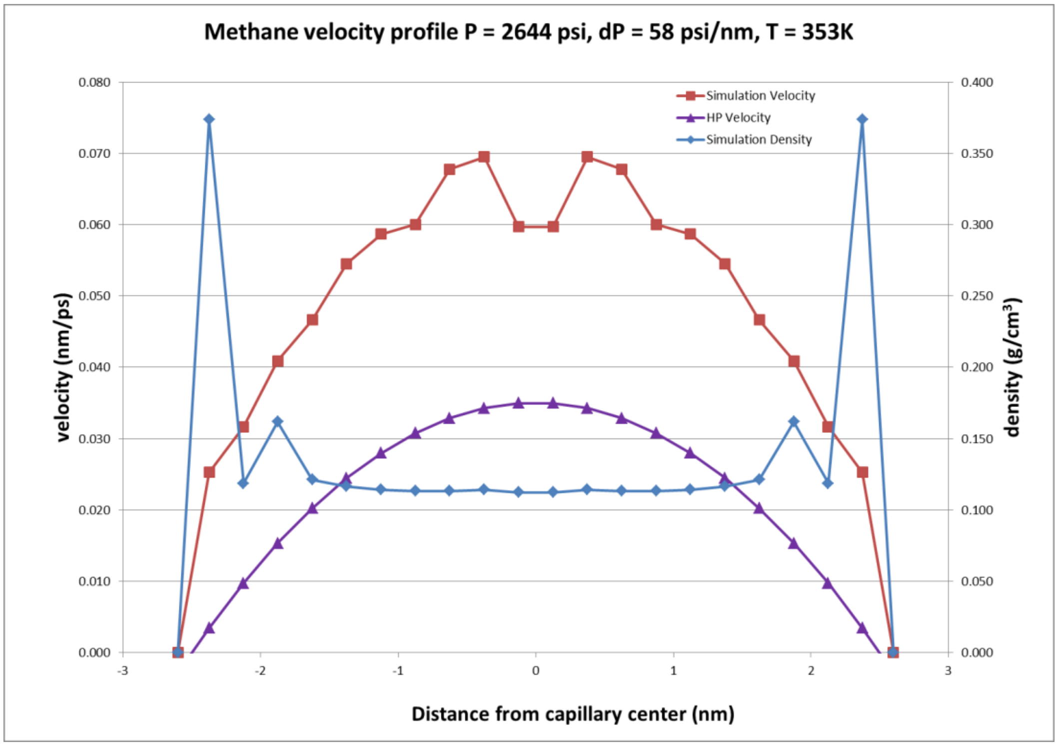

Methane velocity profile P = 2644 psi, dP = 58 psi/nm, T = 353K
Simulation Velocity
HP Velocity
Simulation Density
velocity (nm/ps)
density (g/cm³)
0.000
0.010
0.020
0.030
0.040
0.050
0.060
0.070
0.080
0.000
0.050
0.100
0.150
0.200
0.250
0.300
0.350
0.400
-3
-2
-1
0
1
2
3
Distance from capillary center (nm)

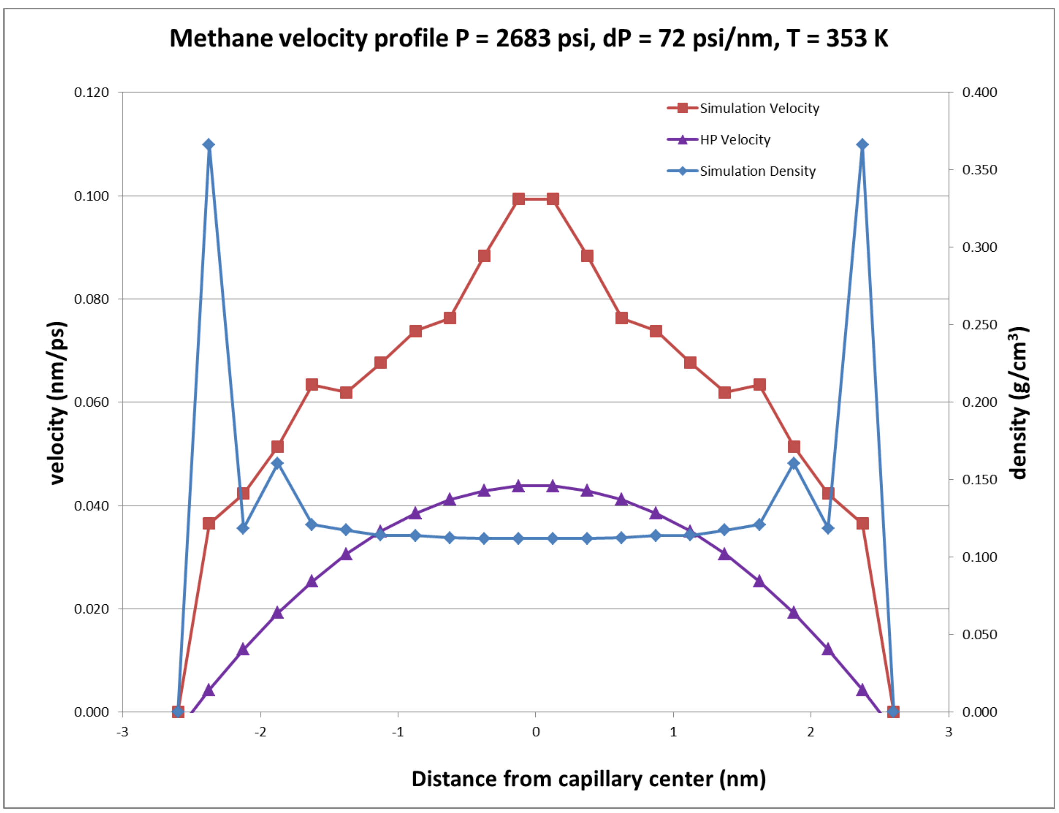

Methane velocity profile P = 2683 psi, dP = 72 psi/nm, T = 353 K
Simulation Velocity
HP Velocity
Simulation Density
velocity (nm/ps)
density (g/cm³)
0.000
0.020
0.040
0.060
0.080
0.100
0.120
0.000
0.050
0.100
0.150
0.200
0.250
0.300
0.350
0.400
-3
-2
-1
0
1
2
3
Distance from capillary center (nm)

A.3 Average Pressure of 3500 psi

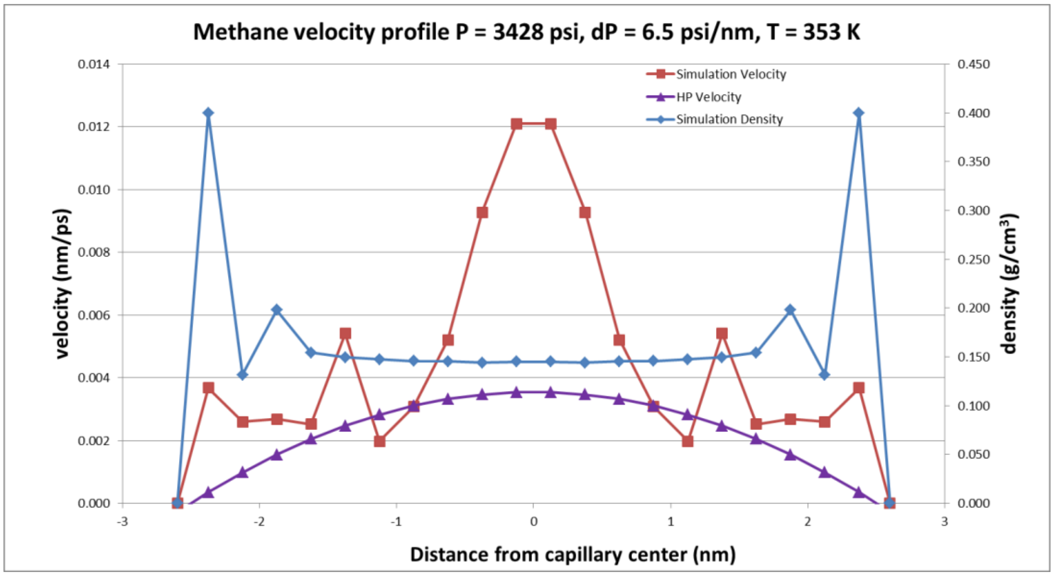

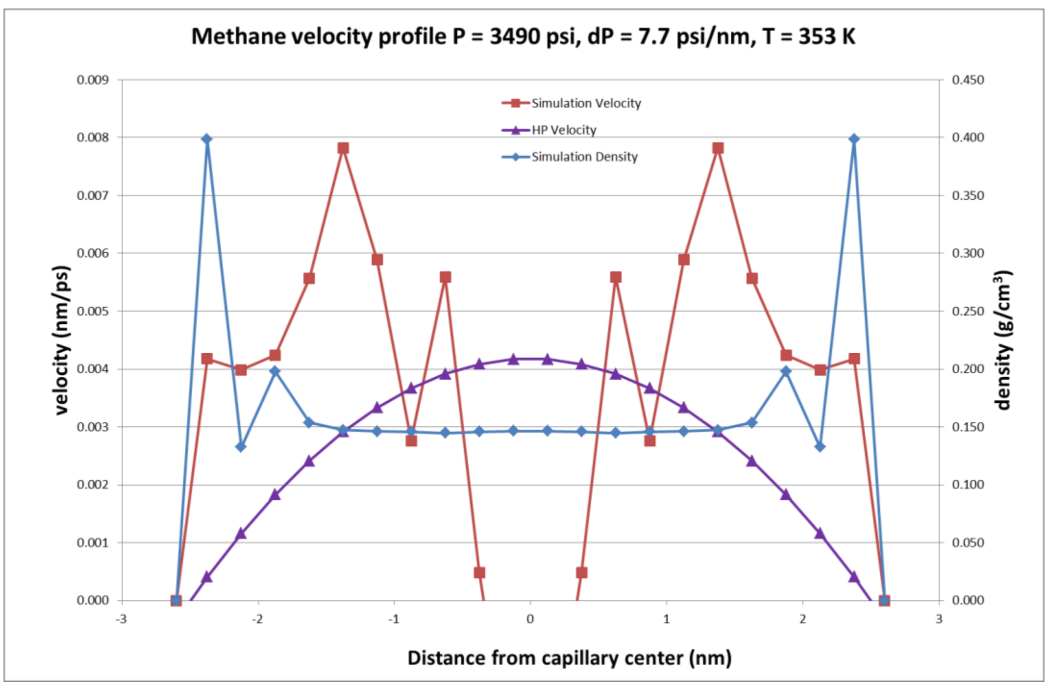

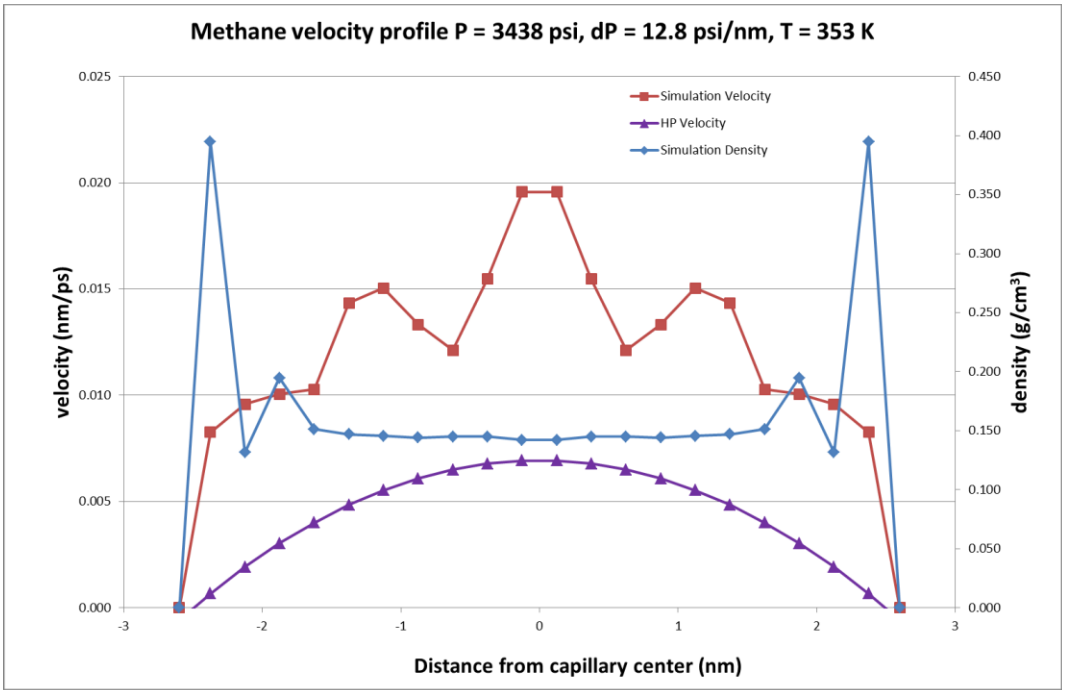
Methane velocity profile P = 3438 psi, dP = 12.8 psi/nm, T = 353 K
Simulation Velocity
HP Velocity
Simulation Density
velocity (nm/ps)
density (g/cm³)
Distance from capillary center (nm)
0.025
0.020
0.015
0.010
0.005
0.000
0.450
0.400
0.350
0.300
0.250
0.200
0.150
0.100
0.050
0.000
-3
-2
-1
0
1
2
3

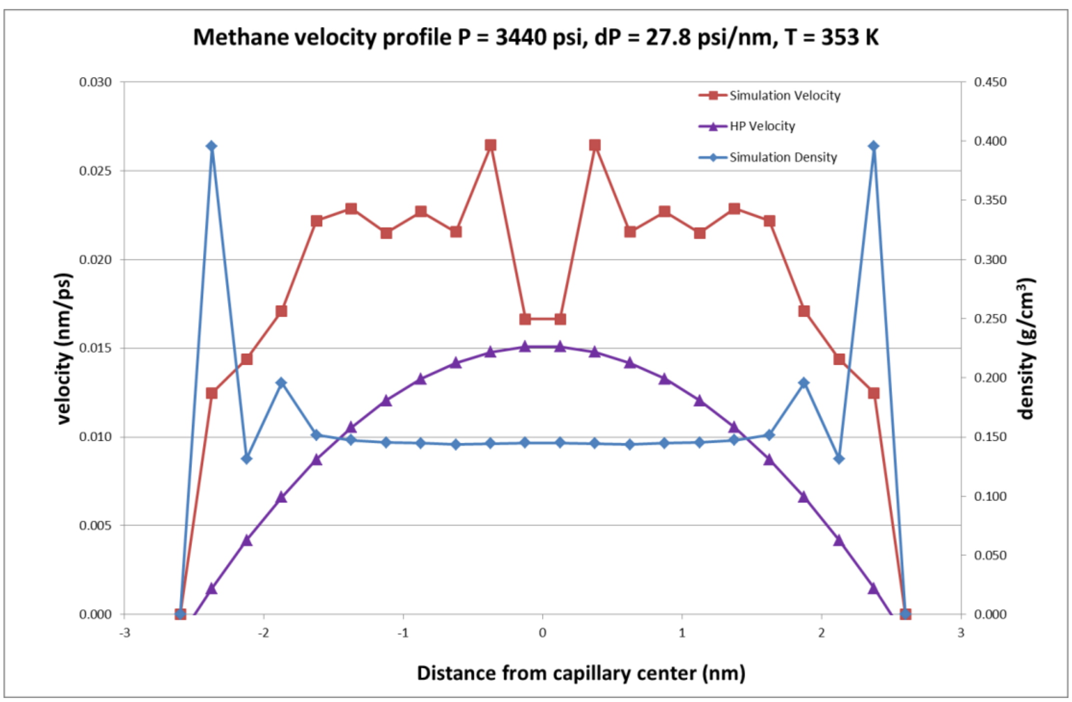
Methane velocity profile P = 3440 psi, dP = 27.8 psi/nm, T = 353 K
Simulation Velocity
HP Velocity
Simulation Density
velocity (nm/ps)
density (g/cm³)
Distance from capillary center (nm)
0.030
0.025
0.020
0.015
0.010
0.005
0.000
0.450
0.400
0.350
0.300
0.250
0.200
0.150
0.100
0.050
0.000
-3
-2
-1
0
1
2
3

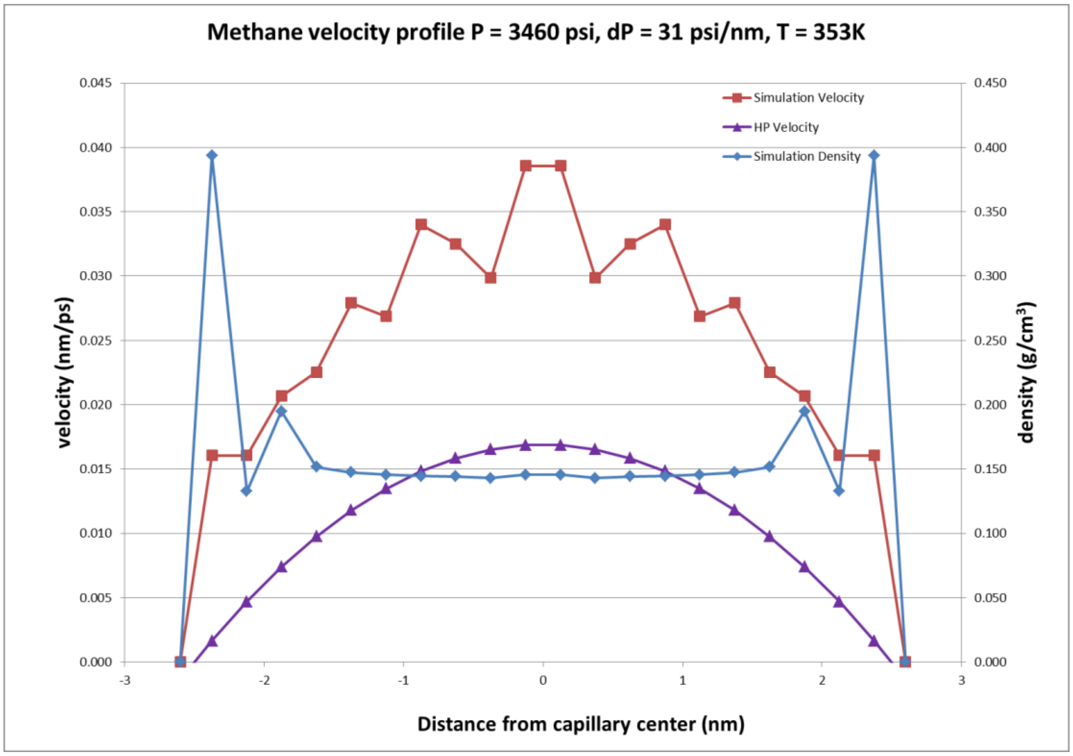

Methane velocity profile P = 3460 psi, dP = 31 psi/nm, T = 353K
Simulation Velocity
HP Velocity
Simulation Density
velocity (nm/ps)
density (g/cm³)
Distance from capillary center (nm)

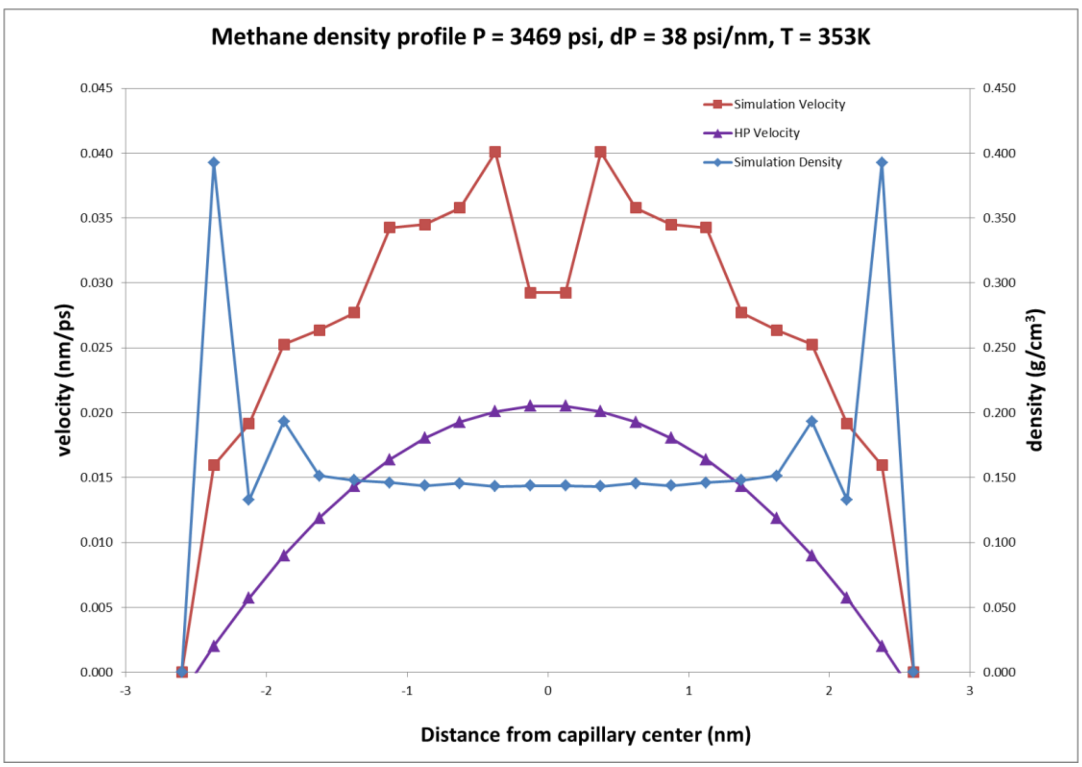

Methane density profile P = 3469 psi, dP = 38 psi/nm, T = 353K
Simulation Velocity
HP Velocity
Simulation Density
velocity (nm/ps)
density (g/cm³)
Distance from capillary center (nm)

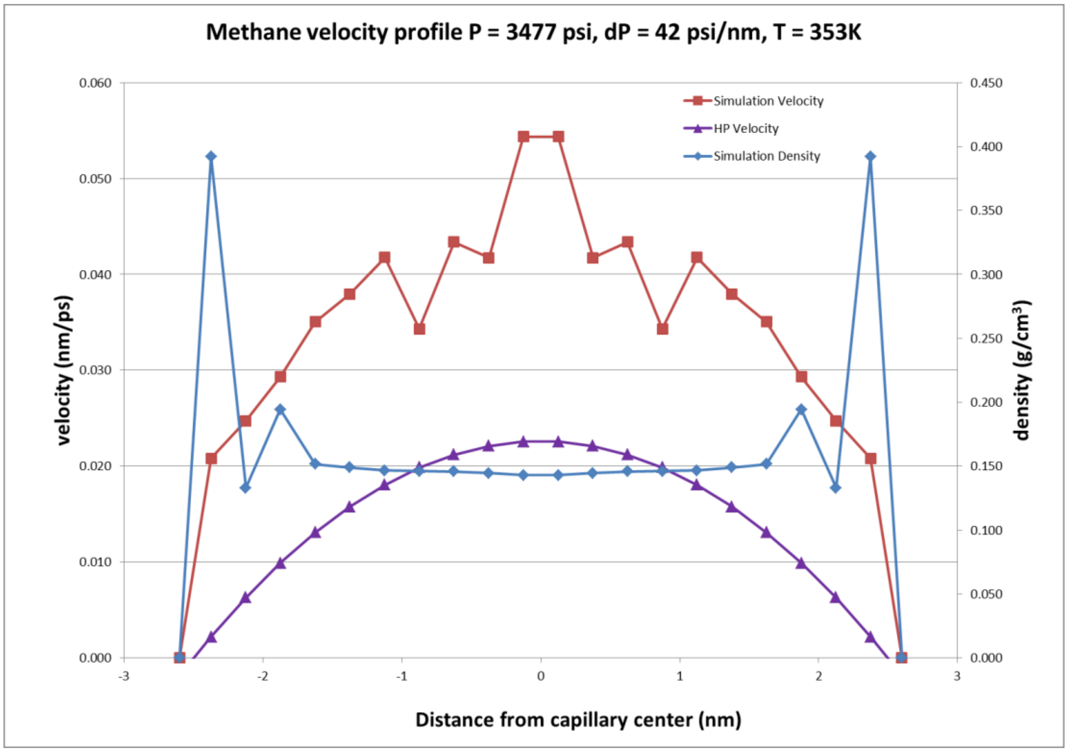
Methane velocity profile P = 3477 psi, dP = 42 psi/nm, T = 353K
Simulation Velocity
HP Velocity
Simulation Density
velocity (nm/ps)
density (g/cm³)
Distance from capillary center (nm)

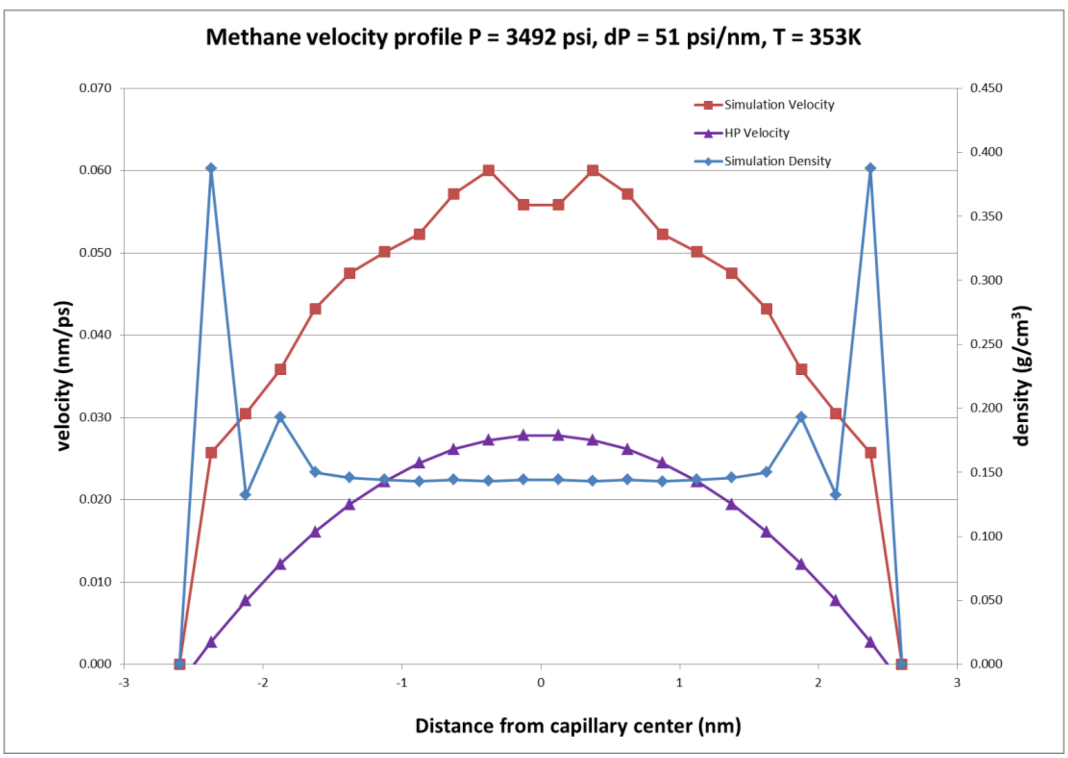
Methane velocity profile P = 3492 psi, dP = 51 psi/nm, T = 353K
Simulation Velocity
HP Velocity
Simulation Density
velocity (nm/ps)
density (g/cm³)
Distance from capillary center (nm)

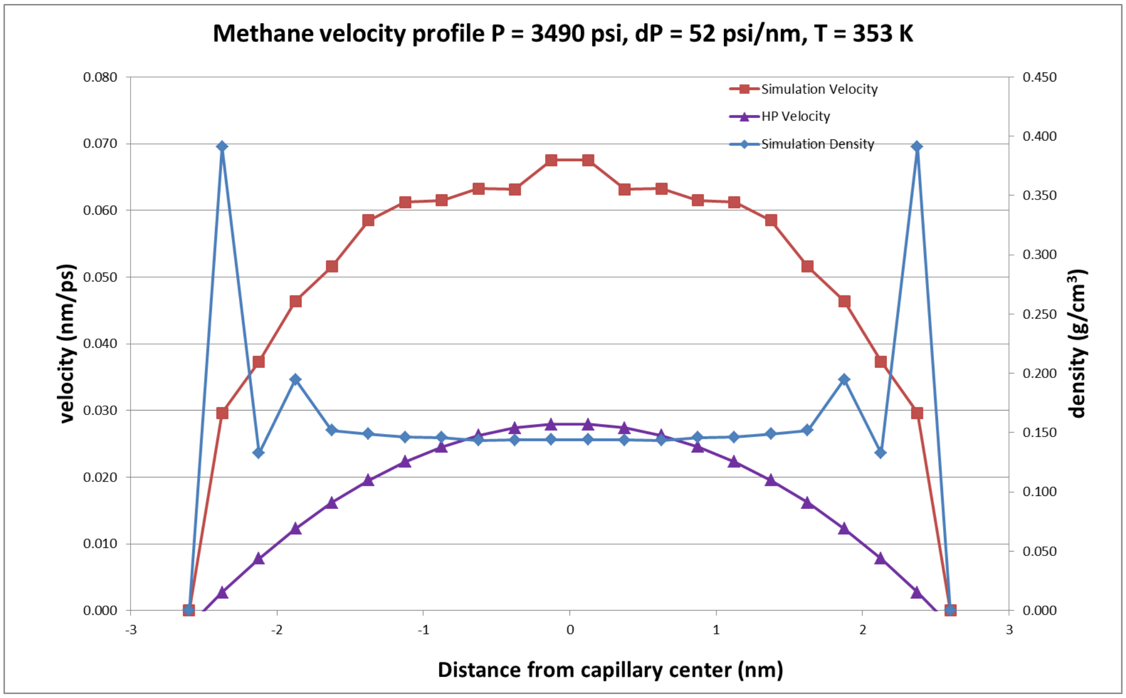

Methane velocity profile P = 3490 psi, dP = 52 psi/nm, T = 353 K
Simulation Velocity
HP Velocity
Simulation Density
velocity (nm/ps)
density (g/cm³)
Distance from capillary center (nm)
0.080
0.070
0.060
0.050
0.040
0.030
0.020
0.010
0.000
0.450
0.400
0.350
0.300
0.250
0.200
0.150
0.100
0.050
0.000
-3
-2
-1
0
1
2
3

APPENDIX B

Superpositioned Velocity Profiles

Velocity profiles obtained from simulations are shown below in red. For comparison, adsorbed phase velocity are added to classical laminar flow Hagen-Poiseuille velocity profiles (HP velocity), shown in green. Phase density is shown in blue. Average Pressure, Pressure Gradient, and temperature of each simulation are labeled on the plots. For most of the result, very close matches are found between the simulation velocity and the superpositioned HP velocity. All figures below are original, Riewchotisakul, 2015.

B.1 Average Pressure of 1700 psi

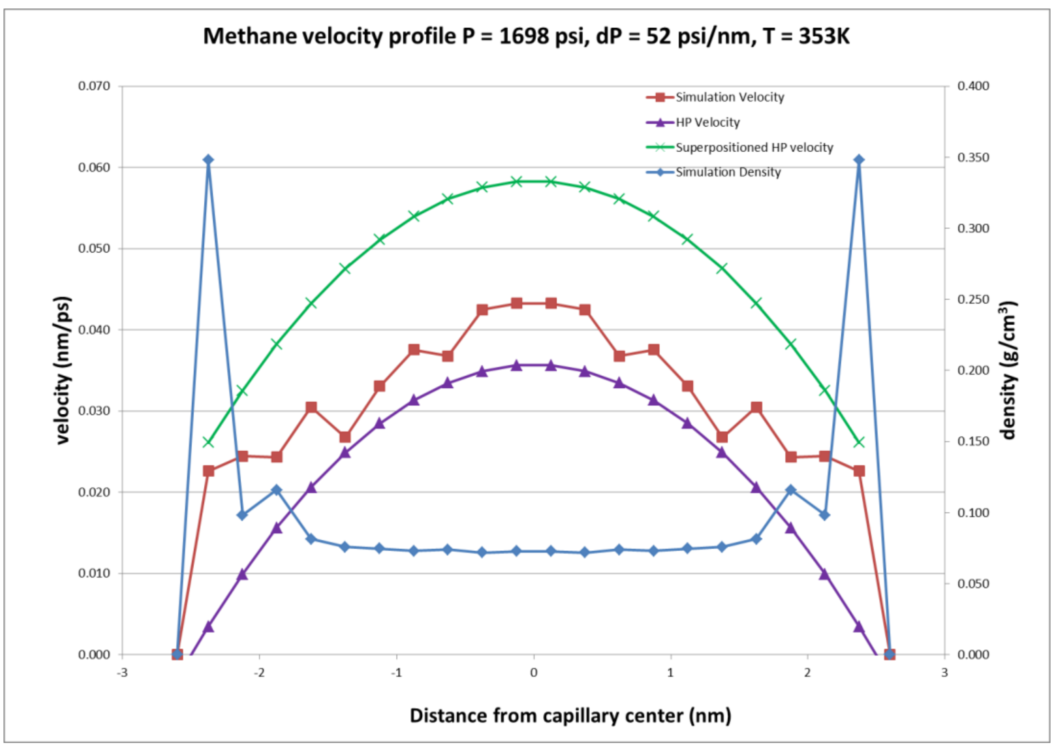

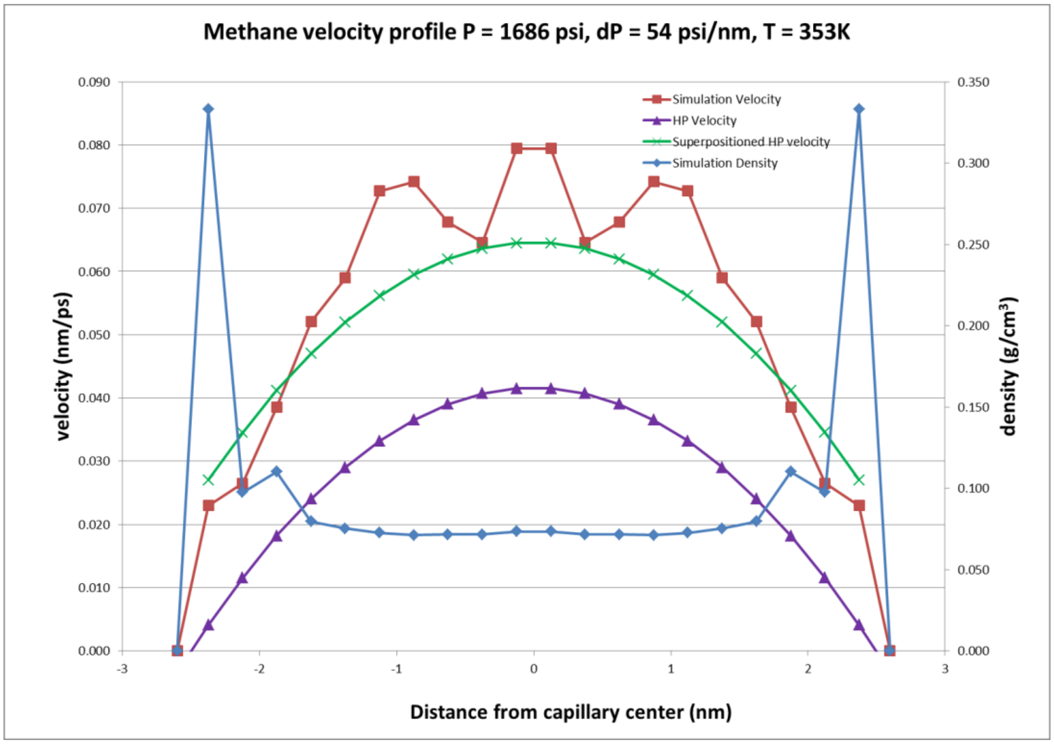
Methane velocity profile P = 1686 psi, dP = 54 psi/nm, T = 353K
Simulation Velocity
HP Velocity
Superpositioned HP velocity
Simulation Density
velocity (nm/ps)
density (g/cm^3)
Distance from capillary center (nm)
0.090
0.080
0.070
0.060
0.050
0.040
0.030
0.020
0.010
0.000
0.350
0.300
0.250
0.200
0.150
0.100
0.050
0.000
-3
-2
-1
0
1
2
3

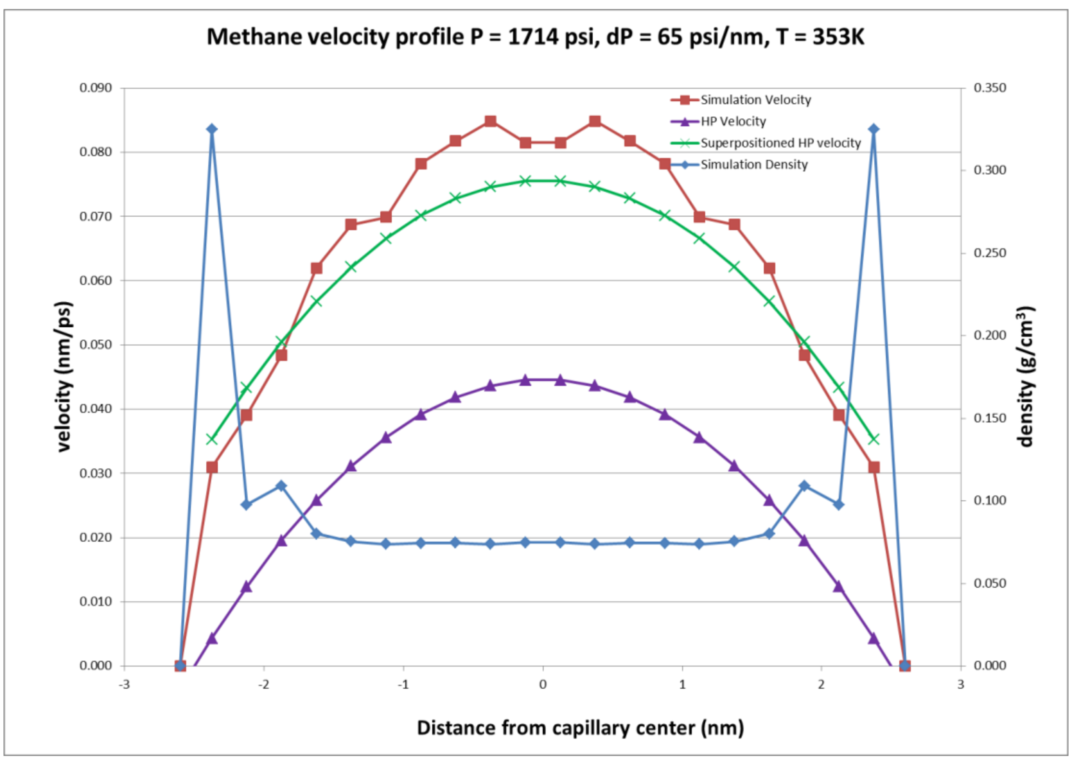
Methane velocity profile P = 1714 psi, dP = 65 psi/nm, T = 353K
Simulation Velocity
HP Velocity
Superpositioned HP velocity
Simulation Density
velocity (nm/ps)
density (g/cm^3)
Distance from capillary center (nm)
0.090
0.080
0.070
0.060
0.050
0.040
0.030
0.020
0.010
0.000
0.350
0.300
0.250
0.200
0.150
0.100
0.050
0.000
-3
-2
-1
0
1
2
3

B.2 Average Pressure of 2600 psi

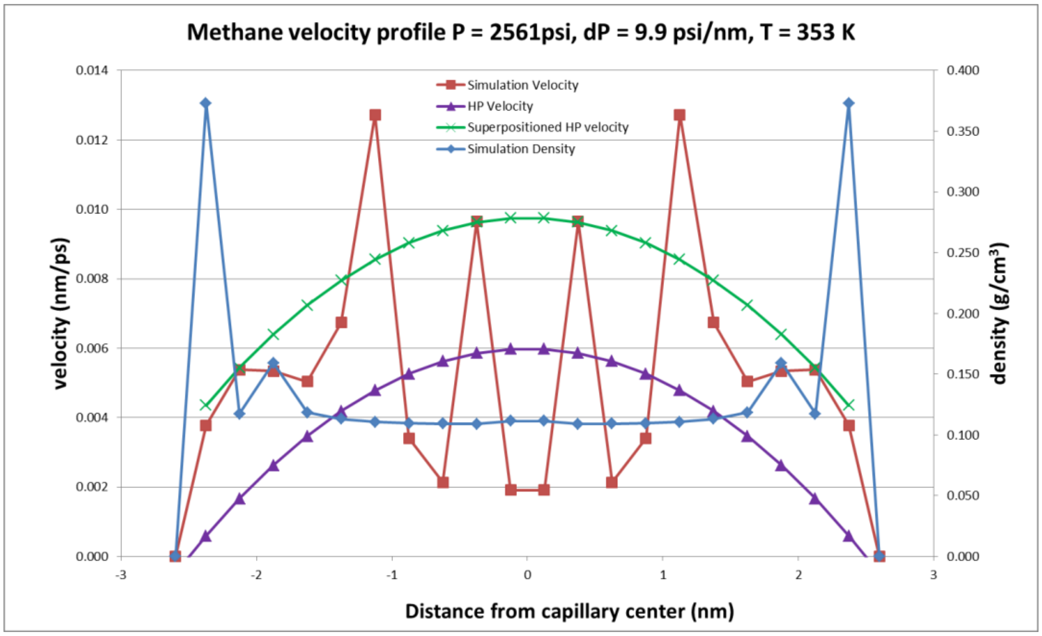

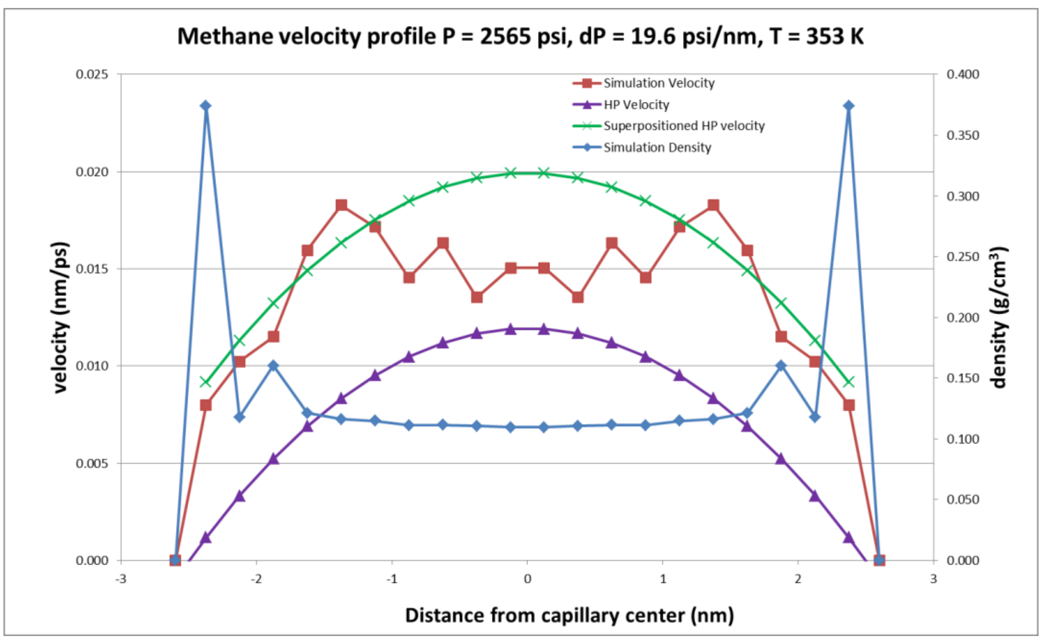

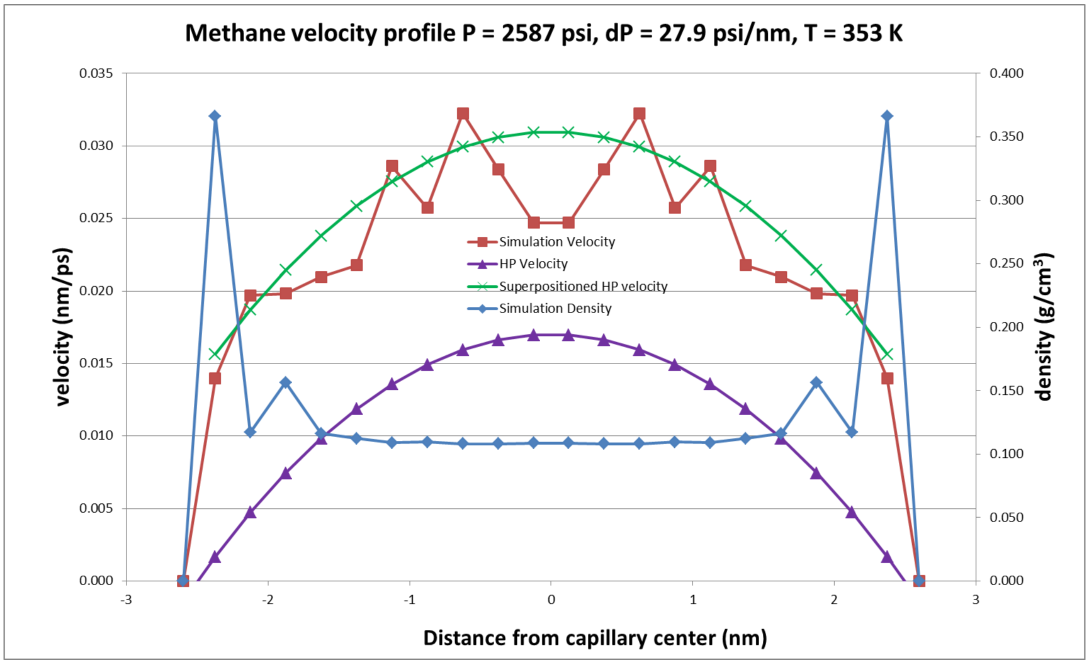
Methane velocity profile P = 2587 psi, dP = 27.9 psi/nm, T = 353 K
velocity (nm/ps)
density (g/cm³)
Distance from capillary center (nm)
Simulation Velocity
HP Velocity
Superpositioned HP velocity
Simulation Density

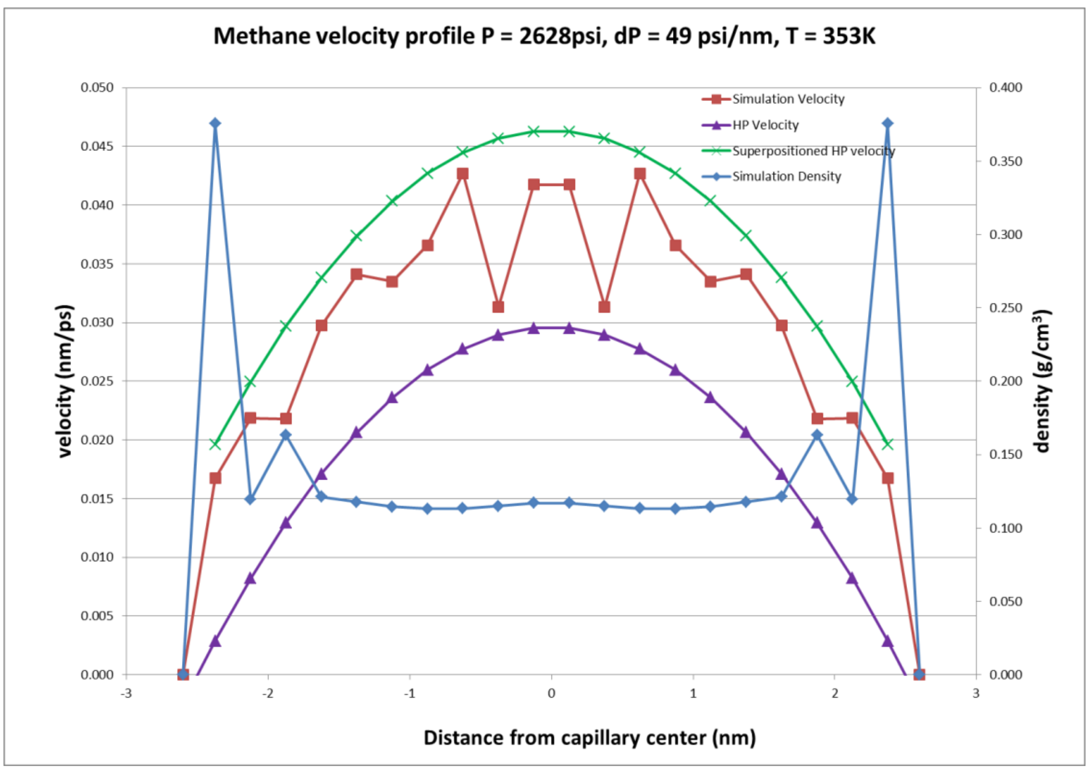
Methane velocity profile P = 2628psi, dP = 49 psi/nm, T = 353K
velocity (nm/ps)
density (g/cm³)
Distance from capillary center (nm)
Simulation Velocity
HP Velocity
Superpositioned HP velocity
Simulation Density

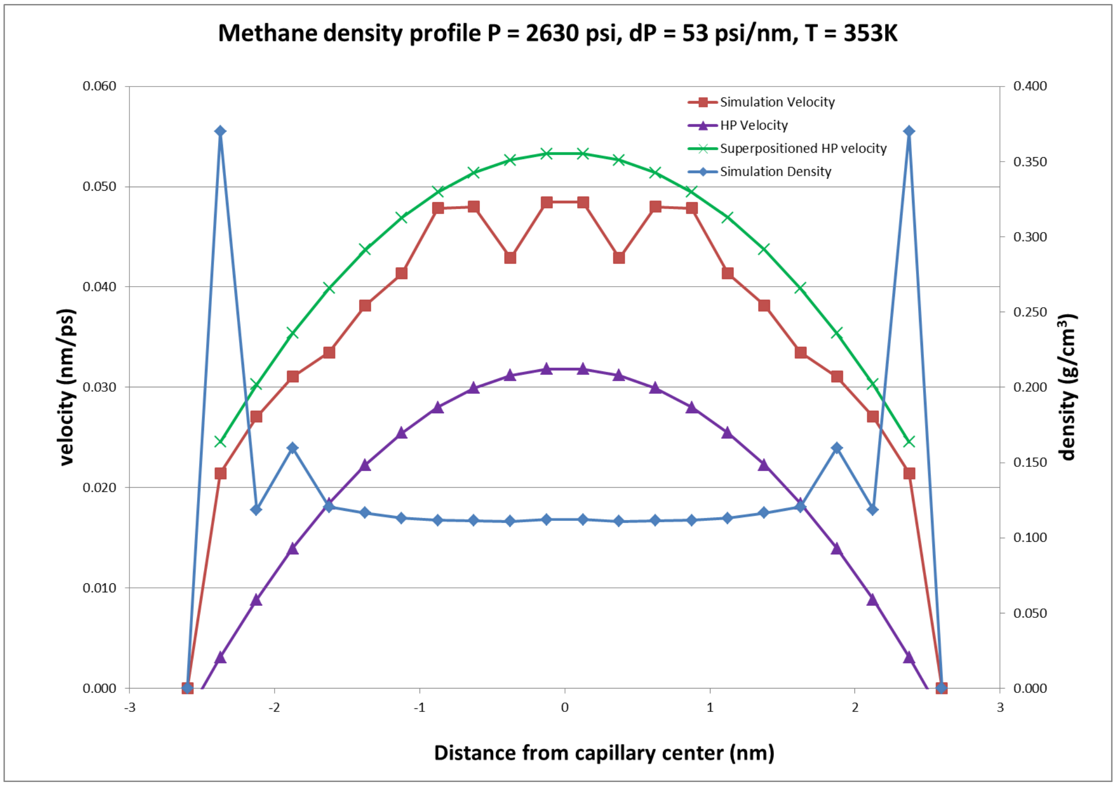

Methane density profile P = 2630 psi, dP = 53 psi/nm, T = 353K
Simulation Velocity
HP Velocity
Superpositioned HP velocity
Simulation Density
velocity (nm/ps)
density (g/cm³)
Distance from capillary center (nm)

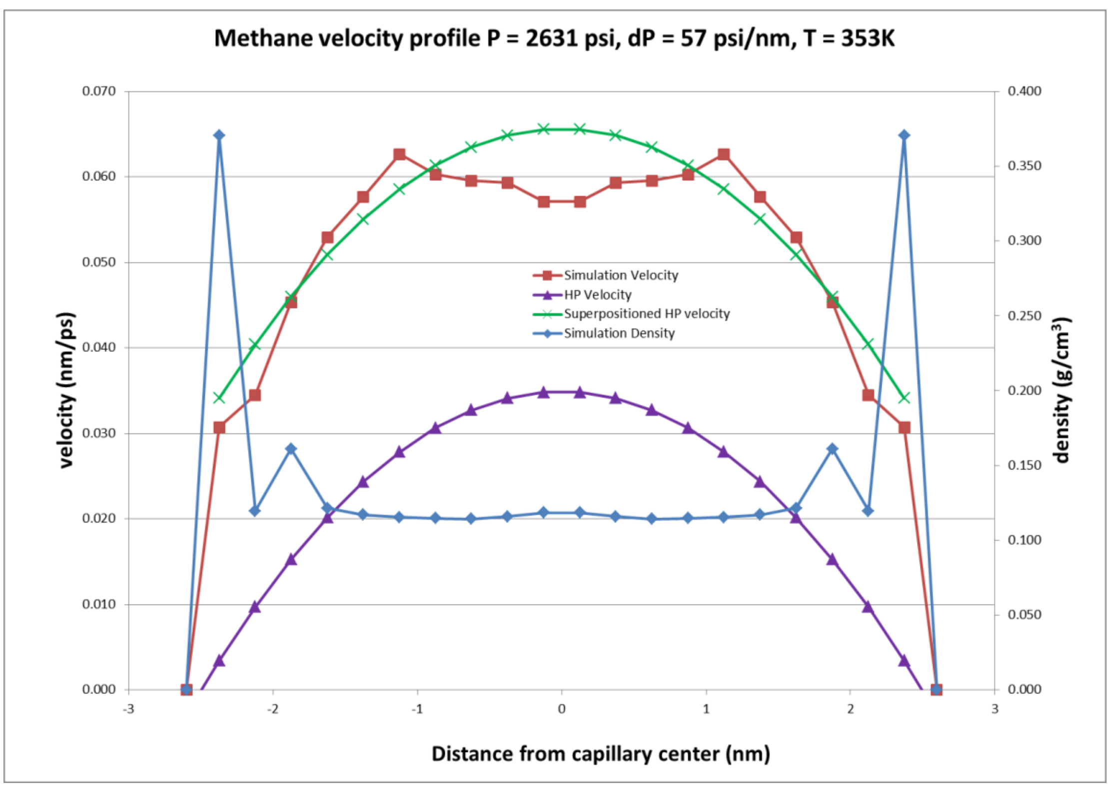

Methane velocity profile P = 2631 psi, dP = 57 psi/nm, T = 353K
Simulation Velocity
HP Velocity
Superpositioned HP velocity
Simulation Density
velocity (nm/ps)
density (g/cm³)
Distance from capillary center (nm)

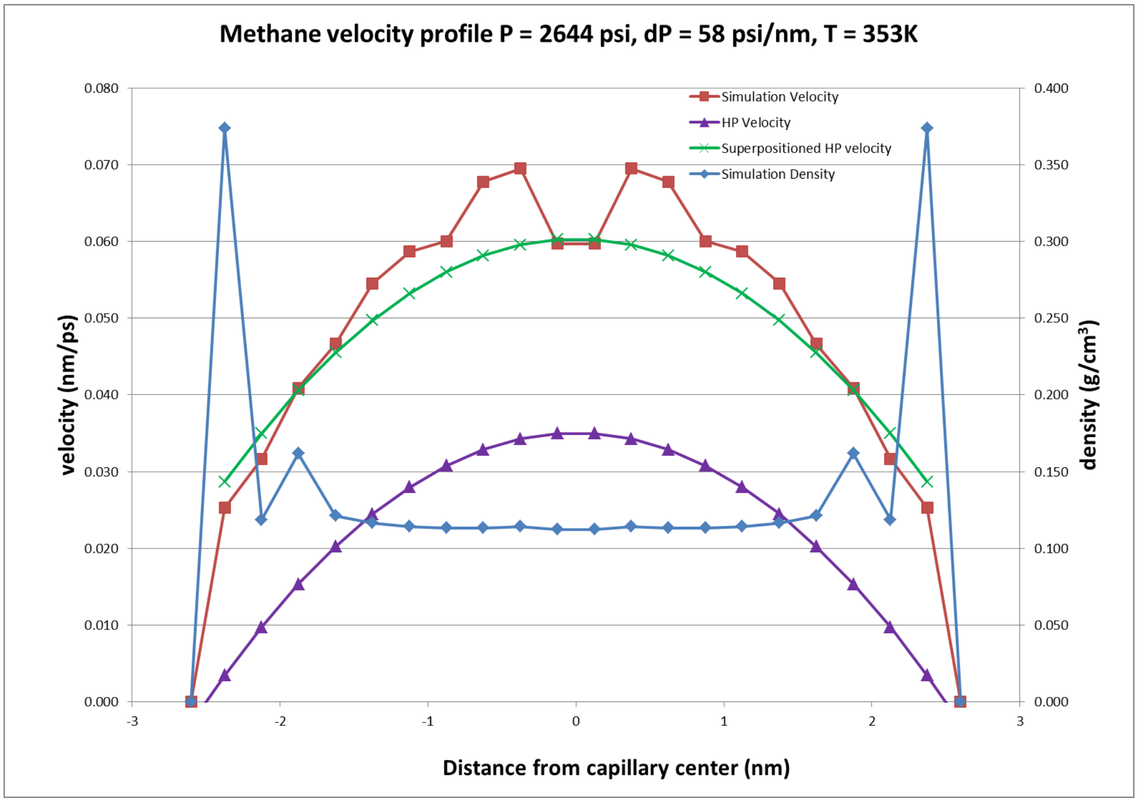
Methane velocity profile P = 2644 psi, dP = 58 psi/nm, T = 353K
Simulation Velocity
HP Velocity
Superpositioned HP velocity
Simulation Density
velocity (nm/ps)
density (g/cm³)
Distance from capillary center (nm)
0.080
0.070
0.060
0.050
0.040
0.030
0.020
0.010
0.000
0.400
0.350
0.300
0.250
0.200
0.150
0.100
0.050
0.000
-3
-2
-1
0
1
2
3

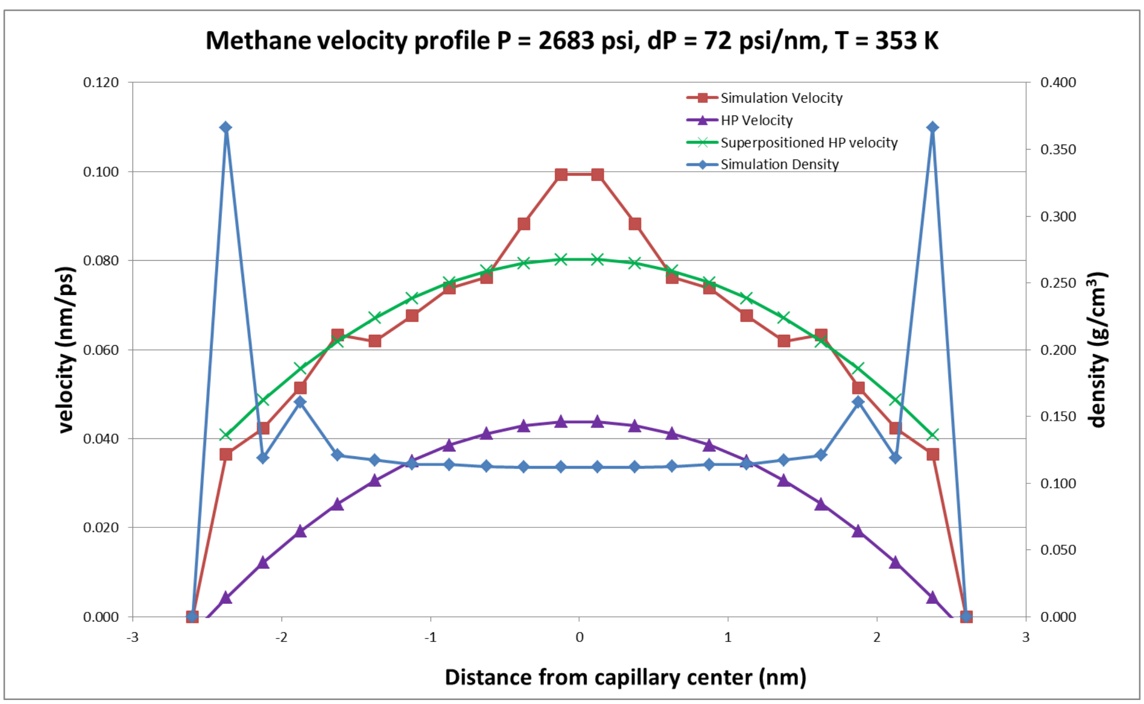
Methane velocity profile P = 2683 psi, dP = 72 psi/nm, T = 353 K
Simulation Velocity
HP Velocity
Superpositioned HP velocity
Simulation Density
velocity (nm/ps)
density (g/cm³)
Distance from capillary center (nm)
0.120
0.100
0.080
0.060
0.040
0.020
0.000
0.400
0.350
0.300
0.250
0.200
0.150
0.100
0.050
0.000
-3
-2
-1
0
1
2
3

B.3 Average Pressure of 3500 psi

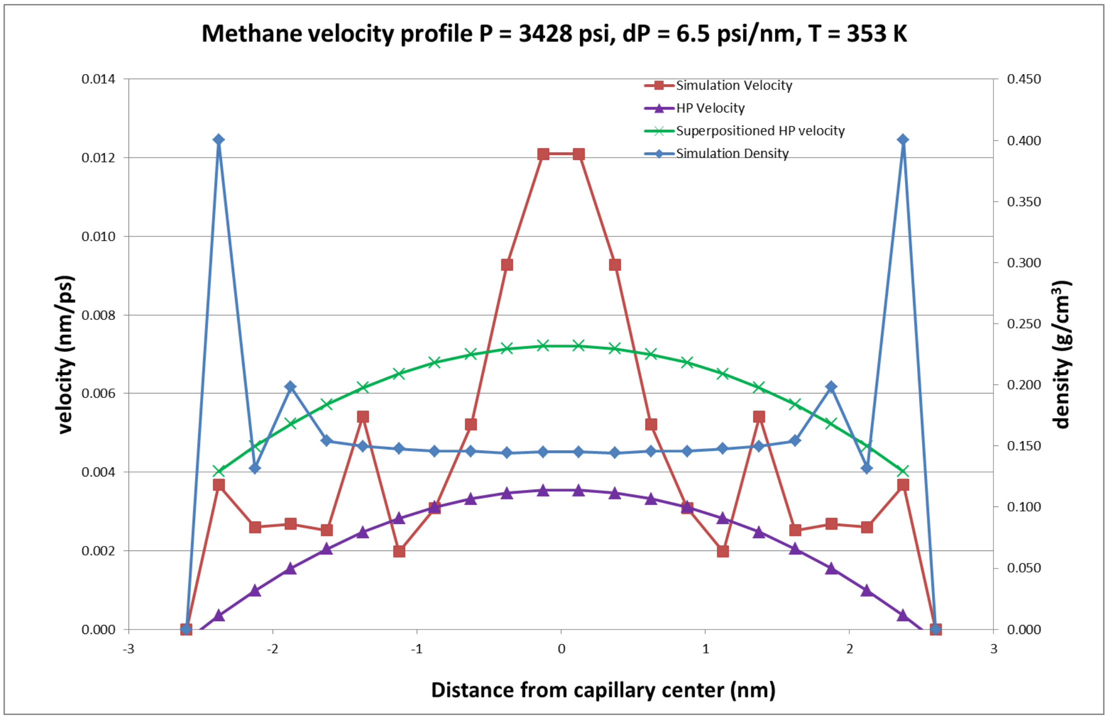

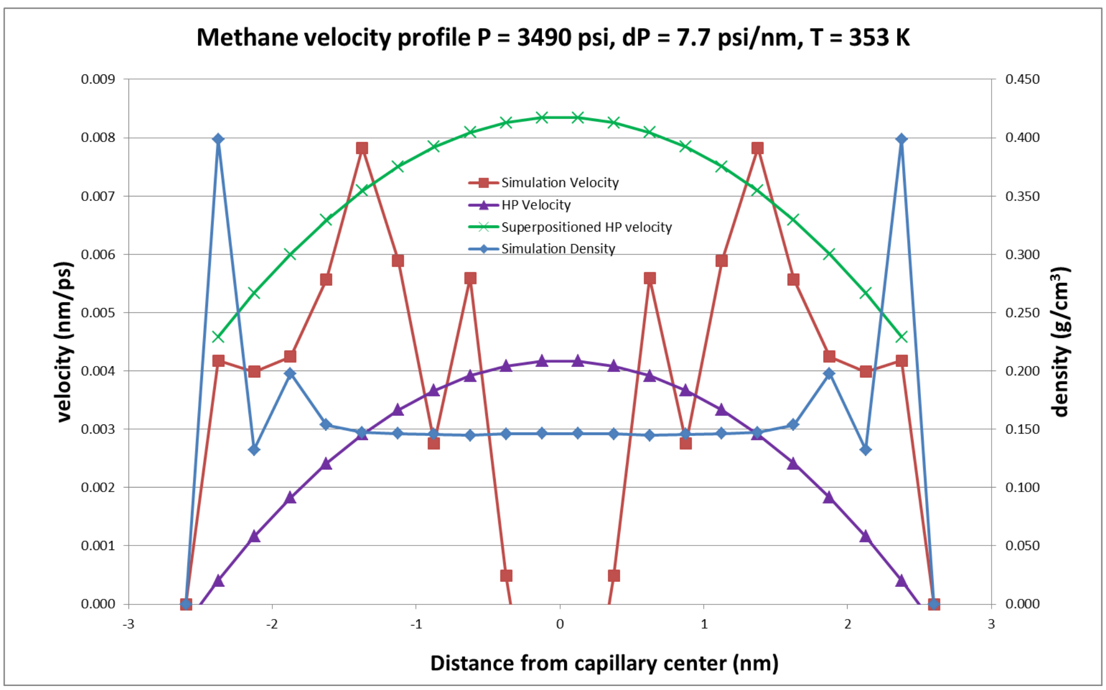

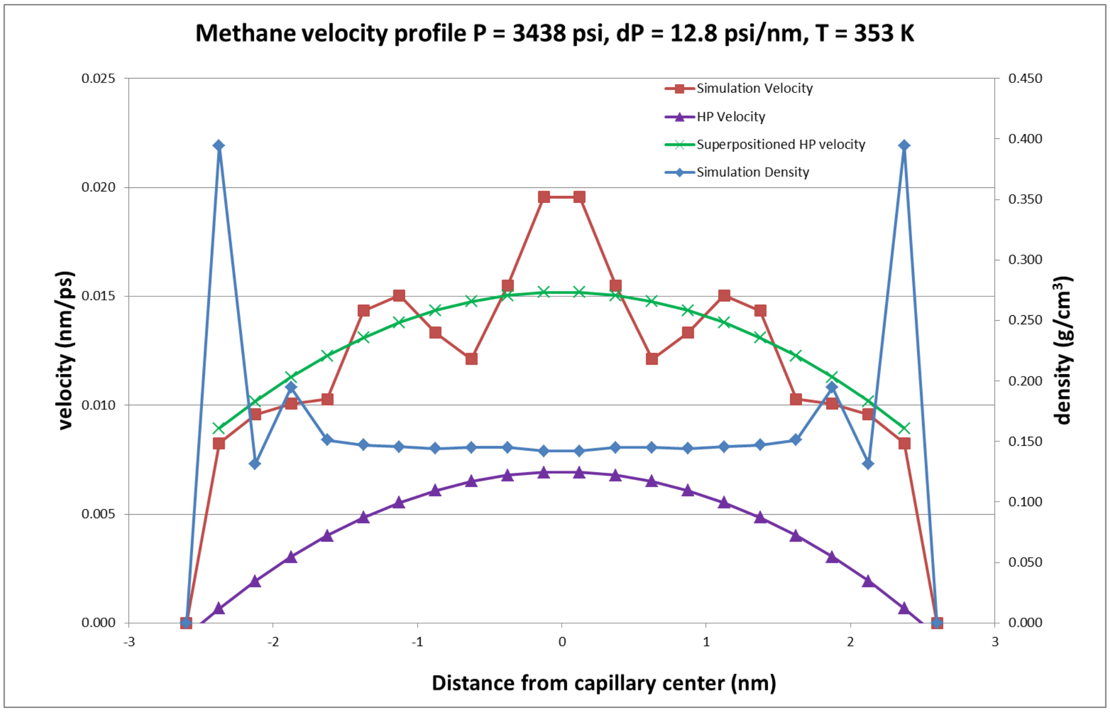
Methane velocity profile P = 3438 psi, dP = 12.8 psi/nm, T = 353 K
Simulation Velocity
HP Velocity
Superpositioned HP velocity
Simulation Density
velocity (nm/ps)
density (g/cm³)
Distance from capillary center (nm)
0.025
0.020
0.015
0.010
0.005
0.000
0.450
0.400
0.350
0.300
0.250
0.200
0.150
0.100
0.050
0.000
-3
-2
-1
0
1
2
3

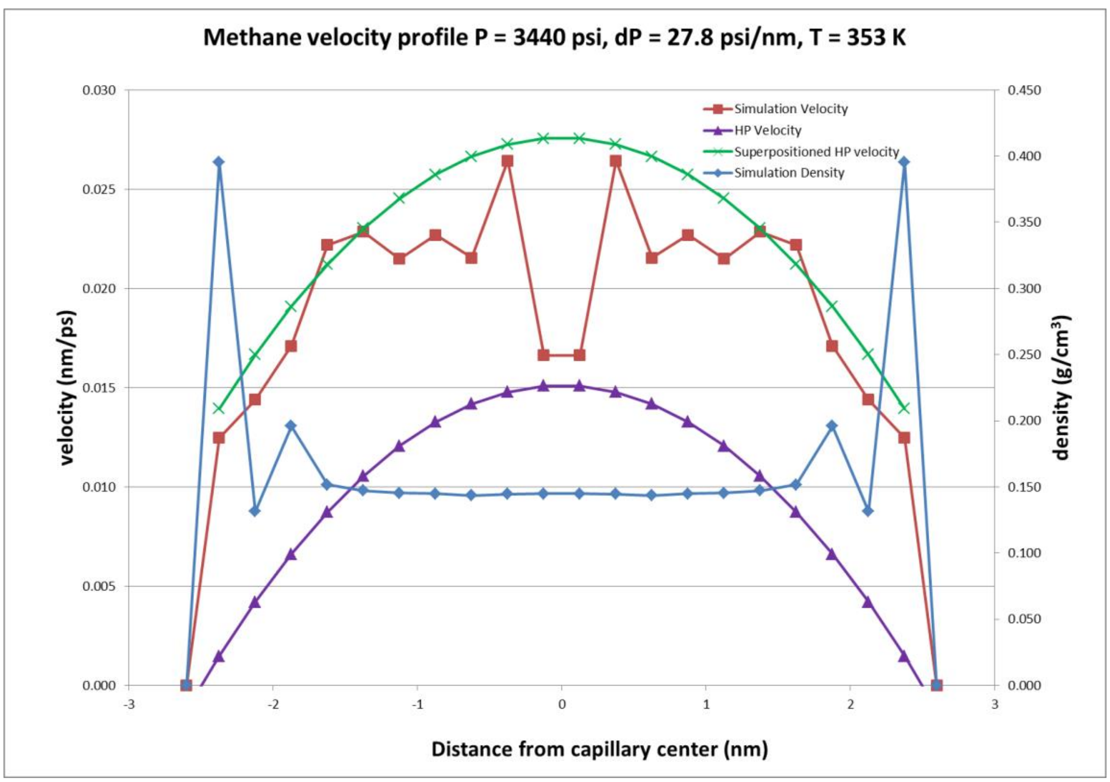
Methane velocity profile P = 3440 psi, dP = 27.8 psi/nm, T = 353 K
Simulation Velocity
HP Velocity
Superpositioned HP velocity
Simulation Density
velocity (nm/ps)
density (g/cm³)
Distance from capillary center (nm)
0.030
0.025
0.020
0.015
0.010
0.005
0.000
0.450
0.400
0.350
0.300
0.250
0.200
0.150
0.100
0.050
0.000
-3
-2
-1
0
1
2
3

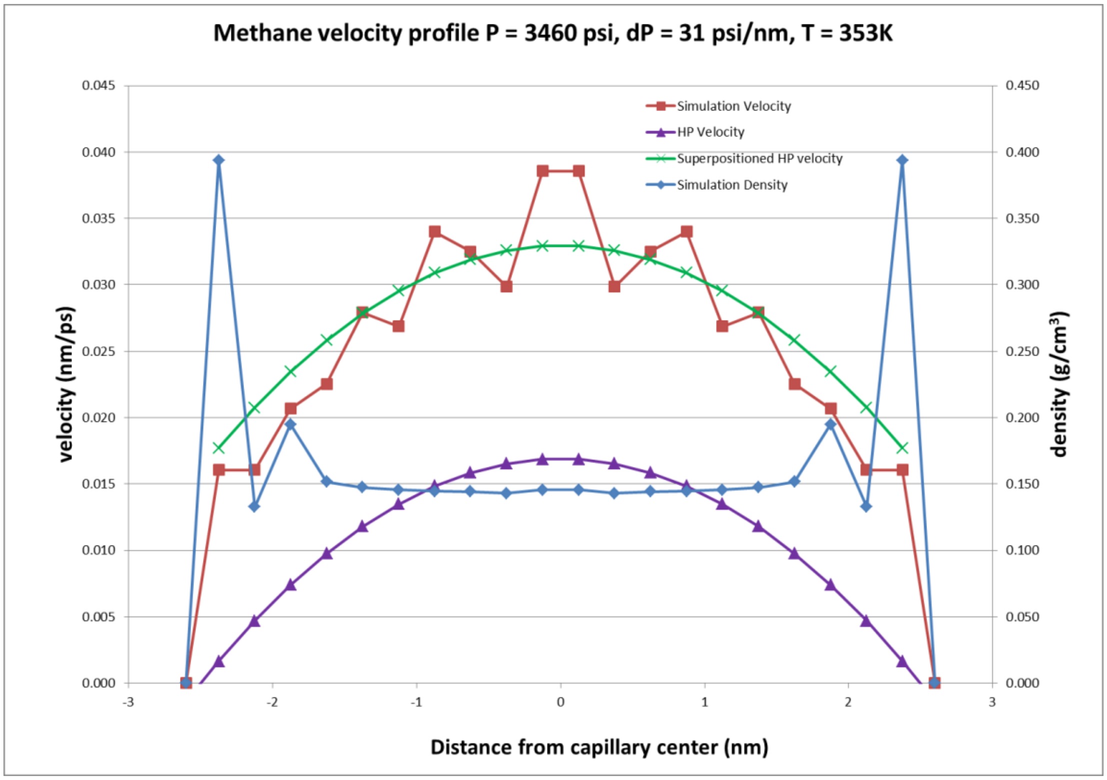
Methane velocity profile P = 3460 psi, dP = 31 psi/nm, T = 353K
Simulation Velocity
HP Velocity
Superpositioned HP velocity
Simulation Density
velocity (nm/ps)
density (g/cm³)
Distance from capillary center (nm)

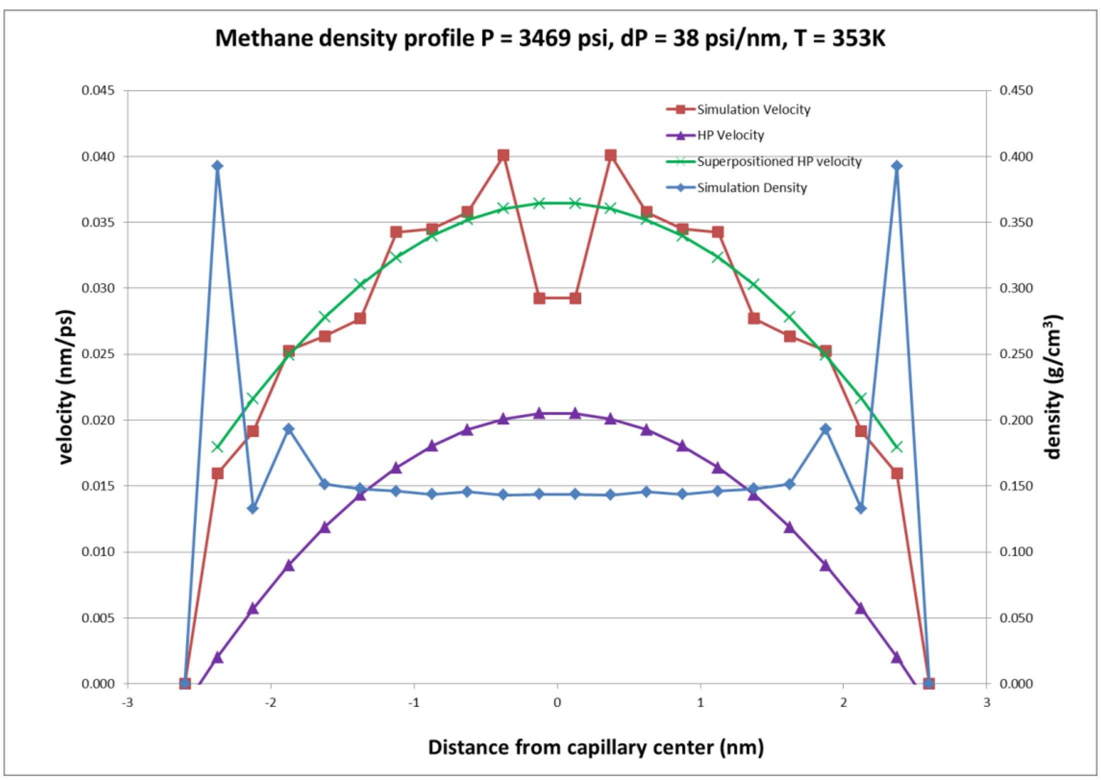
Methane density profile P = 3469 psi, dP = 38 psi/nm, T = 353K
Simulation Velocity
HP Velocity
Superpositioned HP velocity
Simulation Density
velocity (nm/ps)
density (g/cm³)
Distance from capillary center (nm)

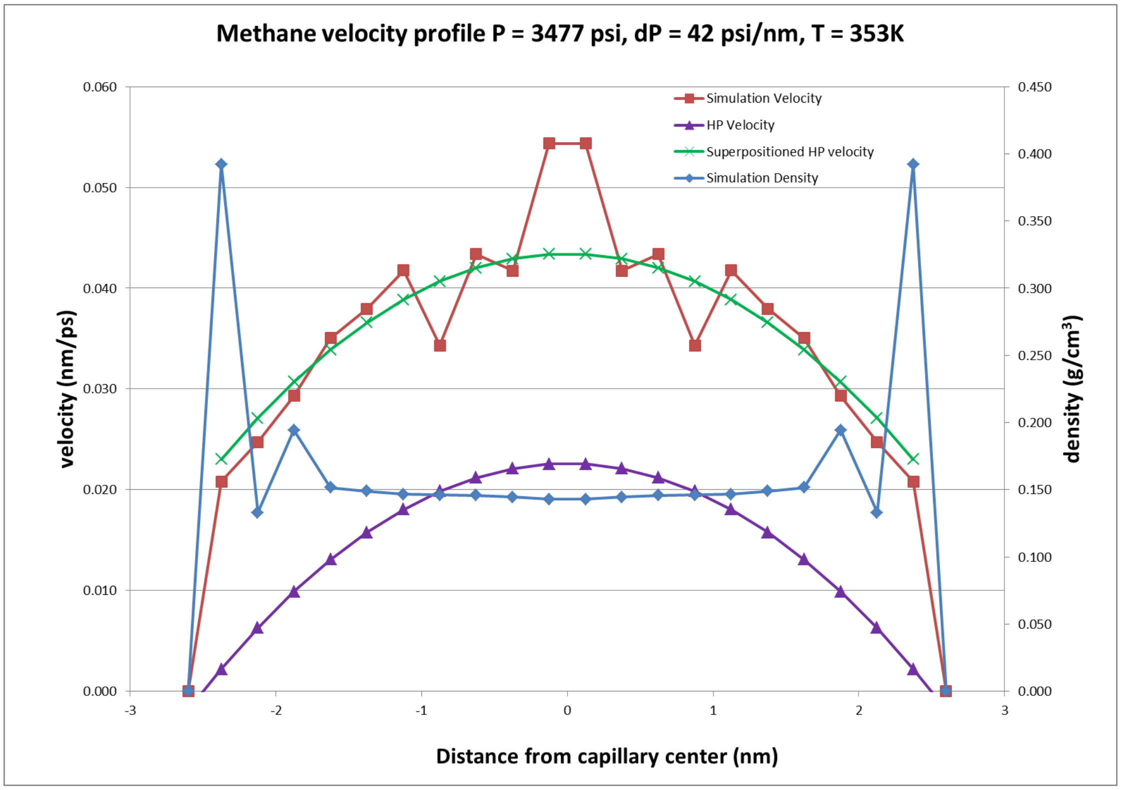
Methane velocity profile P = 3477 psi, dP = 42 psi/nm, T = 353K
Simulation Velocity
HP Velocity
Superpositioned HP velocity
Simulation Density
velocity (nm/ps)
density (g/cm³)
Distance from capillary center (nm)
0.000
0.010
0.020
0.030
0.040
0.050
0.060
0.000
0.050
0.100
0.150
0.200
0.250
0.300
0.350
0.400
0.450
-3
-2
-1
0
1
2
3

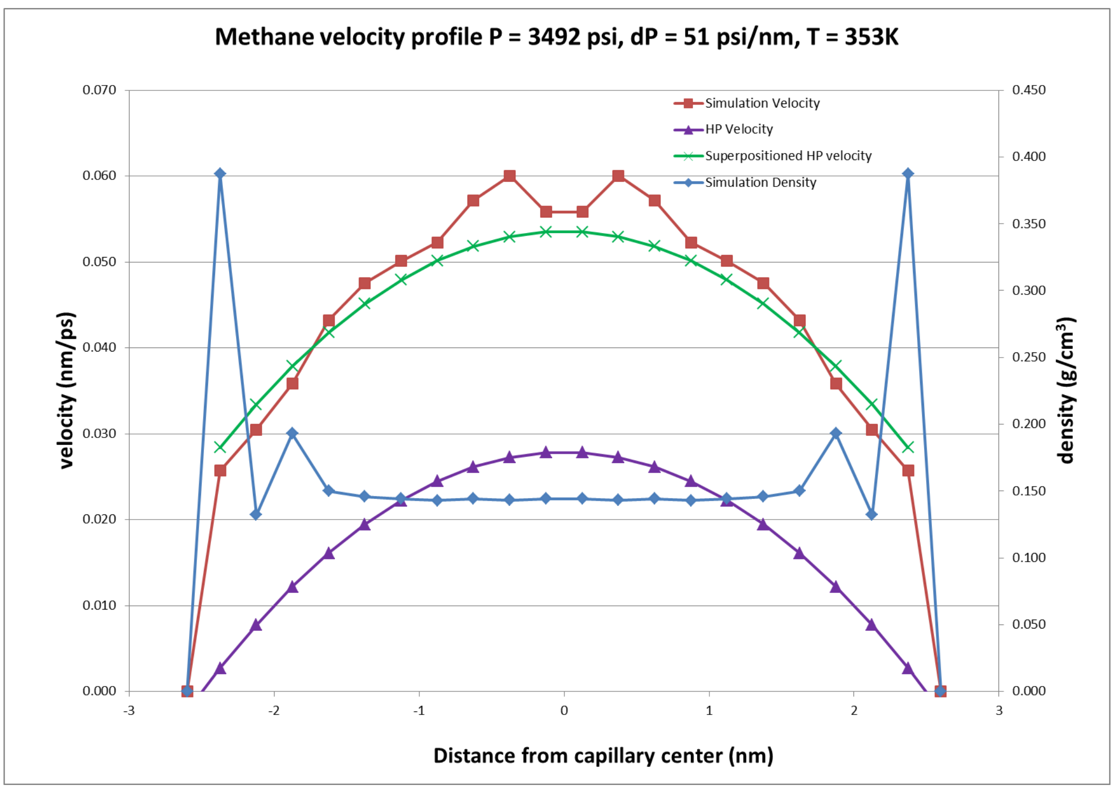
Methane velocity profile P = 3492 psi, dP = 51 psi/nm, T = 353K
Simulation Velocity
HP Velocity
Superpositioned HP velocity
Simulation Density
velocity (nm/ps)
density (g/cm³)
Distance from capillary center (nm)
0.000
0.010
0.020
0.030
0.040
0.050
0.060
0.070
0.000
0.050
0.100
0.150
0.200
0.250
0.300
0.350
0.400
0.450
-3
-2
-1
0
1
2
3

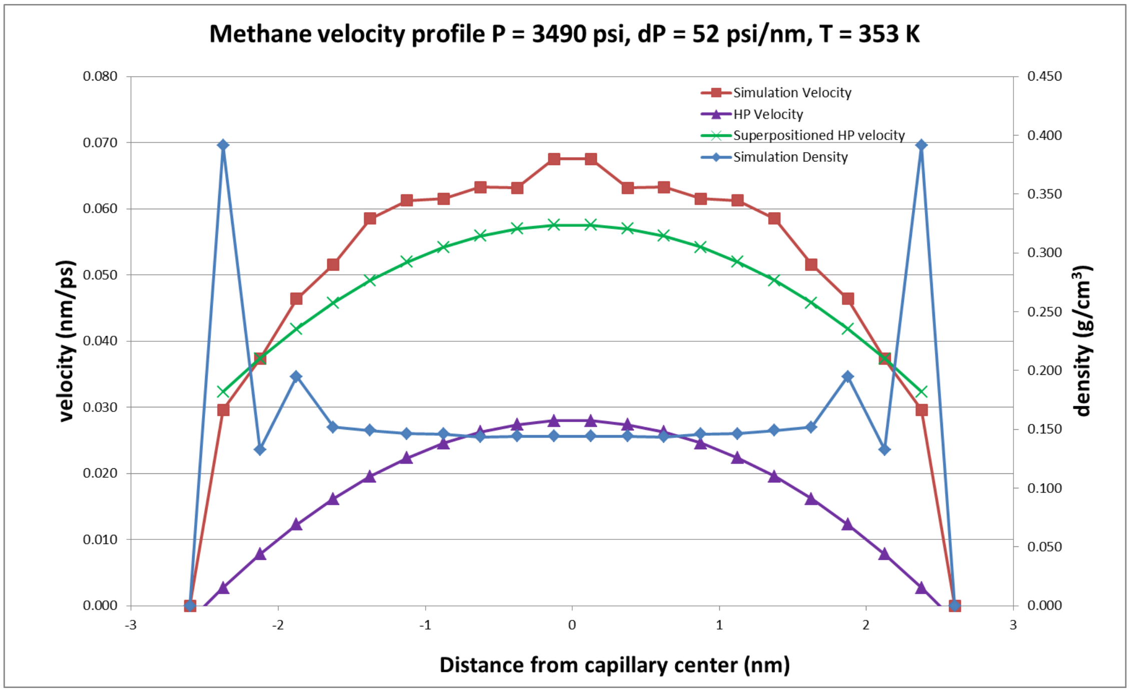

Methane velocity profile P = 3490 psi, dP = 52 psi/nm, T = 353 K
Simulation Velocity
HP Velocity
Superpositioned HP velocity
Simulation Density
velocity (nm/ps)
density (g/cm3)
Distance from capillary center (nm)
0.080
0.070
0.060
0.050
0.040
0.030
0.020
0.010
0.000
0.450
0.400
0.350
0.300
0.250
0.200
0.150
0.100
0.050
0.000
-3
-2
-1
0
1
2
3